Investigation of New Redox Active Materials for Thin Film Solar Cells

Doctor of Philosophy

by

Rebecca A. Milhuisen

B.Sci and B.Eng (hons), Monash University, Australia

Under the supervision of

Prof. Udo Bach

and

Prof. Michael Fuhrer

Declaration

I hereby declare that this thesis contains no material which has been accepted for the award of any other degree or diploma at any university or equivalent institution and that, to the best of my knowledge and belief, this thesis contains no material previously published or written by another person, except where due reference is made in the text of the thesis.

This thesis includes 2 *rewritten* works of published papers in peer reviewed journals and 1 unpublished publication. The core theme of the thesis is the investigation of redox active materials for thin film solar cells. The ideas, development and writing up of all the papers in the thesis were the principal responsibility of myself, the student, working within the Department of Chemical Engineering under the supervision of Prof. Udo Bach.

The inclusion of co-authors reflects the fact that the work came from active collaboration between researchers and acknowledges input into team-based research.

In the case of *Chapter 3,* my contribution to the work mainly involved the characterization of the newly developed redox active material, as well as the fabrication, optimization and characterisation of its application in devices. In the case of *Chapter 4,* my contribution to the work mainly involved the characterization of the newly developed redox active material. In the case of *Chapter 5,* my contribution to the work mainly involved the characterization of the newly developed redox active materials, as well as the fabrication, optimization and characterisation of their application in devices.

Thesis Chapter	Publication Title	Status	Nature and % of student contribution	Co-author name(s) Nature and % of Co-author's contribution*	Co-authors, Monash student Y/N
3	Cobalt Polypyridyl Complexes as Transparent Solution-Processable Solid-State Charge Transport Materials	Accepted	55%. Experimental conduct, manuscript drafting and editing.	1. Muhammad K Kashif. Synthesis. Exp. design. 19% 2. Michael Nippe. 1% 3. Jack Hellerstedt. Low. Temp conductivity, 5% 4. David Z. Zee. Ligand synth. 1% 5. Noel W. Duffy. Low temp. conductivity, IMVS, IMPS, 1% 6. Barry Halstead. GAXRD, 1% 7. Filippo De Angelis. DFT, 1% 8. Simona Fantacci. 1% 9. Michael S. Fuhrer. 1% 10. Christopher J. Chang. 1% 11. Yi Bing Cheng. 1% 12. Jeffrey R. Long. 1% 13. Leone Spiccia. 1% 14. Udo Bach. 10%	Yes No No No No No No No No No No No No No

I have rewritten sections of published papers and added additional data in order to generate a consistent presentation within the thesis.

Student signature: Date: 25-9-18

The undersigned hereby certify that the above declaration correctly reflects the nature and extent of the student's and co-authors' contributions to this work. In instances where I am not the responsible author I have consulted with the responsible author to agree on the respective contributions of the authors.

Main Supervisor signature: **Date:**

Copyright Notice

Notice 1

Under the Copyright Act 1968, this thesis must be used only under the normal conditions of scholarly fair dealing. In particular no results or conclusions should be extracted from it, nor should it be copied or closely paraphrased in whole or in part without the written consent of the author. Proper written acknowledgement should be made for any assistance obtained from this thesis.

Notice 2

I certify that I have made all reasonable efforts to secure copyright permissions for third-party content included in this thesis and have not knowingly added copyright content to my work without the owner's permission.

Table of Contents

Abstract

Thin film solar technologies that are compatible with robust and inexpensive manufacturing technologies like inkjet and roll-to-roll printing have been developed as promising alternatives to conventional first-generation photovoltaics. Among the thin film technologies that exist today, dye-sensitized and perovskite solar cells are viewed as major contenders.

Dye-sensitized and perovskite solar cells employ a range of different charge transport materials (CTMs) for which their primary function is to transport charge across the cell as well as perform important interfacial charge transfer reactions at the electrode interfaces. These tasks are heavily reliant upon their electrical and electrochemical properties which can be largely influenced by their physical properties such as solubility and morphology. With the majority of works nowadays focussing on the use of organic-based materials, this thesis explores the use of novel transition metal complexes as solution-processible CTMs for solar cells in which the redox transformation of the metal center provides a unique mode of conduction that is not applicable to their organic counterparts.

The design, characterization and application of three different transition metal complexes as CTMs in three different kinds of thin film solar cells—the liquid dye-sensitized solar cell, and the solid-state dye-sensitized and perovskite solar cells—forms the major content of this thesis. The transition metal complexes explored as CTMs in this thesis were designed to attain a low energy activation barrier for intermolecular charge transfer between its redox active centers that facilitate their two key functions of (i) charge transfer and (ii) charge transport.

First, the employment of cobalt complex based on a high denticity polypyridyl ligand, Co(bpyPY4), is explored for its use as a solid hole transporting material (HTM) in a solid-state dye sensitized solar cell. Films were found to be largely amorphous yet exhibited exceptional conductivity with a metallic-like behavior and attained exceptional pore-filling ability in devices, yielding an overall power conversion efficiency of 5.7%. An iron complex featuring the same high denticity polypyridyl ligand, Fe(bpyPY4), was also explored and

applied as a solid-state HTM in a perovskite solar cell. Unlike its cobalt counterpart, films were found to possess micro-crystallites embedded within a mostly amorphous matrix and displayed typical Arrhenius hole-hopping charge transport. Its application as an additive-free HTM in a $FAPbBr_3$ perovskite yielded a conversion efficiency of 2.2%. Lastly, a copper bis-phenanthroline-based complex featuring a bulky substituent on the phenanthroline ligand, $Cu(dpp)_2$, was explored for its performance as a redox mediator in a liquid DSC. In contrary to expectations, devices employing $Cu(dpp)_2$performed worse than the reference complex of higher activation energy, $Cu(dmp)_2$. A thorough investigation revealed that a strong interaction between the Cu(II) species and the common additive, tert-butyl pyridine, is key to achieving high-efficiency DSCs which uses copper complexes as the redox mediator.

Acknowledgments

Special thanks to Dr. Udo Bach who remained fully involved throughout my PhD work. His in-depth knowledge, particularly in the field of solar cells and in chemistry, helped push me through to completion of this PhD. I am very thankful for his guidance, as well as his patience and support throughout.

I would like to deeply thank my parents who always supported my studies and who have always remained a source of inspiration throughout my life. They, along with my brothers and extended family, have provided me with constant support and encouragement during my research, and their help during difficult times of research are greatly appreciated.

Thank you to the people who kindly dedicated their time to teach me how to construct and characterize solar cells at the commencement of my PhD, Rishabh Bhargava and Dr. Ishanie Perera. I would also like to thank the various people who helped me carry out a number of key characterizations throughout my PhD, and I would especially like to thank the skilled chemists for the supply of metal complexes which my work strongly depended upon, Dr. Muhammad Kashif and Dr. Sebastian Fuhrer. Synthesizing of new chemicals takes immense effort and amount of time to perfect, for which I am greatly appreciative. I am also very grateful for their guidance and help.

I would like to thank all my lab fellows in the Bach, Spiccia and the Cheng groups, both past and present, for their help and friendliness. I also express my deepest appreciation to those whom I could not mention but are an important part of my work and life.

List of Figures

List of Abbreviations

AgOTF	Silver trifluoromethanesulfonate
Al_2O_3	Aluminium oxide
bpyPY4	6,6'-bis(1,1-di(pyridin-2-yl)ethyl)-2,2'-bipyridine)-
CB / CBE	Conduction band / Conduction band edge
CE	Counter electrode
$Co(bpy)_3$	Tris(2,2'-bipyridyl)-Co (II/III)
Co(bpyPY4)	6,6'-bis(1,1-di(pyridin-2-yl)ethyl)-2,2'-bipyridine)-Co(II/III) TFSI
CTM	Charge transport material
$Cu(dmp)_2$ / $[Cu(dmp)_2]^{+/2+}$	Bis-(2,9-dimethyl-1,10-phenanthroline)copper(I/II)TFSI
$Cu(dpp)_2$ / $[Cu(dpp)_2]^{+/2+}$	Bis-(2,9-diphenyl-1,10-phenanthroline)copper(I/II)TFSI
CV	Cyclic voltammetry / voltammogram
DCM	Dichloromethane
DMF	*N*,*N*-dimethylformamide
DSC	Dye-sensitized solar cell
EDOT	3,4-Ethylenedioxythiophene
Et_2O	Diethyl ether
ETM	Electron transport material
EtOH	Ethanol
$FAPbBr_3$	Formamidinium lead iodide
Fc^+/Fc	Ferrocenium/Ferrocene redox couple
Fe(bpyPY4)	6,6'-bis(1,1-di(pyridin-2-yl)ethyl)-2,2'-bipyridine)-Fe (II/III) TFSI
FTO	Fluorine tin oxide
GAXRD	Grazing-angle x-ray diffraction spectroscopy
HOMO	Highest occupied molecular orbital
HRTEM	High resolution transmission electron microscopy / micrograph
HTM	Hole-transporting material
I^-/I_3^-	Iodide/triiodide
IPCE	Incident photon–to–current efficiency
IMPS	Intensity modulated photovoltage spectroscopy
IMVS	Intensity modulated photocurrent spectroscopy
IPA	Isopropanol
LUMO	Lowest unoccupied molecular orbital

MeCN	Acetonitrile
MLCT	Metal–to–ligand charge transfer
NHE	Normal hydrogen electrode
NMR	Nuclear magnetic resonance
$NOBF_4$	Nitrosonium tetrafluoroborate
OTf^-	Trifluoromethanesulfonate
PCE	Power conversion efficiency
PEDOT	Poly(3,4-ethylenedioxythiophene)
PL	Photoluminescence
PSC	Perovskite solar cell
PV	Photovoltaic
SDS	Sodium dodecyl sulphate
SEM	Scanning electron microscopy
ssDSC	Solid state dye sensitized solar cell
TAA	titanium diisopropoxide bis(acetylacetonate)
$TBAPF_6$	Tetrabutylammonium hexafluorophosphate
TBP	4-*tert*-butylpyridine
TCO	Transparent conducting oxide
TEM	Transmission electron microscopy / micrograph
TFSI	Trifluoromethanesulfonate
$TiCl_4$	Titanium tetrachloride
TiO_2	Titanium oxide
UV/Vis	Ultraviolet/Visible
VB / VBE	Valence band / Valence band edge
WS-72	(E)-3-(6-(8-(4-(bis(2',4'-bis(hexyloxy)-[1,1'-biphenyl]-4-yl)amino)phenyl)-2,3-bis(4-(hexyloxy)phenyl)quinoxalin-5-yl)-4,4-dihexyl-4H-cyclopenta[2,1-b:3,4-b']dithiophen-2-yl)-2-cyanoacrylic acid
XRD	X-ray diffraction spectroscopy
Y123	3-{6-{4-[bis(2',4'-dihexyloxybiphenyl-4-yl)amino-]phenyl}-4,4-dihexyl-cyclopenta-[2,1-b:3,4-b']dithiphene-2-yl}-2-cyanoacrylic acid
c-TiO_2	Compact titanium oxide
m-TiO_2	Mesoporous titanium oxide
AM1.5G	Reference solar spectral irradiance according to ASTM G-173-03
$[Cu(dmp)_2](TFSI)_{1/2}$	Bis-(2,9-dipmethyl-1,10-phenanthroline)copper(I/II)TFSI(bis(trifluoromethanesulfonyl)imide)$_{2/3}$

$[Co(bpyPY4)](OTf)_{2/3}$	6,6'-bis(1,1-di(pyridin-2-yl)ethyl)-2,2'-bipyridine)-Co(II/III) (trifluoromethanesulfonate)$_{2/3}$ TFSI
$[Fe(bpyPY4)](OTf)_{2/3}$	6,6'-bis(1,1-di(pyridin-2-yl)ethyl)-2,2'-bipyridine)-Fe(II/III) (trifluoromethanesulfonate)$_{2/3}$

List of Symbols

χ	Magnetic susceptibility
β	Boltzmann constant
σ	Conductivity
I	Current
J	Current density
τ	Decay time of an exponential fit
D / D^* / D^+	Dye in ground state / Excited dye / Oxidized Dye
e	Electron / Elementary charge
h	Film thickness
μ	Mobility
M	Molar mass
τ_{rec}	Recombination rate constant
R / R^+	Redox mediator in the reduced state / Redox mediator in the oxidized state
E^0	Redox potential
R / R_s / R_{sh}	Resistance / Series resistance / Shunt resistance
ρ	Resistivity
T	Temperature
V	Voltage / Volume
λ	Wavelength
n	Number of…
h	Hole
V_{OC}	Open circuit voltage
J_{SC}	Short-circuit current density
FF	Fill factor
η	Photon-to-electrical power conversion efficiency
P_{max}	Maximum power output
P_{in}	Power IN
φ_{inj}	Injection efficiency
φ_{reg}	Regeneration efficiency
φ_{cc}	Charge collection efficiency
R_{diff}	Diffusion resistance

R_{CE}	Charge transfer resistance at the counter electrode
R_{rec}	Recombination resistance

Chapter 1:

Introduction to Renewable Energy and Solar Cells

Introduction to Renewable Energy and Solar Cells

Chapter contents

1.1 Towards Renewable Energy

Since the beginning of the industrial revolution, the world has seen an ever-increasing reliance on energy, the majority of which comes from fossil fuels such as oil, gas, and coal. However, consumption rates of fossil fuels far exceed the rate at which they can be replenished, with remaining natural oil reserves expected to last only for another 40-50 years, gas reserves for 70 years, and coal for > 200 years[1]. Moreover, the production of pollutant CO_2 emissions generated during their combustion has resulted in *global warming*—a long-term rise in the average temperature—the consequences of which include rising sea levels, extreme weather and species extinctions[2]. Viewed as one of the biggest threats to the future sustainability of the planet, the Paris Climate Agreement (2016) was established in a global effort to drastically reduce carbon emissions by (i) phasing out fossil fuels and (ii) exploiting clean renewable energy technologies for future energy needs.

Of the renewable resources (wind, biomass, geothermal, tidal, hydropower and solar), solar energy remains the largest resource by far. In fact, the amount of solar energy striking land is 23000 terawatt-years, approximately 1500 times the worlds current energy usage and far beyond capable of fully supplying the projected energy demand in the year 2050[4]. To utilize solar energy effectively, a number of technologies have been devised which include solar heating, solar thermal electricity, solar fuels and solar cells. The latter, which directly converts solar energy to electrical energy, is currently the fastest growing fields in energy technology and represents one of the most promising renewable alternatives to fossil fuels and predicted to contribute up to 50% of all electricity by 2050[5]. Demonstrating their huge advantage of scalability, solar cells can be used to power small devices, residential houses and large building infrastructures, or be installed by the thousands to form large power plants.

1.2 Solar Cells

Solar cells generate electrical energy through materials that exhibit the photovoltaic effect, a process whereby the energy of light is transferred to the electrons of a light absorbing material, causing the electrons to jump from a low to a high energy state and leave behind a hole. Due to a driving force, such as an inherent electric field that exists within the cell, the electrons and holes become separated, moving in opposite directions to generate electrical current to power a load. It is this direct conversion of sunlight into electricity—without pollution, sound, or moving parts—which makes solar cells a long-lasting and dependable technology. As shown in Figure 1, the solar spectrum of light at the Earth's surface is mostly spread across the visible (~50%) and near-infrared (42%) ranges and a small part in the near-ultraviolet (8%)[6]. Therefore, key to efficient light harvesting in solar devices is to employ highly absorbing materials (high molar extinction coefficient) with an absorption spectrum strongly overlapping with the solar emission spectrum shown in Figure 1.

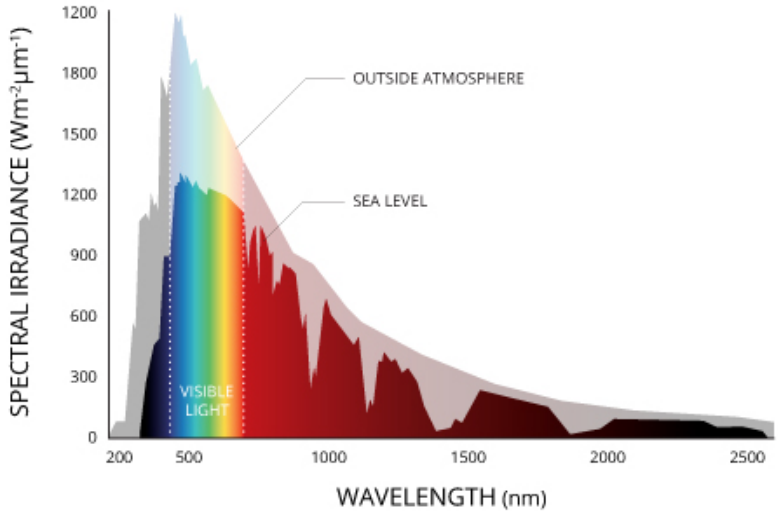

Figure 1. Solar spectrum.[6]

Several promising solar cell technologies utilizing a vast range of materials and processing techniques have been proposed over the last three decades, which can be broadly divided into three generations. First generation of solar cells are based upon semiconductor p-n junctions such as crystalline silicon. Reaching efficiencies of 21% for industrially produced panels (and up to 27% for state-of-the-art lab-scale devices), silicon solar cells account for

the majority of solar panels sold around the world[7]. However, their complex structure and lengthy manufacturing (purification) processes required bares significant impacts the cost of solar electricity and is by far the biggest challenge associated with the silicon-based solar technology[8]. Second generation solar cells are those based on semiconductor thin-films of only a few micrometers thick. The combination of reduced material usage and easier processing methods that allow for their production at low-cost highlights them as viable alternatives to first generation solar cells. Amorphous silicon, cadmium telluride (CdTe), and copper indium gallium diselenide (CIGS) thin-film solar cells are among the best examples, having certified efficiencies of 26.1%, 22.1%, and 22.9%, respectively[7]. However, the use of rare and rather toxic elements have limited their large-scale production. Third generation solar cells are those utilizing solution processed organic, hybrid and inorganic semiconductors and new materials such as nanomaterials and conductive plastics. These include organic polymer (OPV), dye-sensitized (DSC) and perovskite solar cells (PSCs). Though the efficiencies are generally lower, the use of materials that are high in abundance, compatible with low-cost thin-film production methods such as inkjet and roll-to-roll printing makes them attractive alternatives to both first- and second-generation solar cells. Moreover, design opportunities, high temperature stability, flexibility, better diffused and low light performance and the potential to overcome the Shockley–Queisser limit (31–41% power conversion efficiency) by using multi-junction (tandem) structures makes them promising technologies.

Figure 2 is a compilation of device efficiencies of the main classes of solar cell technologies currently under investigation, showing the historic evolution of such technologies by different research groups around the world[7].

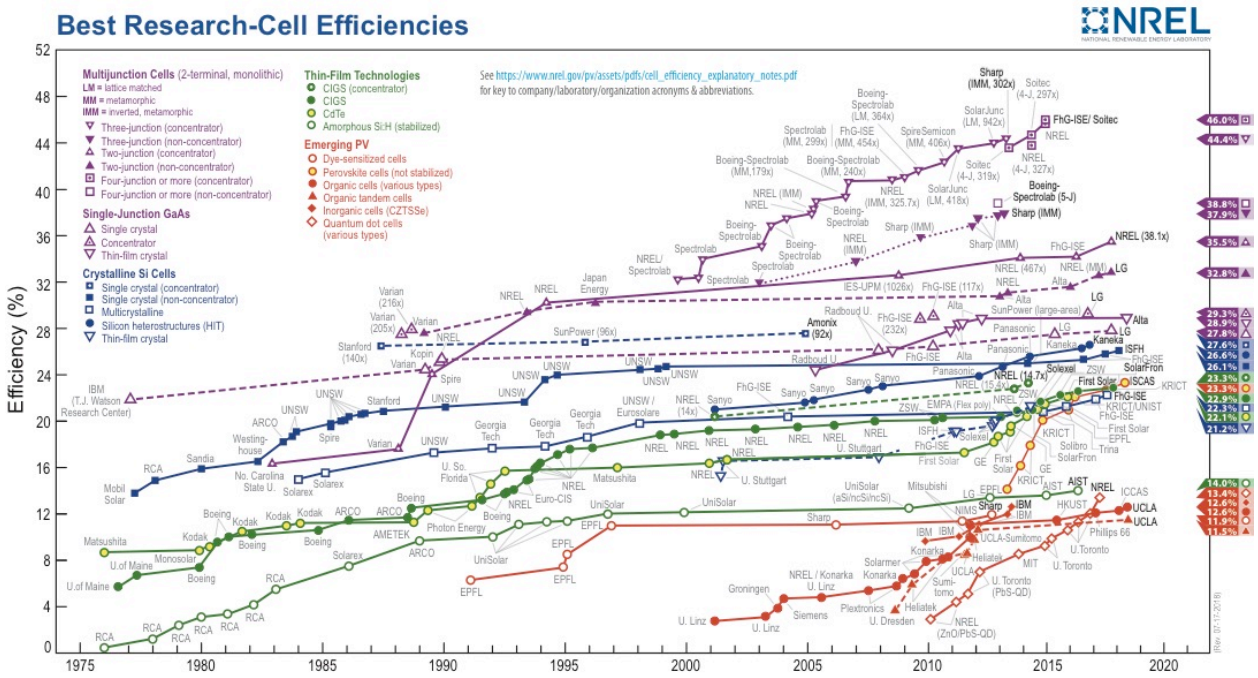

Figure 2. NRELs "Best Research-Cell Efficiencies" (Date of publication: 02/09/2018)[7]

1.3 Thin Film Solar Cells: From Liquid-Based Dye-Sensitized to Solid-State Perovskite Solar Cells

While research on silicon solar cells continue, attempts to reduce the cost and enhance efficiency are slowly reaching its limits due to the expensive, multistep processes at high temperatures/vacuum and ultra-clean conditions often required for their fabrication. As a result, thin film technologies—based upon the layering of lost-cost materials with film thicknesses ranging from only a few nanometers to tens of micrometres and fabricated through solution-processible techniques—have emerged as low-cost alternatives with the potential meet future energy needs. Dye-sensitized solar cells are among first of these technologies to be developed, with the first breakthrough demonstration of a high-efficiency DSC demonstrated by O'Regan and Grätzel in 1991[9]. Fabricated mostly with abundant, affordable and environmental-friendly materials, the DSC uses photoexcitable dye molecules attached onto a large-area semiconducting scaffold to capture light energy, and an electrolyte containing a redox couple to mediate charge towards the counter electrode. Since then, tremendous efforts to improve this technology in terms of both efficiency and long-term stability have taken place, with a significant amount of research focussed on the discovery or development of new and more advanced materials. This search has ultimately resulted with the emergence of the all solid-state DSC by Bach *et al.* in 1998[10]—in which the liquid electrolyte was replaced by a solid-state hole-transporting material—followed by the PSC by Miyasaka in 2009[11]—in which the dye was replaced with a highly absorbing perovskite material. Despite material and architectural differences, the fundamental processes occurring in all three solar systems are very similar, i.e. light absorption by a photosensitive material followed by selective charge collection at each respective contact. The differences between these technologies are described in the following sections, with a most detailed explanation provided for the liquid-based DSC upon which both the ssDSC and PSC were built upon.

1.3.1 Liquid-Based Dye Sensitized Solar Cells (DSCs)

Device architecture and basic principle. As depicted in Figure 3a, the DSC comprises of various components sandwiched between two current-collecting transparent conducting oxide (TCO) electrodes. When irradiated, solar energy is absorbed by the monolayer of dye molecules that are covalently attached to a wide-bandgap n-type semiconductor, typically a mesoporous titanium dioxide (TiO_2) scaffold as shown. This is then followed by ultrafast electron injection from the excited dye molecules into the conduction band of TiO_2,[12,13] after which the electron can then move through the continuous TiO_2 mesoporous network until reaching the TCO as described by a diffusion controlled trapping-detrapping model[14]. At the same time, the hole left behind in the now-oxidized dye molecule becomes regenerated by the reduced species in the electrolyte infiltrating the mesoporous structure, which, in turn, diffuses towards the counter electrode to become restored. Interfacial electron transfer processes at both electrodes occurs as described by Marcus' theory[15,16]. Undesirable dye relaxation (via radiative/non-radiative decay) and recombination of electrons with holes are processes that can also take place, undermining the charge collection efficiency, Φ_{cc}, and overall performance of the device[17]. An overview of all the forward and back reactions that can occur in a DSC (as just described) is provided in Figure 3b. The electron pathway is ultimately dependent upon the driving force for each electron transfer process at each interface, and the comparative time scales on which they occur is (discussed further in section 1.3.1.1). The voltage output of the DSC is determined by the energy difference in redox potential of the redox mediator and the quasi-Fermi level (EF) of TiO_2 under illumination, while the current output is determined by the light-harvesting ability and the total amount of dye bound to the semiconducting surface. Maximizing both the voltage and current outputs and minimizing wasteful recombination processes are fundamental to achieving high-efficiency devices (see section 2.4.1).

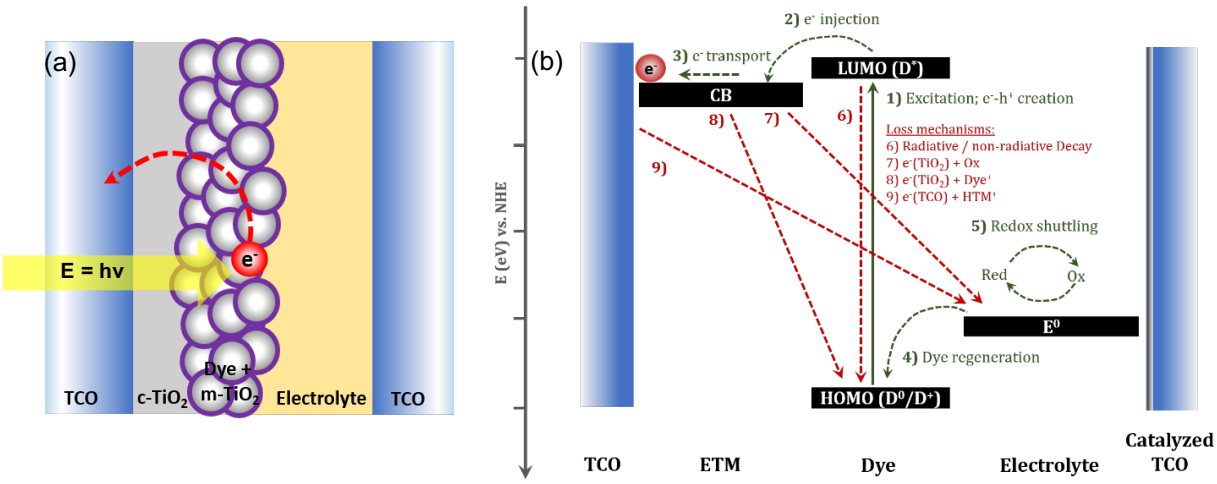

Figure 3. (a) Device architecture and **(b)** schematic of basic operation of a liquid-based DSC.

Maximizing charge collection. Key in the development of high-efficiency DSCs is the use of a nanostructured semiconducting scaffold of high surface area that enables a remarkably high light absorption capacity by adsorbed dye molecules, thereby maximizing the attainable photogenerated current. However, despite its benefits, the large interfacial area between the semiconductor, dye and the electrolyte can also lead to greater pathways of electron recombination that can lead to an overall loss of photo-generated charge carriers. Methods to succumb these negative pathways have been developed that successfully lead to overall improvements in device performance. Such methods include the employment of a compact TiO_2 under layer that eliminates the direct contact between the TCO and the electrolyte, and the use of additives in the dye/electrolyte solutions that block certain recombination pathways (see section 1.3.1.2).

Record efficiency. The champion state-of-the-art DSC today produces an average PCE of 14.3% under standard AM1.5G irradiation[18] (Figure 4), which consists of a mesoporous TiO_2 nanoparticle electrode co-sensitized with an alkoxysilyl-anchor dye (ADEKA-1) and a carboxy-anchor organic dye (LEG4) in combination with the Co(III/II) tris(1,10-phenanthroline) (Co(phen)) redox mediator. More interestingly, DSCs have been shown to perform better compared to crystalline silicon solar cells under simulated low-light indoor conditions (Figure 5), with a record efficiency of 32% under 1000 lux indoor

illumination when employing the copper complex, $[Cu(tmby)_2]^{+/2+}$ in conjunction with the organic Y123 sensitizer. [19]

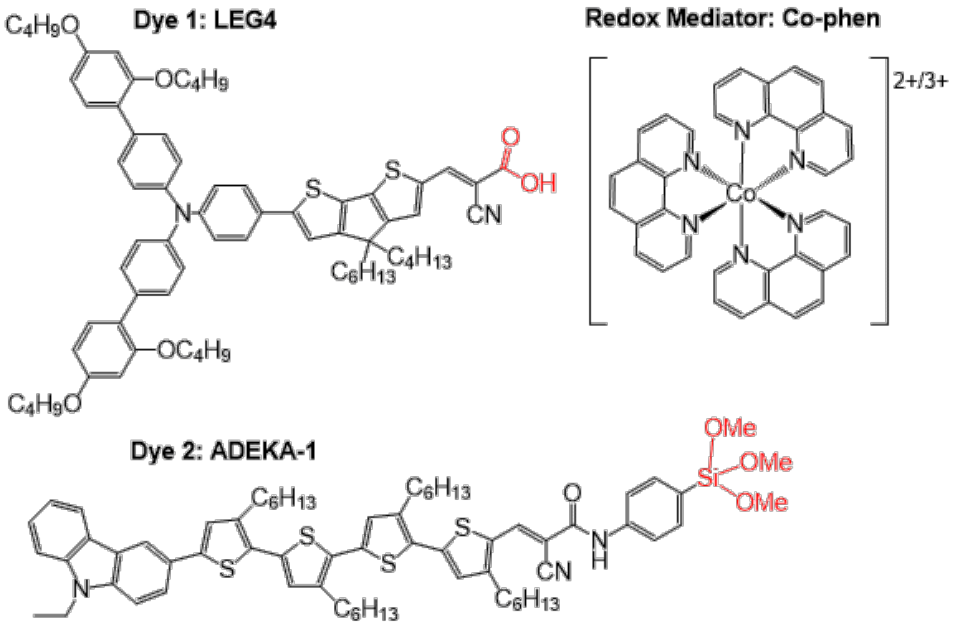

Figure 4. Molecular structures of the ADEKA-1 and LEG4 dyes and $Co(phen)_3$ redox mediator that are used to achieve the highest reported DSC efficiency under standard AM1.5G irradiation.

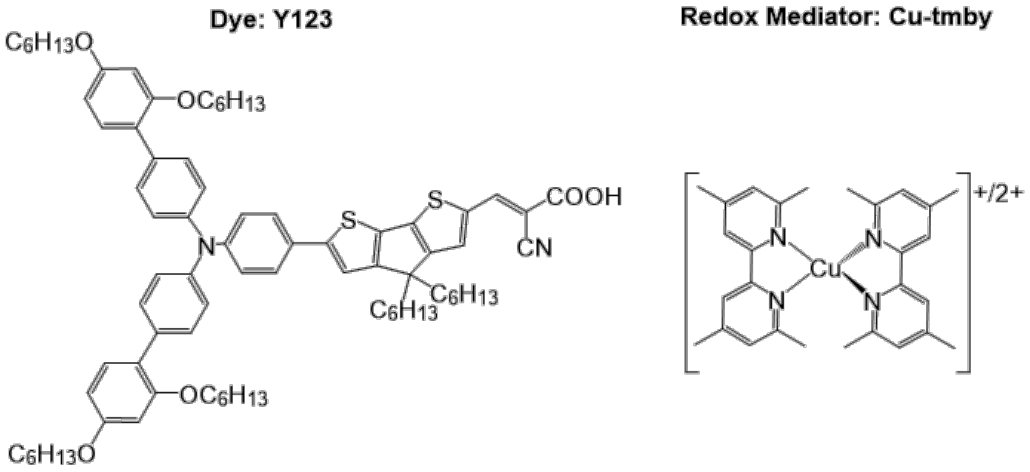

Figure 5. Molecular structures of the Y123 dye and $Cu(tmby)_2$ redox mediator that are used to attain the highest reported DSC efficiency under low-light conditions.

1.3.1.1 Electronic Processes

In contrast to conventional p–n junction solar cells, the various processes of charge separation, transport and collection are designed to be split between the different

material components making up the device, conveniently allowing one to investigate each process separately, and tailor them accordingly to achieve efficient energy conversion. Following the initial photoexcitation step of the dye, the ideal pathway, of course, is for the excited electron to be injected into the conduction band of TiO_2 and subsequently diffuse through the mesoporous network towards the TCO for charge extraction. At the same time, regeneration of the oxidized dye molecules is to be achieved by the redox mediator in the electrolyte. In this way, the electrical circuit is complete, with the flow of electrons moving in the one direction to power a load. However, the competitive processes such as relaxation of the photoexcited dye to the ground state as well as the recombination of electrons with either the oxidized dye or the redox mediator (or both), can take place. The competition between the charge transfer dynamics and kinematics at each interface (as well as the charge transport ability within the bulk materials) are what ultimately determines the direction of the charge transfer and overall charge collection efficiency at the metal contacts. These are highlighted below.

Dynamics

For the interfacial electron-transfer processes to take place, an energetic driving force is required. First, when the dye absorbs sunlight, an electron is excited from the HOMO (highest occupied molecular orbital) energy level to the LUMO (lowest unoccupied molecular orbital) energy level. For this process to occur, the incoming light should have sufficient energy that is equal to or greater than the difference between the HOMO and LUMO level of the dye. Following excitation, an energetic driving force is necessary for electron injection into TiO_2. Under dark conditions, the Fermi level of the TiO_2 and the redox potential of the redox couple are aligned, and therefore there is no positive driving force for electron injection and thus no current flow. Under illumination, the electron concentration in the TiO_2 increases thus shifting the *quasi*-Fermi level of the TiO_2 up and providing a positive driving force for the LUMO electron transfer to occur. Once the electron gets injected, the dye then becomes oxidized and no longer contributes to the system until it becomes regenerated—ideally by the redox mediator—back to its ground state form which can then be re-excited. The energetic driving force required for

regeneration of the dye by the redox mediator is given by the difference in redox potential of the redox mediator and HOMO of the dye. By keeping the driving force needed for electron injection and dye regeneration sufficiently small, one can maximize the voltage output from the device. At the same time, however, the unfavourable electron transfer processes (in particular, those between injected electrons in the TiO_2 with the oxidized redox mediator) can become easier. Thus, in order to maximize the conversion efficiency of devices, the energy levels of the different components must be tuned carefully, to maintain a sufficient driving force for electron transfer in the system, meanwhile avoiding energy losses incurred by high overpotentials.

Kinetics

Electron transfer kinetics of the favourable electron pathways must occur on smaller timescales compared to that of undesirable electron pathways. More specifically, (i) the electron injection time must be faster than the dye relaxation time, (ii) the electron diffusion through TiO_2 must be faster than recombination with the oxidized electrolyte or dye, and (iii) regeneration of the photo-oxidized dye molecule by the CTM must be faster than the recombination with electrons from the TiO_2. Rate constants of the different electron transfer processes strongly depend on the materials employed. For the typical iodide/triiodide-based DSC, electron injection into the TiO_2 takes place in the femtosecond to picosecond scale, which is faster than the relaxation time of the dye to its low energy state (nanosecond), and significantly faster than that of recombination with the oxidized dye molecules (μs to ms range) and the oxidized redox mediator (milliseconds to seconds), allowing for the sustained performance of the DSC[20].

1.3.1.2 The Important Components

The Transparent Conducting Oxide (TCO) Electrodes

The main function of the electrode is to effectively extract and transport charges from the inner components of the device while still allowing for the transmission of incoming solar radiation to reach the dye molecules. Glass substrates are generally used as they are low-

cost and exhibit high optical transparency in the visible and near infrared regions, which is then typically coated with a transparent conductive film such as fluorine doped tin dioxide (FTO).

The Light Absorber; Dye

Light capture is achieved by a monolayer of dye molecules that are attached to the surface of the semiconducting surface and thus play the key role of the DSC. For maximum photocurrent, the sensitizer should possess exceptional absorption properties over the visible spectrum—largely overlapping with the solar emission spectrum—and with high molar extinction coefficient. The transition that is generally responsible for the absorption of visible light is the transition from the highest occupied molecular orbital (HOMO) to the lowest unoccupied molecular orbital (LUMO) of the dye. Furthermore, to achieve efficient electron injection, strong binding of the dye molecule to the semiconductor surface is required. This binding is usually achieved through the chemical bonds formed with the semiconductor via functional groups inherent in the dye structure, the most common ones being the carboxylic and phosphonic acid groups. Appropriate positioning of the dye's energy levels relative to the conduction band of the n-type semiconductor and the energy levels of the CTM is also of critical importance to allow for the preferential movement of electrons in the device. Specifically, the LUMO should be sufficiently high for efficient electron injection into TiO_2 and the HOMO be sufficiently low for the efficient regeneration of the oxidized state.

Over the past three decades of DSC research, hundreds of dyes have been designed in an effort to yield higher molar extinction coefficients, extend absorption beyond 800 nm, lower recombination losses and maximize the injection yield. The majority of these can be categorized as being metal complexes or organic dyes. Metal complex sensitizers, in particular, those based on polypyridal compounds of Ru(II) such as N3, N719 and Z907 have been used extensively due to the predominant absorption bands across the visible region as a result of the metal–to–ligand charge transfer (MLCT) transition in addition to the absorptions resulting from organic ligand charge transfer (LCT)[21]. However, their

relatively low molar extinction coefficients, roughly 10^4 mol^{-1} cm^{-1}, necessitates the use of relatively thick semiconducting films 10–20 μm for adequate light absorption. Organic sensitizers, on the other hand, that form large conjugated π-systems yield relatively high molar extinction coefficients as a result of the low-energy (usually intramolecular) π-π * transitions, allowing the use of thinner films. A large variety of organic sensitizers have been designed such as those based on porphyrins[22], phthalocyanines[23], squaraines[24], as well as those comprising various functional groups such as long alkyl and alkoxy side chains to improve alignment and block electrolyte access to the semiconductor surface thus reducing recombination losses[25–27]. The Donor-π-Acceptor (D–π–A) dye is one particular design of dye that has retrieved significant attention which, as the name implies, consists of three organic moieties—an electron-rich donor unit (D), an electron-deficient acceptor unit (A) (with an anchoring functionality attached) and a conjugated π-bridge (π) connecting the two—which maintains good electron delocalization across the entire molecule[28]. When light is absorbed, the electron density is vectorised in the direction of the semiconductor surface that enables efficient electron injection into the conduction band of the semiconductor, such as the 3-{6-{4-[bis(2',4'-dihexyloxybiphenyl-4-yl)amino-]phenyl}-4,4-dihexyl-cyclopenta-[2,1-b:3,4-b']dithiphene-2-yl}-2-cyanoacrylic acid (Y123) dye shown in Figure 6.

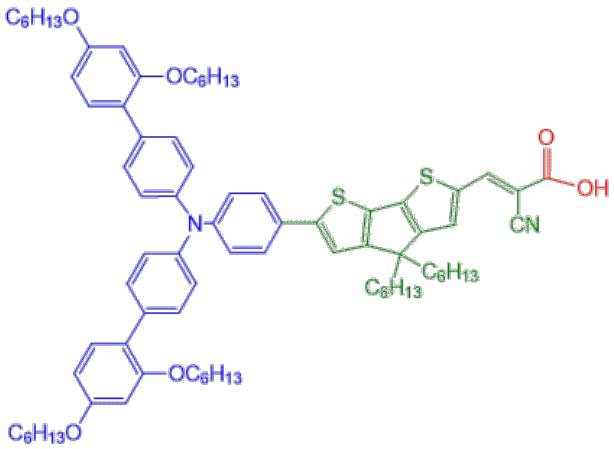

Figure 6. Molecular structure of a high performing Donor–π–Acceptor dye, Y123 (donor = blue, π-bridge = green, acceptor = red).

The N-type Semiconductor (Electron Transport Material, ETM); TiO_2

This component crucial for DSCs as it serves as a scaffold onto which dye molecules can attach and transfer its excited electrons. Following this, the key function of the n-type semiconductor is then to transport the electrons away towards the TCO, after which they can then move into the external circuit to power a load. Amongst the few semiconductors that have been developed thus far, TiO_2—being an abundant, non-toxic and environmentally friendly material with superior chemical stability and a wide band gap of ~3.2 eV—makes it, by far, the most popular material of choice. TiO_2 exists naturally in three different phases; rutile and brookite and anatase, the latter phase of which has been the benchmark and thus the most widely used phase for DSC applications[29–31].

A mesoporous layer. Key to maximizing the amount of generated photocurrent is to use a nanostructured scaffold comprising an interconnected network of *transparent* TiO_2 nanoparticles that provides a high-surface area available for dye-attachment. To date, a large number of different materials and morphologies have been developed, the most common and successful one being a mesoporous (sponge-like) structure that comprises of interconnected TiO_2 spherical nanoparticles. The smaller the particle size, the larger the surface area, thus, it is often desirable to employ the smallest possible particle size. However, it is also necessary to ensure that the pore size (which is directly proportional to the nanoparticle size) is large enough to be infiltrated by the electrolyte. As such, a compromise between the two needs to be found, which is largely dependent upon the electrolyte in use. Typically, a 30 nm particle size (in diameter) is used for metal complex-based electrolytes, whilst 18 nm particle size is large enough for the traditional iodide-triiodide electrolyte system. A light *scattering* layer is also commonly used, typically comprising of nanoparticles with a diameter of 400 nm, in order to back scatter photons towards the dye molecules that were not initially absorbed when passing through the transparent film[32–34]. The most widely used technique to deposit the mesoporous layer is by doctor blading or screen-printing a paste comprising the nanoparticles of desired size, with the inclusion of binders and polymer fillers that control the porosity and uniformity of the film, which are then removed during the sintering process used to form interconnections between the nanoparticles.

A compact underlayer. To prevent direct contact between the TCO and the oxidized species of the redox couple and thus block interfacial recombination reactions that limit device performance, a compact TiO_2 layer is often deposited beneath the mesoporous layer. Ideally, the blocking layer is made to be as thin as possible but as thick as necessary to achieve full surface coverage of the TCO surface. Several techniques have been used to deposit compact layers such as spray pyrolysis[35], electrochemical deposition[36], hydrolysis[37] and atomic layer deposition[36], the total thicknesses of which would typically lie in the range of 10 – 100 nm. Of the techniques developed, the two methods that are commonly used are spray pyrolysis (spraying a titanium diisopropoxide bis(acetylacetonate) (TAA) diluted solution in isopropanol (IPA) solvent on top of the heated TCO substrate which causes the decomposition to TiO_2) and hydrolysis (immersion of the TCO substrates into an aqueous solution of $TiCl_4$). Formation of a compact TiO_2 layers in this way is very simple and inexpensive, yielding films of relatively good quality and uniformity[38]. A $TiCl_4$ post-treatment is also done to improve both the roughness of the TiO_2 films and inter-particle connection between the TiO_2 nanoparticles for efficient charge carrier transport. An overall improvement in device efficiency is observed as a result of the post-treatment which can be attributed to an increase in the electron injection efficiency, retardation of recombination and increase to the adsorption capacity[39,40].

The Electrolyte

The electrolyte is used to facilitate charge transport between the electrodes and to ensure quantitative dye regeneration. Typical electrolytes contain a redox couple and electrolyte additives (discussed below) dissolved in an organic, non-protonic, low-viscosity solvent such as acetonitrile (MeCN) or propionitrile that do not limit the mass transportation (diffusion) of the redox mediator within the electrolyte. Electrolyte filling through a small opening with the aid of vacuum is the typical technique employed in the fabrication of DSCs, and generally found to achieve sufficient contact with the sensitized semiconducting surface, provided the redox mediator maintains good solubility in the

solvent used and adequate sealing that does not permit the evaporation of electrolyte solvent.

The redox couple. The redox couple forms the most important component of the electrolyte, performing the main tasks of regenerating the dye as well as mediating charges between the working and counter electrodes via a redox shuttling process (mass transport of the redox mediator that is driven by a concentration gradient). Iodide-triiodide (I^-/I_3^-) is the conventional and most referenced redox couple in DSC research, due to its long is of desirable properties. However, it suffers from a number of shortcomings such as competitive light absorption and corrosiveness towards metal contacts that hinder their use in the development of durable devices with a long product life time[41]. A thorough literature review of the characteristics of redox mediators and a description and comparison of the vast range of alternative materials employed is provided in section 1.4.1.

Additives. To reach the high efficiencies of modern DSCs, additives are incorporated into the electrolyte to improve both interfacial charge transfer dynamics at the dye/TiO_2 interface as well as the conductivity of the electrolyte (Figure 7). A common additive is 4-*tert*-butylpyridine (TBP), which is a basic pyridine molecule that has the ability to adsorb onto bare TiO_2 surfaces through coordination of its lone pair of electrons on the nitrogen atom. An interfacial TBP layer can then formed, avoiding direct contact between TiO_2 and the infiltrating electrolyte and thus blocking any wasteful recombination reactions that limit the J_{SC} of the device[42–45]. Moreover, due to the high electronegativity of the pyridine ring and electron-donating property of methyl group, TBP possesses a net dipole moment which can lead to a favourable upward shift of the conduction band[44,46,47], raising the V_{OC} attainable in a device but lowering the driving force electron injection and thus the J_{SC}. Other bases such as *p*-trifluoromethylpyridine (TFMP) and (NMBI) are also used to a lesser extent, but nonetheless, have resulted with similar effects to that of TBP base[48]. The salt additive, bis(trifluoromethanesulfonyl)imide (LiTFSI), is also commonly added. When dissolved, Li^+ cations adsorb onto the negatively charged TiO_2 surface, while the $TFSI^-$ anions remain in the vicinity of donor part of the oxidized dye molecule

to act a as counter charge for stabilization. Opposite to the effect of TBP, Li^+ ion adsorption resulting with a positive shift of the flatband potential, yielding an unfavourably lower V_{OC}, but at the same time enhancing electron injection efficiency and accelerating charge transport in the TiO_2, leading to higher current densities[49–52]. Overall, the main challenge is to find the optimum additive composition that realizes a good balance between all parameters.

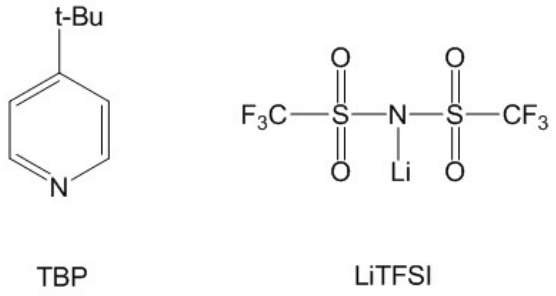

Figure 7. Chemical structures of common electrolyte additives; TBP and LiTFSI.

The Counter Electrode (CE)

Reduction of the oxidized redox species in the electrolyte or collection of holes from the HTM are the main purposes of the CE material. The over potential required to drive the charge transfer reaction gives rise to a charge transfer resistance (R_{CT}) which should be minimised to avoid significant losses of electrons. Thus, ultimately, the counter electrode material is chosen based on their catalytic ability and stability towards the particular redox species used in the electrolyte of the device, and should ideally possess a low sheet resistance to minimize the overall series resistance of the device. A large range of CE materials have been investigated for their employment in DSCs such as platinum, carbon and conductive polymers, employing a range of deposition techniques such as thermal decomposition, sputtering, spin coating and electrodeposition, each producing distinct morphologies that affect their ability to transfer charge[53].

1.3.2 Solid-State Dye Sensitized Solar Cells (ssDSCs)

Device structure and basic working principle. Despite the great achievements of the conventional liquid-based DSC, they do face a number of concerns linked to the use of a solvent (such as leakage, evaporation, desorption of dye, and corrosion of electrodes) that undermines their long-term stability. Thus, to alleviate these concerns, the ssDSC was developed in which the liquid electrolyte was replaced by a solid-state HTM (Figure 8). In contrast to the liquid DSC, a solid HTM is typically deposited by a spin-coating technique, on top of which a thin film of noble metal (typically Au or Ag) is deposited by thermal evaporation to serve as the counter electrode. ssDSCs therefore eliminate the need for a sandwich-based glass-glass type structure, leading to flexibility in design and lightweight devices. The basic working principle is equivalent to that of the conventional DSC, but instead, the HTM is responsible for regeneration of the photo-oxidized dye molecules and charge conduction across the cell. The mechanism by which charge conduction occurs is generally through a hole-hopping mechanism[54] in contrast to the shuttling (mass diffusion) mechanism of a redox mediator in a liquid electrolyte.

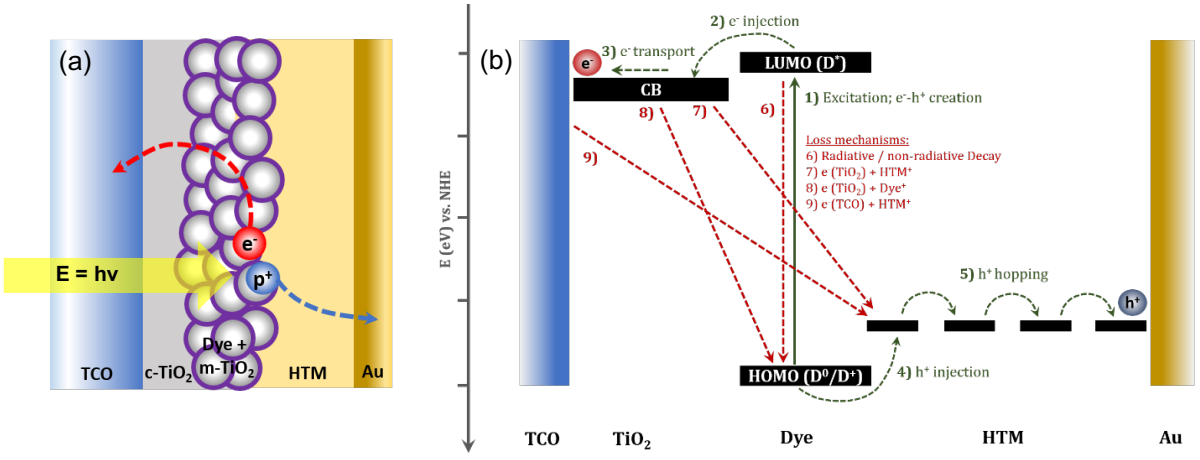

Figure 8. (a) Device architecture and **(b)** schematic of basic operation of a ssDSC.

The HTM. In aiming towards the future commercialization and up-scale production of solar cells, the HTM is typically deposited by spin-coating an organic-based precursor solution containing the HTM compound and certain additives. Spin-coating is the typical

technique of choice for depositing the HTM, due to the simplicity of the procedure and the ability to create uniform thin films, which allows for easy control over the HTM film morphology of nano-scale thickness by variations to the spin acceleration, speed, time and choice of solvent. Upon deposition and prior to spinning, the HTM is able to infiltrate into the pores of the semiconductor structure. During the spinning process, the solvent evaporates leaving behind a solidified HTM matrix within the pores of the semiconducting mesostructure and a capping layer formed from the residual solution on top of the mesostructure, that avoids direct contact (and therefore recombination) between the counter-electrode and the TiO_2 surface. As such, both pore filling ability, uniformity of the capping-layer, as well as the molecular alignment, orientation, morphology and overall conductivity of the formed HTM is heavily influenced by the solubility of the HTM molecules in the chosen organic solvent, and the volatility of the solvent itself.

Limitations and challenges. Despite the inherent advantages associated with the use of employing an all solid structure, the current record efficiency of ssDSCs built using the conventional monolithic solid-state architecture is still below the optimal device efficiency required to make them a competitive solar technology. This is a consequence of a number of factors, such as the 10 to 100 times faster recombination rate of injected electrons with holes in the HTM, gradual loss of contact between the HTM and dye layer/counter electrode, and it limited pore infiltration into the TiO_2 mesoporous structure[59–61]. These lead to an overall TiO_2 film thickness that is often limited to 2 – 3 μm, far thinner than that used for the conventional liquid DSC and far less than needed to achieve good optical absorption for most of the currently used sensitizers. Moreover, the devices exhibit poor reproducibility due to variations in the stability, charge transfer ability and conductivity exhibited by the HTM. Pore-filling ability has been identified as one of the limiting factors to the performance of the ssDSC. However, the evaporation of solvent during the spin-coating technique commonly used and eventual formation of a capping layer during the spinning process is what limits further infiltration of the HTM molecules to fill the pores which, for spiro-OMeTAD, results with less than ideal pore-filling fraction (PFF) of ~60%[62]. Theoretical calculations show increases to the PFF can

significantly improve the hole injection efficiency and lower recombination rates by 10-fold, and thus significant improvements to device performance expected with 100 % PFF in thicker scaffolds[63]. Equally as important to pore-filling ability of a CTM is the pore-wetting ability, which ensures good interaction for charge transfer. This is largely influenced by differences in hydrophobicity between the sensitized semiconductor's surface and the electrolyte / HTM precursor solution[62]. One approach to overcome the said issues is to develop novel HTMs that exhibit both excellent charge transport ability and stability, as well as good diffusion into the mesoporous scaffold for effective hole-transfer. Extensive research undergone over last thirty years ago—ranging from molecular or polymeric organic semiconductors to inorganic semiconductors (literature review provided in section 1.4.2)—however, none have succeeded the organic small molecule, spiro-OMeTAD, that was used in the first reported ssDSCs[64], and remains as the HTM of choice for producing high-efficiency monolithic solid-state devices[7].

Record performance. The best-performing ssDSC employing the traditional monolithic device architecture uses the spiro-OMeTAD HTM in conjunction with the organic LEG4 dye (7.7%), Figure 9.[55] However, in a more recent breakthrough, the "zombie" ssDSC which employs the same glass-glass sandwich-type structure as that of the traditional liquid-based DSC, has been able to exceed the 10% efficiency mark when employing $[Cu(tmby)_2]^{+/2+}$ as the HTM and the organic Y123 dye (11%), Figure 10.[56] This record performance is largely attributed to the ~3 to 4 times thicker TiO_2 scaffold enabled by the use of a small HTM molecule with good infiltration. In both cases, the additives LiTFSI and TBP—like those typically used in the electrolytes of DSCs—are added to the HTM precursor solutions, improving the overall conductivity of the resultant HTM film (up to 3 orders of magnitude for spiro-OMeTAD in the presence of oxygen and moisture[57], see section 1.4.2 for more details). Aside from conductivity enhancements, the interfacial effects of LiTFSI and TBP additives on the performance of ssDSCs—though slightly more complex—are believed to be the same as that found for liquid DSCs[58]. A thorough literature review of the characteristics of HTMs in general, as well as a detailed description of spiro-OMeTAD and the vast range alternative materials employed as HTMs is provided in section 1.4.2.

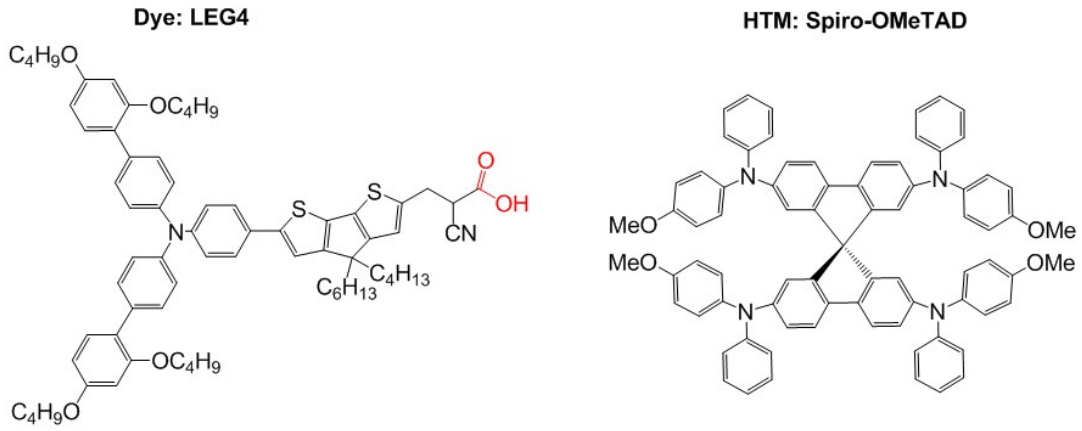

Figure 9. Components of the record performing monolithic-based ssDSC.

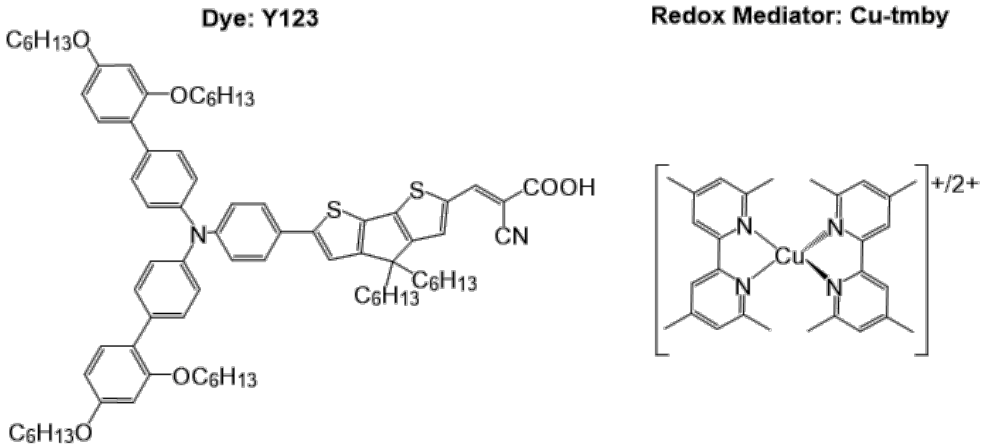

Figure 10. Components of the record performing sandwich-based ssDSC.

1.3.3 Perovskite Solar Cells (PSCs)

In an effort to push efficiencies of ssDSCs further, one major breakthrough was the replacement of dye molecules with a perovskite material of high optical absorption cross-section. This ultimately led to the emergence of the PSC. Today, PSCs attract prominent attention due to the rapid rate at which the power conversion efficiency has increased over the recent years—from an initial 3.8 %[65] conversion efficiency in 2009 to a record 22.1 % in 2017[66]—and the extremely low amounts of perovskite material it requires through simple processing techniques.

The perovskite light absorber. Perovskites form a class of materials that possess the same type of crystal structure with general formula, ABX_3, where A and B are cations (A larger than B) and X are the anions such as iodine, bromine or chlorine as depicted in Figure 11. A large number of perovskite compositions—tuned via cation and halide selection—have been investigated, resulting with optical bandgaps between the range of 1.5 and 2.3 eV[67–69]. So far, methylammonium lead iodide has received the most attention, with high short-circuit current densities > 20 mA cm^{-2} and open circuit voltages > 1 V routinely reported. Its bandgap of 1.54 eV, corresponding to an absorption onset of about 800 nm, and a valence band (VB) position of 5.4 eV vs. vacuum makes them the ideal candidate to be used in conjunction with the electron transporting materials (ETMs, typically TiO_2) and HTMs that have been traditionally employed for ssDSCs[69,70]. On the other hand, bromide-based perovskites typically possess higher band gaps, making them particularly suitable for tandem devices which demand high voltages[71]. However, due to incompatible energy levels the typical HTMs available, these perovskites have been much less explored to date.

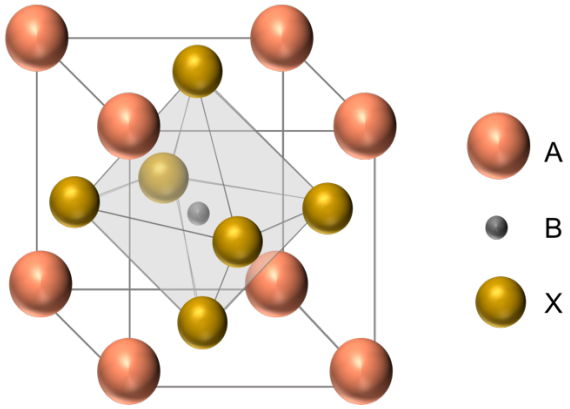

Figure 11. Schematic of the perovskite ABX_3 structure where A is the larger cation that occupies cubo-octahedral sites and shared with twelve X anions, while the B is the smaller cation that adopts an octahedral site and shared with six X anions.

Device architectures. At the beginning of its discovery, the perovskite solar cell was just a simple adaptation of the DSC, where the dye molecules were replaced with perovskite nanoparticles adhered to the TiO_2 mesoporous surface[11]. The operation of the PSC was therefore initially thought to be similar to that of ssDSC, whereby electrons are injected into the conduction band of the TiO_2 following the initial excitation step of the perovskite material. However, with unprecedented efficiencies over 10% being reached using an

electrically inert Al_2O_3 mesoporous scaffold, it was soon realized that—apart from absorbing photons—the perovskite material had the ability to act as an efficient ETM[72,73]. Further studies now show the perovskite to be a highly efficient, ambipolar charge-conductor [74], exhibiting a long carrier diffusion length[75] and small exciton binding energy[76], that allow it to perform the three key tasks of light absorption, electron transportation and hole transportation that proceed in three different materials in the conventional DSC. Thus, with the very unique properties of perovskite materials and the surprisingly high tolerance to defects[77–80]—a number of different configurations have been developed in its short time of its existence, some of which eliminate the use of an ETM[72,81] or HTM[82], or even those which do not employ the traditional monolithic thin film configuration[83,84]. The physical mechanisms of the operation of the PSCs are significantly different to that of the DSC. However, the use of charge-selective layers has been identified as being crucial to achieving high efficiency PSCs[85]. As such, the main two configurations that have been most commonly adopted are shown in Figure 12a-b. Here, the perovskite material is sandwiched between an ETM and HTM. As evolved from solid-state DSCs, the mesoscopic-based PSCs have a device architecture that is composed of a compact titania dioxide layer, a mesoporous metal oxide scaffold infiltrated by the perovskite and covered by a perovskite capping layer, and a p-type organic semiconductor film contacted by silver or gold. The planar-based PSC simply eliminates the use of the mesoporous scaffold.

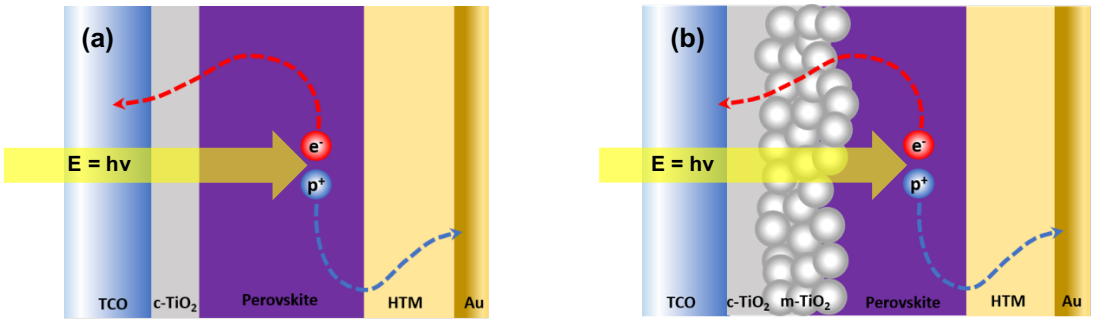

Figure 12. Device architecture of **(a)** planar and **(b)** mesoscopic PSCs.

Basic working principle. The energy level diagram, Figure 13, indicates the main charge-transfer processes that take place in the device architectures shown in Figure 12. First, the perovskite material performs its main task of absorbing incoming light, after

which the photogenerated electrons and holes are transported through the perovskite layer towards the charge selective contacts. Electrons are transferred to the TiO_2 conduction band, whilst holes are injected into the HTM, and collected on to their respective front and back metal contacts to generate current. In the mesoscopic structure, electrons can be collected directly and/ or via the TiO_2 layer. The ambipolar behaviour and extremely high absorption coefficient is what enables the use of ultrathin layers of around 500 nm to absorb the complete visible solar spectrum[86] and thus a CTM with exceptional pore-infiltration is not required, unlike that in ssDSCs. The ETM —either a compact or mesoporous scaffold layer of TiO_2—deposited directly beneath the perovskite is used to efficiently extract photogenerated electrons from the perovskite layer towards to the TCO, whilst the HTM—usually an organic thin layer—is used to extract holes and transport them in the opposing direction towards what is typically a gold contact. Like that of their DSC predecessors, the undesirable processes include the recombination reactions, that is, the electron back transfer reactions at the TiO_2/ HTM and TiO_2/perovskite interfaces, and the hole back transfer reactions at the perovskite/HTM interface. Thus, in order to maximize device efficiencies, the charge recombination processes (red arrows) should occur on slower time scales than the process of charge generation, separation, and extraction (green arrows).

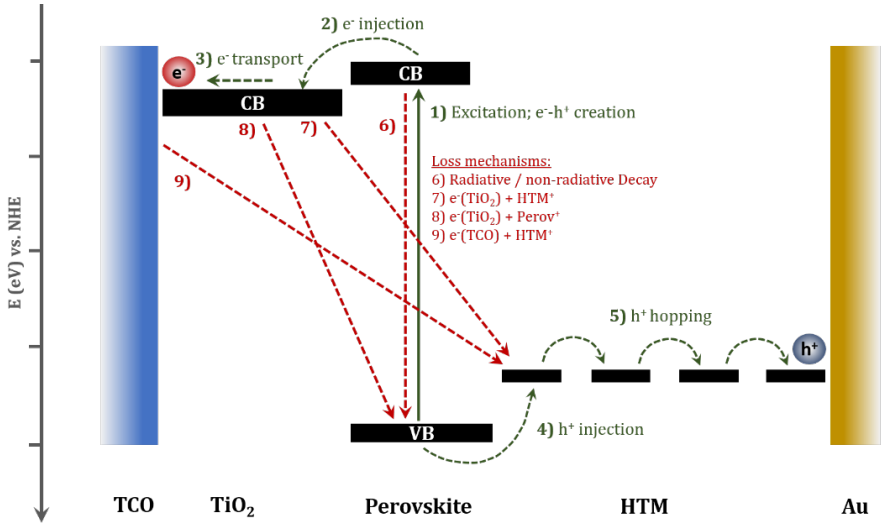

Figure 13. Schematic of basic operation of a PSC.

Challenges. Though it is not crucial, mesoporous TiO_2 layers have been shown to play a pivotal role in the formation of the perovskite crystal structure—improving reproducibility and reducing hysteretic behaviour among other things—and currently dominates in terms of overall efficiency[89,90] However, the costly high temperature fabrication process is one of their biggest downfalls, [72,81] making planar perovskite solar cells a more attractive and simpler option in terms of fabrication[81,87,88]. Aside from the severe doubts raised in terms of environment safeguarding over the use of lead as used in the highest performing devices, one of the biggest challenges faced by PSCs in general is their instability, significantly hindering their long-term device operation. The instability of PSCs has been found to be caused by several factors such as small variations in crystal size or structure[91], surface morphology[92], material composition[93], and ion migration at interface between different layers[94] and the presence of pinholes in the perovskite layer can have detrimental effects on the overall device performance and the important aspect of long-term stability[84]. Another challenge is the observation of hysteretic current–voltage behaviour (i.e. a discrepancy between the forward and reverse scans), a phenomena rarely seen in other solar technologies[95] and making accurate efficiency determination an ambiguous and challenging task.

1.4 Literature Review of Charge Transport Materials (CTMs) for Thin Film Solar Cells

Forming a key component in thin film solar cells is the charge-transport material. This thesis focusses specifically on the CTMs which serve the main purpose of regenerating the light absorbing material and then transporting holes towards the counter electrode. The following summarizes the general materials selection criteria that the CTM should possess for their success in a solar cell.

(i) **Compatible energy level.** Compatible energy levels between the light absorber and CTM are a fundamental requirement for the device to work. Ideally, the energy level of the CTM—that is, the redox potential of the redox mediator or the HOMO level of the HTM—should be as positive as possible to maximise the V_{OC} of the device, meanwhile maintaining a sufficient driving force for the regeneration of the light absorbing material.

(ii) **Good interfacial contact**. Direct interfacial contact between the CTM and light absorber is necessary for charge transfer to occur. For DSCs and ssDSCs, this means the CTM should possess good pore infiltration into the nm-sized voids of the TiO_2 scaffold and follows the curvature of the sensitized scaffold as much as possible for intimate contact inside the mesoporous scaffold.

(iii) **Good conductivity.** Following charge transfer between the CTM and light absorber, the charge should quickly move away from the interface, in order to prevent the wasteful recombination reactions from occurring and any build-up of charge that would otherwise increase the series resistance of the device and limit the overall charge collected at the metal contacts. Thus, a CTM with efficient charge transporting ability is essential. For electrolytes, this means that the redox species in solution should diffuse as fast as possible within the solvent of the electrolyte. Thus, the conductivity is largely dependent upon viscosity of the electrolyte solution which, in turn, is determined by the solvent and the concentrations of the electrolyte components, as well as the overall bulkiness of the redox mediator. For HTMs, the chemical composition (and/or doping

concentration), morphology, and processing methods all can have strong influence the charge transporting abilities, and for it which it is particularly important they exhibit *p*-type conducting behaviour with a high hole mobility that allow for a fast migration of holes away towards the counter electrode.

(iv) **Good stability.** To ensure the long-term stability of the device, the CTM must be non-corrosive towards the contacting materials, such as metal contacts and the light absorbing material, and be able to sustain the photoelectrochemical environment in which they would be operating under, that is, exposure to photons, electric fields and possible moisture.

(v) **Low absorption.** A CTM with a low absorption coefficient will avoid competitive absorption with the light absorbing material, which would otherwise limit the photocurrents attainable from the device.

A general description of the different classes of materials that have been investigated thus far for their use as a CTMs in solar cells are described in the following sections, highlighting both their key advantages and disadvantages.

1.4.1 Redox Mediators

1.4.1.1 Halogen-Based Redox Mediators

The conventional DSC redox mediator is iodide/tri-iodide (I^-/I_3^-), which, to date, has reached power conversion efficiencies of 12.1% and 10.2% in conjunction with ruthenium-based[96] and organic-based sensitizer[97], respectively. Its low cost, high stability, ease of preparation and small size that permits excellent infiltration with good mobility in and out of the mesoporous network have all contributed to their success as a redox mediator. Moreover, its complex multi-step dye regeneration mechanism involving the breaking of chemical bonds makes recombination between the injected electrons and the oxidized species I_3^- difficult to occur, leading to low recombination losses and long electron lifetimes within TiO_2 that enable large collection efficiencies[41]. Shortcomings using this redox mediator, however, are its competitive visible light absorption below 500 nm (limiting the photocurrent attainable), corrosiveness towards most metals and

sealants (complicating the design of large area DSC modules), and the large energy loss (up to 0.8 V) caused by its fixed redox potential of 0.37 V vs. NHE[41,98–100]. Moreover, the two-step dye regeneration mechanism of the I^-/I_3^- acts as an additional energy activation barrier for dye regeneration[101]. Other halogen-based redox systems such as Br^-/Br_3^- as well as mixed halogen systems (interhalogens) such as IBr_2^-/I_2Br^- with higher redox potential has since followed that permit the use of deeper HOMO level dyes yielding photovoltages greater than 0.8 V[49,102]. However, the inability to fine-tune the redox potential and the complexity in the equilibria established in such halogen systems has significantly limited further development.

The limitations and inherent issues faced using traditional halogen-based redox mediators has ultimately led to the employment of organic-based and metal complex-based redox shuttles which allow for structural modification and thus fine-tuning of physical and electrochemical properties. In particular, the development of redox mediators that minimize total energy losses—in particular, those which act in the one-step regeneration of the oxidized dye and those which possess higher redox potentials together with small driving force requirements for dye regeneration—have been key objectives.

1.4.1.2 Organic-Based Redox Mediators

A number of one-electron organic-based redox mediators have been reported, the first key examples being 2,2,6,6-tetramethyl-1-piperidinyloxy radical (TEMPO), tetrathiafulvalene (TFF) and N-(methoxyethoxyethyl)-phenoxazine (MEEP)[103,104]. Their simple one electron redox process with redox potentials as high as 0.8 V vs. NHE has enabled efficient dye regeneration and higher open circuit voltages in conjunction with low HOMO level dyes[105]. Of those reported thus far, TEMPO and its derivatives are the leading candidates, enabling DSC efficiencies as high as 5.4 % [106,107]. Efficiencies are significantly lower than their I^-/I_3^- predecessor attributed to their simple one-electron thiolate – disulfide redox mechanism that lead to faster recombination kinetics, as well as instability of the oxidized mediator and reaction with the sensitizer[105]. To combat the fast

recombination kinetics, thiolate – disulfide redox couples that embody a two-electron redox mechanism have also been developed reaching a maximum device efficiency of 7.9% employing the 5-mercapto-1-methyltetrazole (T^-) and 5,5′-dithiobis(1-methyl-1H-tetrazole) (T_2) redox couple[108–111]. However, the formation of high energy intermediates during the two-electron redox process necessitates a large driving force exceeding 600 mV for efficient dye regeneration, constituting a major potential loss.

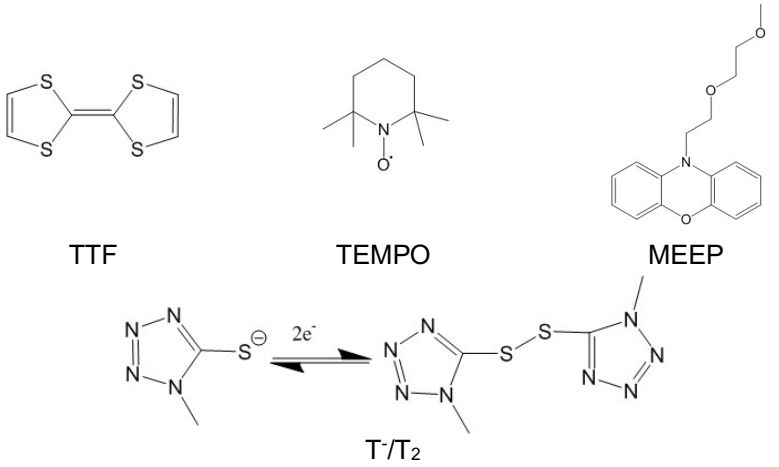

Figure 14. Selected published organic-based redox couples.

1.4.1.3 Transition Metal Complex-Based Redox Mediators

Composed of a metal center surrounded by organic ligand/s, a large number of transition metals have been investigated as redox mediators in DSCs, most of which are based on a cobalt, iron and copper metal centers[112], each discussed separately below.

Cobalt complexes. Hexa-coordinated Co(II/III)-based redox mediators are the most extensively studied transition metal-based redox couples for DSCs (Figure 15). Their success is a result of their single electron and reversible redox chemistry, favourable electrochemical redox potentials, negligible light absorption, non-volatility, non-corrosiveness towards the metal contacts used to build devices, and their ability to achieve more positive redox potentials that afford for larger V_{OC}'s in comparison to the halogen based redox couples. A wide selection of Co(II/III) complex electrolytes have been studied[112], the most successful of which are those based upon polypyridyl ligands such as bipyridine (bpy), terpyridine (terpy), phenanthroline (phen) and their

derivatives. With the advancement of new organic dyes and the use of co-sensitization electrodes, progressive improvements in DSC efficiencies employing polypyridal-based cobalt complexes have come about, reaching 13% with $[Co(bpy)_3]^{2+/3}$ in 2014, followed by 14.3% with $[Co(phen)_3]^{2+/3+}$ in 2015.[18,113]. The main performance limiting factors of Co(III/II) redox mediators, however, is mass transport of the bulky cobalt complexes through the mesostructured titania, poor stability due to possible decomposition through ligand exchange with other nearby components present in the electrolyte[114,115], and its relatively large internal reorganization energy during the transition from high-spin d^7 and low-spin d^6 states[116] which necessitates a driving force more than 0.25 eV for dye regeneration that constitutes a substantial potential loss[117–119]. Their carcinogenicity and poor long-term stability are what further limit their potential industrialization and mass production[115]. Research efforts to reduce the activation energy for change transfer have indeed taken place, such as the use of strong field ligands like (e.g. trithiacyclononane, ttcn) that force both the Co^{2+} and Co^{3+} oxidation states to adopt low-spin configurations, achieving quantitative dye-regeneration with a driving force of only ~ 200 mV[120]. This, however, lacked in terms of overall efficiency with a maximum 2% achieved. The development of novel cobalt complexes that employ pentadentate[121] and hexadentate[48] ligands, namely, $[Co(PY5Me_2)]^{2+/3+}$ and $[Co(bpyPY4)]^{2+/3+}$, with both improved thermodynamic stability and lower activation energies for charge transfer have also been applied as redox mediators, both of which were shown to outperform the archetypal $[Co(bpy)_3]^{2+/3+}$ complex.

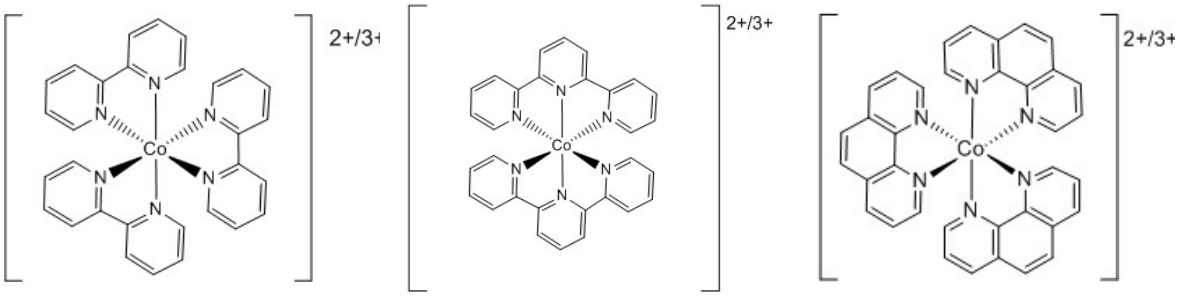

$Co(bpy)_3$ $Co(terpy)_2$ $Co(phen)_3$

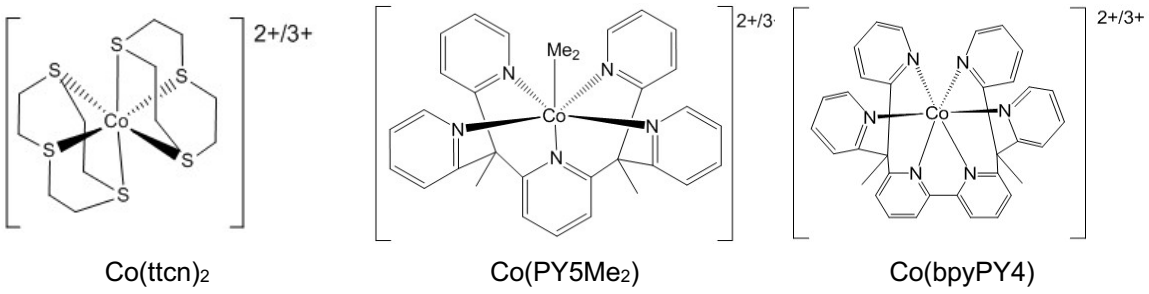

Co(ttcn)$_2$ Co(PY5Me$_2$) Co(bpyPY4)

Figure 15. Selected published cobalt complex redox couples.

Iron complexes. The abundance and lowered toxicity of iron makes iron-based complexes attractive alternatives to carcinogenic cobalt-based redox mediators. They are well-known to undergo kinetically fast one-electron outer sphere reactions as a result of their electronically close spin states[120], for which can overcome the high reorganization energy barrier experienced by the cobalt complexes. The ferrocene/ferrocenium (Fc/Fc^+) redox couple with well-defined electrochemistry was amongst the first to be investigated as an alternative redox mediator to cobalt complexes. When applied in a DSC, the Fc/Fc^+ was able to demonstrate itself as an excellent dye regenerator, but, at the same time, exhibited rapid interfacial recombination of photoinjected electrons, resulting with device efficiencies less than 0.6 % [122,123]. Techniques for passivating the dye-sensitized TiO_2 interface using poly(methylsiloxane)[124] or chenodeoxycholic[49] acid, or by the deposition of a compact TiO_2 film[124] to decrease the recombination rates by orders of magnitude have been of crucial importance. Their great potential was revealed when used in conjunction with a metal-free organic donor-acceptor sensitizer, Carbz-PAHTDTT that incorporates long spacer and bulky donor units to restrict the charge recombination from titania to ferrocenium, achieving an impressive efficiency of 7.5 %[49]. Here, a driving force of 0.20- 0.25 eV was identified to be ideal for efficient dye-regeneration. Other iron based complexes such as the $[Fe(CN)_6]^{4-/3-}$ redox couple in conjunction with the carbazole dye, MK2, constructed with aqueous electrolyte have achieved efficiencies of over 4% [125]. In general, however, the lower device performances employing iron complex-based redox mediators have not been able to compete with those employing cobalt complexes and have therefore not undergone extensive investigation since.

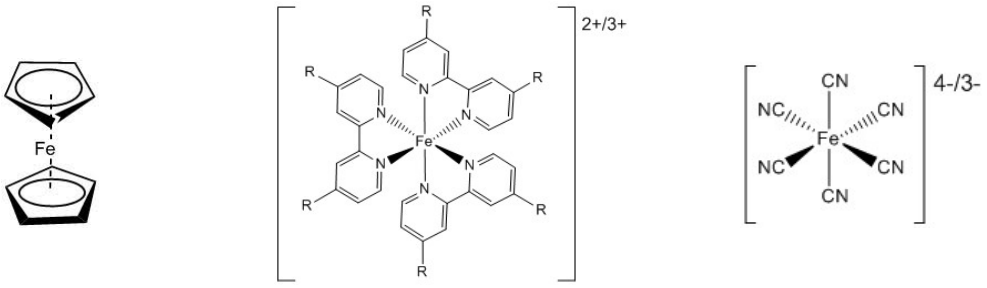

Figure 16. Selected published iron complex redox couples.

Copper Complexes. Copper is a low-cost, environmentally friendly metal, making copper-based complexes as attractive redox mediators for DSC applications. Unlike the aforementioned cobalt and iron complexes, copper complexes undergo a change coordination geometry as a function of their central metal oxidation state; Cu(I) complexes generally adopt 4-coordinate tetrahedral geometries while the Cu(II) complexes typically adopt 5-coordinatate square pyramidal, 5-coordinate trigonal bipyramidal, or 6-coordinate octahedral geometr[126]. Thus, the redox transition between Cu^{1+} and Cu^{2+} usually involves large activation energy. This is overcome by employing ligands that maintain the coordination around copper metal center during the redox transformation[127]. Key examples include $[Cu(SP)(mmp)_3]^{-1/0}$ and $[Cu(dmp)_2]^{+/2+}$ (Figure 17). Initial attempts employing $[Cu(dmp)_2]^{+/2+}$ as a redox mediator were rather low with power conversion efficiencies of only 1.4% in 2005[128] reached. However, the development of new organic dyes later increased the record to 7.0% in in 2011[105], and more recently 10.3% in conjunction with the high absorption coefficient organic dye, Y123, in 2016[129], revealing Cu(II/I) complexes as a viable alternative to that of the traditionally employed cobalt complexes requiring small driving forces of 0.1 V for efficient dye regeneration [105]. Other key examples of copper complexes in which the ligands were designed to attain small and distorted geometries and correspondingly low reorganization energies for efficient charge transfer include the bipyridyl-based complexes, $Cu(dmby)_2$ and $Cu(tmby)_2$, reaching efficiencies exceeding 10%[118]. A copper complex redox couple featuring a tetradentate ligand, Cu(oxabpy) has also been introduced as a redox mediator in a DSC, attaining a 6.2% power conversion efficiency[130], largely attributed to the slow recombination kinetics of excited electrons between the

TiO_2 and $[Cu(oxabpy)]^{2+}$ species and long electron lifetimes. Despite yielding viscous gel-like solutions, Cu(oxabpy) was found to exhibit better charge transport characteristics in comparison to $Cu(tmby)_2$, attributed to a superposition of mass diffusion and hole hopping between copper centers.

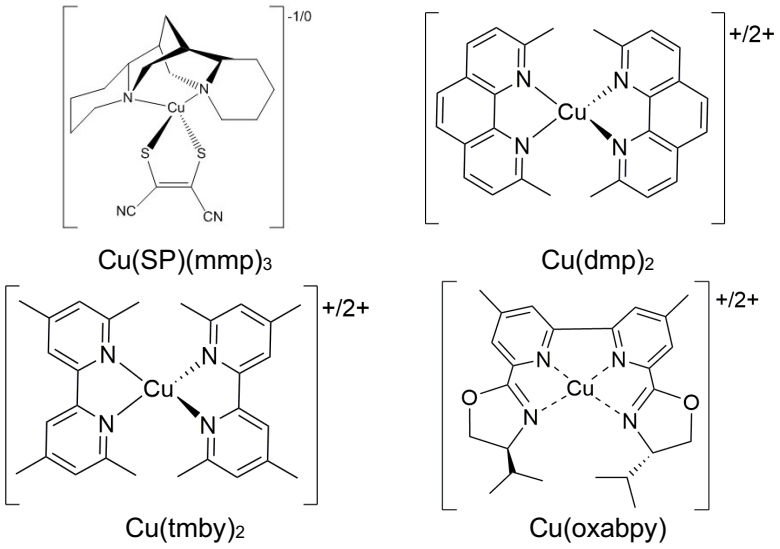

Figure 17. Selected published copper complex redox couples.

1.4.2 Solid-State Hole Transporting Materials (HTMs)

1.4.2.1 Inorganic P-type Semiconductors

Inorganic p-type semiconductors are attractive materials as HTMs because of their low-cost and ease of synthesis. They fulfil a number of key requirements such high transparency in the visible region, high stability (in comparison to organic HTMs that are often prone to photodegradation), and high charge-carrier mobility (usually orders of magnitude higher than organic materials). The latter is a consequence of their three-dimensional crystal structure that enables better charge transport compared to organic semiconductors. However, with these ideal characteristics, only a few have been successful applied due to the lack of p-type semiconductors that are solution processible. Among those that have been successfully applied are the copper-based inorganic semiconducting HTMs, for which CuI and CuSCN have received the most attention, and other such as CuBr, NiO, Cu_2O and CuO, the latter three of which have only been applied

in PSCs. These have been reviewed thoroughly[131]. Photo-conversion efficiencies of 4.5% and 2% using CuI[132] and CuSCN[133], respectively, have been attained when applied in a ssDSC, deposited through solution processing techniques that enable good pore-filling. The main shortcomings, however, are their uncontrolled crystallization during their deposition, leading to the gradual loss in contact to the sensitizing dye and counter electrode for efficient hole extraction thus leading to severe stability issues[134]. The use of crystal-growth inhibitors such as 1-methyl-3-ethylimidazolium thiocyanate or triethyl ammonium thiocyanate (THT) to counteract crystallization have been reported[135–137], demonstrating greater stability but with lower efficiency due to their hindrance on charge transport. Improved contact between the CuI HTM and dye molecules through interfacial engineering at the dye and counter electrode interfaces have been a more successful approach[138–140], leading to significant improvements in the efficiency reaching 7.4 %. Nevertheless, the efficiencies are still far lower than that liquid electrolyte-based DSCs due to the significantly higher recombination kinetics that lead to low fill factors and high photocurrent losses[140]. The use of an inorganic metal halide perovskite, $CsSnI_3$, as a hole-conductor has also been applied in a ssDSC, reaching a conversion efficiency of 8.5%[141]. However, due to the high absorption coefficient of $CsSnI_3$ and no IPCE measured in the infra-red region, the true origin of the high photocurrents measured have not been clearly understood. The application on inorganic HTMs in the wide range of PSC architectures have indeed been investigated, yielding maximum conversion efficiencies of 15.4%, 18.0 % and 13.58% utilizing NiO, CuSCN and CuI, respectively [142–144], showcasing both high efficiency and improved thermal stability. The biggest drawback for the use of inorganic HTMs in PSCs, however, is the oxidation-induced degradation and partial dissolution of the perovskite layer, compromising the long-term device stability[145]. Cu_2O-based PSCs have enabled the formation of highly uniform and high coverage perovskite films, and have thus far reached conversion efficiency of 13.35%[124]. However, theoretical simulations rank Cu_2O-based PSCs to exhibit the highest efficiencies (24%) amongst all other inorganic HTMs investigated as well as spiro-OMeTAD[146].

1.4.2.2 Coordination-Based Metal-Organic Complexes

Coordination metal-organic complexes offer a number of desirable attributes, such as simple synthesis, high charge-carrier mobilities, and high thermal stability, making them particularly ideal for their use as HTMs. Their application as HTMs in ssDSCs and PSCs are very few, and only recently have gained significant attention during the intense search for low-cost alternatives to spiro-OMeTAD for PSCs in particular. Of those investigated, phthalocyanine (Pc)-based metal complexes have been the main subject of investigation. They present themselves with high conductivities up to 10^{-2} cm^2 V^{-1} s^{-1}, owing to their stacked configuration that allows for conjugation of their macrocyclic ligand structures[147] and for which can be tuned by coordination with a range of metals such as Zn, Al, Ti and Cu[148]. In the simplest form, an efficiency of 15.4% is reached with CuPc[149]. Due to its lack of solubility in common solvents, its deposition relies on the use of expensive deposition techniques such as thermal evaporation, heavily limiting their scope of application. One successful approach to improving solubility as well as assist in the molecular orientation on top of the perovskite layer to enhance carrier mobility is through the modification of the ligand with alkyl-substituted functional groups[150–152]. Impressive efficiencies of 17.8% and CuPrPc has been reported in the absence of any dopants[153]. More recently, a molecularly bulky triphenylamine-based copper complex, CuH, with a twisted and nonplanar structure has been applied as HTM in a PSC, achieving an efficiency of 15.75% higher than was measured for spiro-OMeTAD under the same conditions[154].

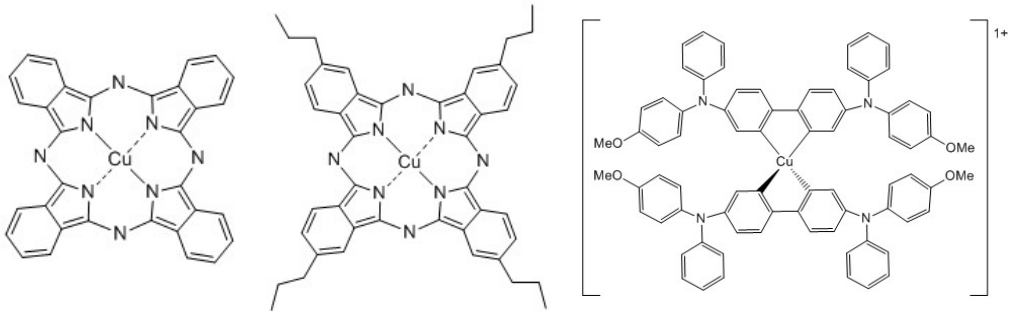

CuPc CuPrPc CuH

Figure 18. Selected published coordination-based metal organic HTMs.

1.4.2.3 Conjugated Polymers

Conducting polymers present themselves with remarkably high conductivities and hole mobilities (10^{-3}~10^{-2} cm^2 V^{-1} s^{-1})[155]. This is due to the strong overlap of electronic wave functions along the polymer backbone that creates a system of delocalised π-electrons, which, when the material is doped by oxidation, attains high mobility. In addition to the oxidation level of the polymer, chain alignment, interchain interactions, conjugation length, and their degree of disorder are key factors which can influence the overall conductivity and hole mobility. A vast range have been investigated for both ssDSCs and PSCs, including those based upon poly(3-hexylthiophene-2,5-diyl, (P3HT)[156,157], poly (3,4-ethylene dioxythiophene) polystyrene sulfonate (PEDOT:PSS)[158,159], and poly-triarylamine (PTAA)[66]. The main drawbacks of the use of polymeric HTMs include their complex purification process, material inconsistencies, and, most significantly, their poor solubility in organic solvents due to their high molecular weights that limits their ability to be deposited through solution processible technique, the method of choice when aiming towards large scale production. For ssDSCs in particular, their poor solubility heavily restricts pore infiltration into the mesoporous electrodes, leading to inefficient regeneration of oxidized dye molecules and a higher probability of charge recombination[160–163]. What's more, large conjugated chromophore groups integrated into the molecular structure of the polymer compete with light absorption by the dye and lowers the maximum attainable photocurrent. As such, device efficiencies no greater than 3.85 % have been achieved. In PSCs, however, the poor infiltration no longer becomes an issue due to the smooth perovskite capping layer formed. HTMs with high conductivity and mobility are therefore of the highest priority for PSC application. Competitive power conversion efficiencies have been reached utilizing the aforementioned polymers in PSCs, with efficiencies of 16.2% employing P3HT with a thickness of only 11 nm deposited by electropolymerization has been achieved, 18.1% with PEDOT:PSS, and a current record efficiency from any polymeric HTM of 20% reached with PTAA in conjunction with a mixed perovskite of PTAA showing negligible hysteretic behaviour.[66,164,165]

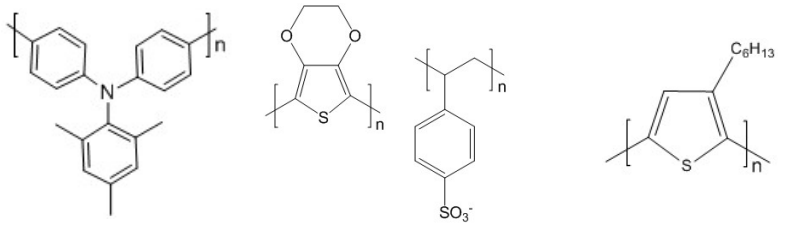

Figure 19. Selected published conducting polymers HTMs.

1.4.2.4 Small Organic Molecules

Small organic molecules as HTMs have acquired significant attention and research efforts and account for the majority of HTMs investigated for solid state solar cells as they can be strategically designed to match the band gaps of various light absorbing materials, as well as eliminate the issues of crystallinity and poor pore infiltration in mesoscopic structures that are often faced by inorganic and polymeric HTMs, respectively. Moreover, their weak light absorption, high solubility in organic solvents, electrochemical reversibility and tuneable electronic properties make them particularly attractive in the development towards solution processible solar cells. In such systems, charge is transported between the neighbouring molecules and moieties by a hopping mechanism[166,167].

Of those investigated thus far, triphenylamine (TPA)-based compounds are the most extensively studied small molecule HTMs[168] due to their high conductivity (Figure 20). Among those investigated, spiro-OMeTAD is the HTM often responsible for the highest efficiency solar cells reported in both monolithic-based ssDSCs[55] and PSCs[66]. Its suitably positioned HOMO level of 5.1 eV that provides sufficient driving force hole extraction from a large variety of dye and perovskite absorbers, as well as good hole mobility (when doped) in the range of 10^{-3} to 10^{-2} cm^2 V^{-1} s^{-1}, both key to their leading success as HTMs in solid state devices[169]. Furthermore, its solution-processability in non-polar organic solvents such as toluene and chlorobenzene (CBZ)—of which many perovskite materials are insoluble in—to form smooth thin layers serves as a major drawcard in their utilization. Its major downfalls, however, are its lengthy synthetic route and poor conductivity ($\sigma = 10^{-5}$ S cm^{-1}) and hole mobility (10^{-5} to 10^{-4} cm^2 V^{-1} s^{-1}) in its pristine

form[170,171]. The latter is a result of poor intra- and inter-molecular orbital coupling (low conjugated property) and the large intermolecular distances caused by the twisted spiro-carbon center in combination with the intrinsic lack of hole vacancies that does not allow for hole hopping conduction[171,172]. Thus, like most organic HTMs, spiro-OMeTAD requires p-type doping (described in section 1.3.2) A large handful of p-type dopants have been successfully applied, such as various Co(III) complexes[173,174], 2,3,5,6-tetrafluoro-7,7,8,8- tetracyanoquinodimethane (F4-TCNQ)[175], $SnCl_4$ [176], and silver bis(trifluoromethanesulfonyl)imide (AgTFSI)[177], that leads to the necessary improvement in electrical conductivity for their successful application as HTMs in solar cells. These not only adds costs but can exhibit poor solubility and high boiling points that limits their solution-processability. Nonetheless, the use of dopants are still strongly replied upon, the most commonly employed being LiTFSI and TBP (described in section 1.3.2), but which have deteriorating effects on the perovskite light absorber[178], and its high sensitivity to oxygen and light exposure makes reproducible and stable films difficult to achieve[179]. A key performance-limiting factor in ssDSCs is their low pore-filling ability, in which they have been found to achieve a maximum pore-filling fraction of only 60% for 2 – 3 μm thick semiconducting film[61,62], and dropping down to 40 % upon increasing the film thickness to 11 μm[61]. Various approaches have been made to improve to the poor filling capacity of HTMs and enable the use of thicker TiO_2 films have been developed, such as melt-infiltration processing[180], and the development of alternative organic molecules such as AS37 and AS44 of lower molecular weight, higher solubility and lower melting points[171], though optimized ssDSCs could not yield higher efficiencies than those utilizing spiro-OMeTAD. For PSCs, a significant amount of research has been undergone to which include those based on pyrene, thiophene and carbazoles have also attracted significant attention, achieving good chemical and environmental stability. Dopant free-based HTMs such as those based on tetrathiafulvalene (TTF) derivatives have shown huge potential as HTMs for PSCs[181,182], as well as fluoranthene-based HTMs in which an impressive efficiency of 18.03% has been reached with BTF4 displaying both enhanced stability and mobility (up to 10^{-4} cm^2 V^{-1} s^{-1}).

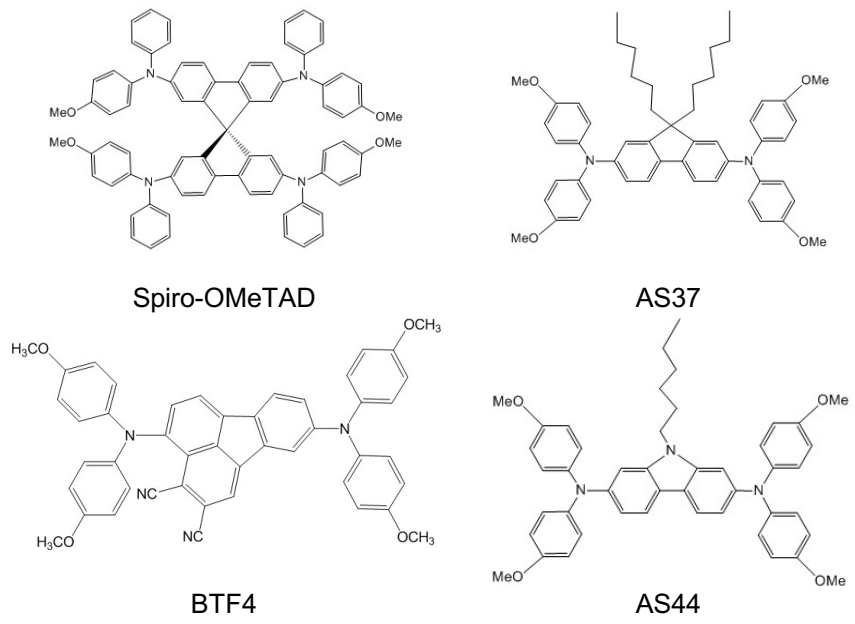

Figure 20. Selected publishes small molecule HTMs.

1.5 Thesis Scope and Outline

Transition Metal Complexes as CTMs for Thin Film Solar Cells.

Thin film solar cells based upon dyes and perovskite light absorbers are a promising and inexpensive solution to our future energy needs. Today, dye solar cells achieve record performance under diffuse and low-light conditions[143–146] (making them useful for indoor applications), whilst perovskite solar cells achieve among one of the highest single junction device efficiencies under AM1.5G simulated sunlight on record[66], approaching that of well-established silicon-based solar cells. As highlighted in section 1.3, forming a key component in dye solar cells and playing a vital role in high performance perovskite cells is the CTM. However, as learned from section 1.4, CTMs that are stable, solution-processible, cheap and simple to synthesize, with the ability to attain good pore infiltration (for dye solar cells particularly) and that which possess exceptional charge transport and interfacial charge transfer ability are key aspects that are lacking. As such, the field's attention has largely focussed on the development of new CTMs, which has led to many publications and a steady progression in device efficiencies over the years.

In line with the fields' trends, this thesis explores the applicability of transition metal complexes as solution-processible CTMs. The ability of the metal ion center to alternate between two (or more) oxidation states to perform intermolecular charge transfer is what makes them particularly worthy for exploration as CTMs. Furthermore, their generally good thermal and chemical stability, solubility, ease of synthesis, and the natural abundance of rare earth elements makes transition metal complexes appropriate for the future development of thin film solar cells on an industrial scale.

Background Theory

For transition metal complexes, the activation energy for charge transfer, whether it be homogeneous (self-exchange reactions between itself) or heterogeneous (reactions between different molecular species, such as at electrode interfaces), can be explained by Marcus' Theory[16,187]. According to this theory, an important factor affecting the rate of intermolecular

charge transfer is the reorganization energy, λ. This is the energy associated with the internal readjustment of the complex species involved (inner-sphere reorganization, λ_i), and the reorganization of the surrounding molecules (outer sphere reorganization, λ_o). In general, the smaller the geometrical differences—such as the metal-to-ligand bond lengths and angles resulting from changes in their electron density and orbital configurations—the smaller the inner-sphere reorganizational energy will be. A schematic representation of Marcus' theory describing intermolecular charge transfer is provided in Figure 21, showing the potential energy curves of the reactants (left) and products (right), which, when solved for the point of intersection, provides the free energy of activation, ΔG^*, given by:

$$\Delta G^* = \frac{(\Delta G^0 + \lambda)^2}{4\lambda} \qquad \text{Eq. 1}$$

where λ is the total reorganizational energy (i.e. the sum of the inner, λ_i, and outer-sphere, λ_o, reorganizational energies) and ΔG^0 is the Gibbs free energy for the process. The corresponding rate constant for the electron transfer reaction, k_{et}, is given by

$$k_{et} = kv \cdot \exp\left(\frac{-(\Delta G^0 + \lambda)^2}{4\lambda KT}\right) \qquad \text{Eq. 2}$$

where K is the Boltzmann constant, T is the absolute temperature, v is the nuclear frequency factor and k is the transmission coefficient (a measure of the probability of the system to progress from the reactant to the product states once it has surpassed the intersection of the potential energy curves).

Thus, according to Eq. 1 and Eq. 2, a small reorganization energy would result with a more easier and rapid charge transfer reaction, which is generally desirable for solar cells applications (discussed in section 1.3.1.1) as it can promote the following; (i) faster regeneration / hole extraction from the light absorbing material with a smaller driving force requirement, and so maximizing the open circuit voltage attainable in a device, (ii) faster rates of electron re-capture at the counter electrode and so minimizing series resistance in a device, and (iii) faster self-exchange that can facilitate charge conduction within the bulk material itself.

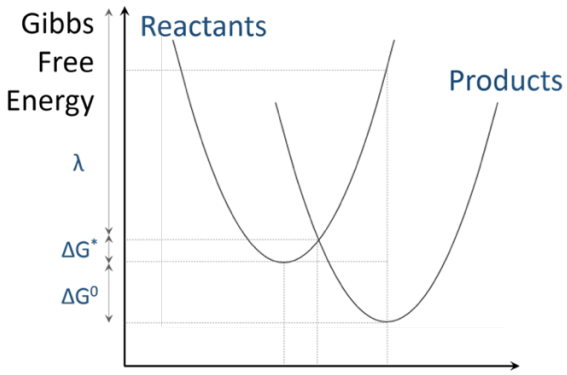

Figure 21. Free energy curves for an electron transfer process as described by Marcus' theory, showing the key kinetic parameters.

For transition metal complexes, the reorganization energy is dependent upon a number of key factors such as the electronic spin configuration (spin state) of the metal center, and the steric environment of the metal coordination sphere[188]. Iron complexes, for example, typically exhibit extremely low reorganization energies due to their low-spin states[189]. Cobalt and copper complexes, on the other hand, tend to exhibit larger reorganization energies; for cobalt complexes, this is largely attributed to the spin changes that take place between the typically high-spin Co(II) and low-spin Co(III) ions during the charge transfer[120], whilst for copper complexes it is largely dominated by the geometrical changes it experiences going from a 4-coordinate to a 5-coordinate system[128]. Nonetheless, depending upon the type, number and strength of the metal–ligand bonding interactions that arise upon coordination, the surrounding ligand can play a dominating role over both the electronic configuration and overall geometry of the coordination sphere of the metal center. Thus, for a given metal center, control over the reorganization energy and the associated activation energy for charge transfer can be achieved through ligand design.

The Strategy

Transition metal complexes possess huge potential to guarantee the necessary flexibility to develop CTMs that are capable of meeting the electrical (and electrochemical) requirements that are fundamental to achieving highly efficient thin film solar cells. The strategy used in this thesis specifically was to employ transition metal complexes with the ligands rationally designed to attain a *low* activation energy barrier which, when combined with large

electronic coupling[191], can provide a highly efficient mechanism for charge conduction and interfacial charge transfer.

Indeed, as highlighted in section 1.4.1.3, transition metal complexes have already garnered significant attention as redox mediators for DSCs. However, with the vast range of possible structures and designs yet to be implemented, they continue to take lead the field and there is still major room for improvement in the development towards high efficiency DSCs exceeding 20% predicted in literature[190]. The application of transition metal complexes as HTMs for ssDSCs and PSCs have also been demonstrated (see section 1.4.2). These works, however, focus mainly on highly conjugated macrocyclic planar systems such as phthalocyanines and porphyrins [192–194] or π-conjugated extended molcules[195,196] that allow for pi-stacking of its molecules. When used as a HTM, the metal cation adopts a single oxidation state and, without the metal cation present, the organic ligands by themselves exhibit high conductivity[197]. Thus, the excellent charge transport properties exhibited by these systems is largely attributed to the growth of stacked configurations that allows for pi-pi overlap between layers and not attributed to the redox transformation of the metal complex. The use of non-planar transition metal complexes in solid-state devices are mostly limited to p-type dopants in organic-based HTMs to improve conductivity[173,174,198–201], and only two examples exist in which non-planar complexes applied as HTM themselves have been reported[56,202].

Thesis Outline

The transition metal complexes studied in this thesis include one electron outer-sphere transition-metal complexes of cobalt, iron and copper that employ polypyridyl based ligands for which the ligands were designed to suit the different coordination chemistries of each metal center. The compatibility of the newly developed and carefully designed complexes for solar applications were explored, which included thorough investigation of the electrical, morphological, electrochemical and optical properties of each complex. These are outlined below.

- In **Chapter 3,** a cobalt complex featuring a high-denticity hexadentate ligand was investigated and applied as a HTM in a ssDSC. The hexadentate ligand, designed to encapsulate the cobalt center and form a rigid structure, offers superior robustness and stability that is necessary for their application in solar cells. Films comprising a mixture of the oxidized and reduce forms displayed surprisingly high and metallic-like conductivity, despite its amorphous nature. This was in striking contrast to what was measured for the conventional spiro-OMeTAD HTM and that of the well-established Co-bpy complex deposited under the same conditions, highlighting the novelty of the newly developed HTM.

- In **Chapter 4,** an iron complex featuring the same high-denticity hexadentate ligand from Chapter 3 was investigated following a similar set of experiments. Unlike the cobalt analogue, the resistivity behaviour for both pristine and mixed films displayed atypical Arrhenius behaviour. The much higher redox potential for this iron complex necessitated the use of the deep valence band energy formamidinium lead bromide ($FAPbBr_3$) perovskite. Applied as an additive-free HTM in the PSC, this is highlighted as one of the first HTMs for perovskite solar cells in which the conductivity is provided solely by a redox transformation of a transition metal.

- In **Chapter 5,** two copper complexes featuring phenanthroline-based ligands were investigated as redox mediators for DSCs. The extremely fast reorganization energies of these complexes resulted with poor device performance when applied as redox mediators in the absence of the common TBP additive but improved dramatically in its presence. Thorough investigations revealed strong coordination of TBP with the Cu(II) species in solution is critical for attaining high device efficiencies.

Chapter 2:

Materials and Experimental Methods

The following chapter describes the materials, experimental methods and characterization techniques used in this thesis. The methods outlined provide only a broad description of the standard experimental procedures. Specific details concerning the materials and experimental methods used for each individual study are outlined in the results section of each respective chapter.

Materials and Experimental Methods.

Chapter contents

2.1 Materials

Dye-sensitized and perovskite solar cells comprise a wide selection of materials, with each material performing a specified function. Broadly speaking, they consist of four major components; the working electrode (also referred to as the photoanode or electron transporting material, ETM, most commonly TiO_2 on TCO) the light absorbing material (a monolayer of dye molecules or a thin layer of perovskite), the charge transport material (either a liquid-based electrolyte or solid-state HTM), and the counter-electrode (such as PEDOT-catalysed TCO or gold). Here, an overview of the specific materials used in fabrication of the solar cells employed in this thesis is provided. The procedures used for fabricating the devices are described in detail in section 2.3. Unless otherwise specified, all materials were purchased from either Alfa Aesar or Sigma-Aldrich and used as received. AgOTf (silver trifluoromethansulfonate) was sourced from Strem Chemicals Inc.

2.1.1 The Working Electrode

TCO. Commercially available fluorine-doped tin oxide (FTO) deposited on glass substrates (TEC8) were purchased from Dyesol, exhibiting resistivities in the order of 10^{-3} Ω cm and optical transmissions exceeding 80% [203] and were employed for all solar cells.

TiO_2 Mesoporous Films. In this thesis, mesoporous TiO_2 films were made using commercially available TiO_2 pastes (purchased from two different companies; JGC Catalysts and Chemicals Ltd, and Great). These pastes comprise of a mixture of TiO_2 nanoparticles and organic binders dissolved in EtOH:terpineol. The latter two components are incorporated into the pastes to help control the morphology/structure of during deposition, which are burnt/evaporated off during the high-temperature sintering process (see section 2.3.1), leaving behind a rigid structure of interconnected TiO_2 nanoparticles. The diameter size of the TiO_2 nanoparticles were chosen to be ~30 nm diameter which provided a large enough pore size for both dye attachment and electrolyte/HTM infiltration of the materials used in this thesis. For liquid DSCs only, TiO_2

particles of 400 nm diameter were used in addition to act as a scattering layer that improve chances of light absorption by the dye molecules.

2.1.2 Light Absorbing Materials

Y123 Sensitizer. For the DSCs and ssDSCs fabricated in this thesis, the D-π -A Y123 dye (purchased from Dyenamo, *product code*: DN-F05Y) was employed. Here, the electron-rich donor is an alkoxy-substituted triphenylamine group and the electron-deficient acceptor (anchoring) is a cyanoacrylate group. These are connected by a conjugated thiophene-based π-bridge. Long alkyl chains integrated into the structure of the dye are designed to avoid to aggregation due to π– π interactions and/or hydrogen bonding that is frequently encountered during the formation of the dye monolayers on the semiconducting surface. Having a high molar extinction coefficient of 48 000 M^{-1} cm^{-1}, a HOMO of 1.07 V vs NHE[204] and excellent stability at high temperatures[205], this dye has been shown to work exceptionally well in conjunction with cobalt and copper-based redox systems, yielding efficiencies exceeding 10%[113,206].

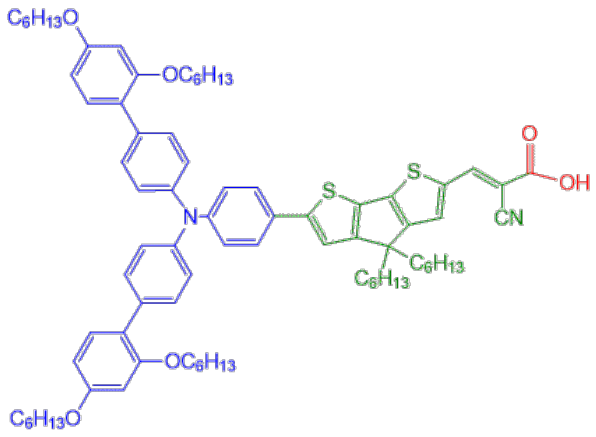

Figure 22. Molecular structure of a high performing Donor–π–Acceptor dye, Y123, used in this thesis. (donor = blue, π-bridge = green, acceptor = red)

$FAPbBr_3$ Sensitizer. For the PSCs fabricated in this thesis, formamidinium-lead-bromide ($FAPbBr_3$) was used. Compared to the many existing perovskite materials investigated to date, $FAPbBr_3$ is a perovskite material which is has received significantly less exploration due to its incompatible energy levels (HOMO = -5.83 vs. vacuum) with that of the typically

used HTMs employed. Nonetheless, an outstanding V_{OC} of 1.53 V and a conversion efficiency of 8.2% has been reported[207]. Despite their relatively lower efficiencies of fully bromide perovskites compared to their iodide-containing counterparts, they possess the close-to-ideal bandgap for tandem applications in which theoretical efficiencies of 43% have been predicted[208].

2.1.3 Charge Transport Materials

Redox mediators. The redox mediators used in this thesis are shown in Figure 23. $[Co(bpy)_3]^{2+/3+}$ is one of the most commonly used redox mediator in DSCs with a redox potential $E^0_{2+/3+}$ = 0.57 vs. NHE (V), achieving efficiencies as high as 13% when employed in conjunction with a co-sensitized electrode[18]. Given its success and commercial availability, it is often used as a control when testing the performance of newly developed redox mediators. $[Cu(dmp)_2]^{+/2+}$ is a complex of low reorganization energy exhibiting fast charge transfer kinetics and a low redox potential of $E^0_{+/2+}$ = 0.93 V vs. NHE, which together, enable the use of low HOMO level dyes to attain high open circuit voltages exceeding 1 V.[128,129] Though commercially available, all of $[Co(bpy)_3](OTf)_2$, $[Co(bpy)_3](OTf)_3$, $[Cu(dmp)_2](TFSI)$ and $[Cu(dmp)_2](TFSI)_2$ used in this thesis were synthesized in-house following published procedures, with the OTf or TFSI counter ions chosen to facilitate their solubility in the MeCN solvent of choice.

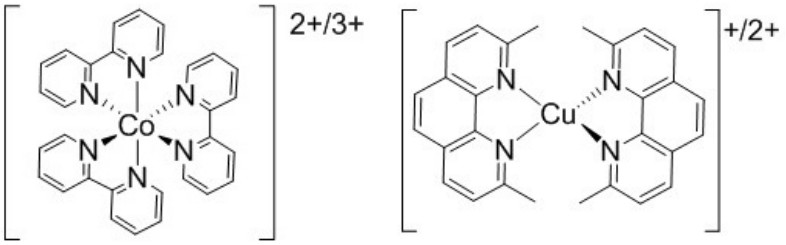

$Co(bpy)_3$ $Cu(dmp)_2$

Figure 23. Molecular structures of the cobalt and copper complex-based redox mediators, $[Co(bpy)_3]^{2+/3+}$ and $[Cu(dmp)_2]^{+/2+}$, used in this thesis.

HTMs. In this work, spiro-OMeTAD (> 99.5% HPLC purchased from Lumtec Technology Corp, product code LT-S922) was used as a reference to which the novel metal complex-based HTMs synthesized in this thesis are compared. Films were deposited by means of

spin coating a CBZ-based precursor solution (containing spiro-OMeTAD and the commonly used additives of LiTFSI and TBP) under inert conditions. Given its sensitivity to oxygen and moisture, the amount of exposure of spiro-OMeTAD films to water and oxygen were limited to only few steps during the fabrication and testing of devices , but were otherwise stored in a glovebox or dry box.

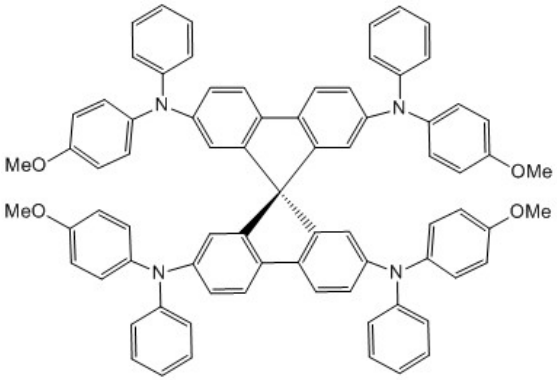

Figure 24. Molecular structure of the HTM, spiro-OMeTAD, used in this thesis.

2.1.4 Counter Electrodes

Platinum. Though being a costly noble metal, platinum has long been used as a standard counter electrode material for DSCs due to its high catalytic activity and excellent stability, in particular, towards I_2/I_3^- and cobalt complex based redox mediators[209,210]. For that reason, platinum has been the material of choice in the fabrication of the "zombie" ssDSCs that employ the novel cobalt complex HTM developed in this thesis. Here, platinized counter electrodes were prepared by the thermal decomposition of chloroplatinic acid solution, a method which has proven to be the simplest over other methods such as sputtering.

Poly(3,4-ethylenedioxythiophene) (PEDOT). Conducting polymers have been viewed as the ideal counter electrodes for copper-based redox mediators and were therefore employed as the counter electrode material of choice for the liquid-based DSCs fabricated in this thesis. Here, PEDOT was deposited by the electropolymerization of an aqueous solution of 3,4-ethylenedioxythiophene (EDOT) and sodium dodecyl sulphate (SDS) onto mesoporous ITO films. An SDS surfactant is used to help the formation of a highly organised and highly oriented array of PEDOT molecules and yields very homogenous

films[211], while the use of a mesoporous ITO layer is used to increase the surface area for catalytic reactions (improving the FF) as well as reduce the distance through which the redox mediators need to shuttle.

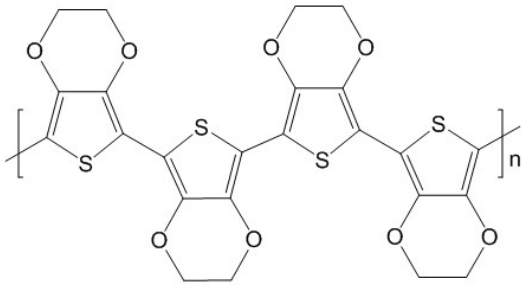

Figure 25. Molecular structure of the polymeric counter electrode catalyst, PEDOT, used in this thesis.

Gold. For monolithic-based solid-state solar cells, thermal evaporation of a noble metal with a high work function, such as gold or silver, are typically employed as counter electrode materials. For the PSCs fabricated in this thesis, gold was the material of choice as this was found to yield higher efficiencies compared to those made with silver and has been extensively employed in the research field due to its chemical stability.

2.2 Instruments and Characterization of Components

A detailed description of the instruments and general characterization methods used throughout this thesis is provided. The specific details of the parameters/techniques used are also provided and are referenced to their relevant section.

2.2.1 Optical Characterization

UV/Vis Spectroscopy of Solutions and Films. UV/Vis spectra were recorded with a Lambda 950 Perkin-Elmer spectrophotometer or an Ocean Optics Spectrometer set-up inside a glovebox. A 1 cm path length quartz cuvette and a standard detector was used for liquid-based measurements, whilst an integrating sphere detector was used for solid-state films that, unless otherwise specified, were deposited onto glass slides.

UV/Vis Titration Experiments of Complexes (specific to section 5.3.6.1). UV/Vis spectra were recorded using an Ocean Optics Spectrometer set-up inside a glovebox, and using a 1 cm path length quartz cuvette. Starting with a 6 mM stock solution of the complex in DCM in the cuvette, a 500 mM solution of TBP in DCM was added in 10 to 20 uL increments (the TBP amount equating to 0.1 eq. of the copper complex). With each addition, spectra were recorded at least three times (spaced at least 2 minutes apart) to ensure that an equilibrium state was reached.

Fluorescence Spectroscopy of Solutions and Films. Spectra in section 4.3.5 were recorded on a Horiba Jobin-Yvon FluoroMax-4 spectrophotometer and using a standard 1 cm path length quartz cuvette. Spectra in section 5.3.6.4 were recorded using the r Cary Eclipse Fluorescence Spectrophotometer (Agilent Technologies), using a 1 cm path length quartz cuvette with a septum screw cap through which titrations could be made using a needle.

Time correlated single photon counting (TC-SPC). The samples were excited using a Picoquant LDH-P-C-440 440 nm laser pulsing at 20 MHz with a pulse duration of at most 80 ps. The excitation polarization was set to the 'magic angle' to eliminate polarization

anisotropy. The laser power was 178 microWatts. Excitation and collection were at right angles to each other. Excitation was at approximately a 45 degree angle to the substrate. The excitation and collection were on opposite sides of the substrate to reduce the scattering of laser light into the detector. Photoluminescence was collected through a 500 nm long pass filter. The photoluminescence was monochromated using a Digikrom DK480 equipped with a 1200 grooves/mm grating blazed at 330 nm and set to 640 nm. Photon counting was performed using a Hamamatsu R3809U-50 microchannel plate and a Picoquant PicoHarp 300 counter. The average count rate was less than 10 kHz, which ensures pulse pile-up is negligible.

2.2.2 Electrochemical Characterization

Cyclic voltametric (CV) measurements for electrochemical characterizations were conducted inside a glovebox using a classical three-electrode configuration employing a platinum wire (as working electrode), $Ag/AgNO_3$ (as reference electrode) and a platinum mesh (as counter electrode). A Bio-Logic VSP potentiostat was used in CV mode to record current-voltage characteristics of the three-electrode set-up. Unless otherwise stated, measurements were performed at a scan rate of 100 mV s^{-1} on 3 mM solutions of the metal complex of interest in MeCN with 0.1 M $TBAPF_6$ as a supporting electrolyte. For calibration, a cyclic voltammogram of Fc in the same electrolyte was recorded at end of each measurement and the redox potentials of each metal complex converted with respect to NHE using the standard value Fc^+/Fc = 0.63 V vs. NHE in acetonitrile.

2.2.3 Morphological Characterization

Scanning electron microscopy (SEM). SEM was performed on a FEI Magellan 400 FEG microscope. Images were captured using an accelerating potential of 5 kV and a beam current of 6.3 pA.

Transmission electron microscopy (TEM). TEM was performed on a Jeol JEM-2100F FEGTEM (JEOL Ltd., Tokyo, Japan) operated at 200 kV. Images were collected using a Gatan UltraScan 1000 (2k × 2k) CCD camera (Gatan Inc., Pleasanton, CA, USA). Low

magnification bright-field (BF) TEM images were obtained using a 20 μm objective aperture and a defocus of −10,000 nm to heighten contrast from phase boundaries. High resolution TEM (HRTEM) images were obtained with no objective aperture and at Scherzer defocus, selected area diffraction patterns (SADPs) were obtained using a 120 μm selected area aperture, corresponding to areas of 750 nm in radius.

X-Ray Diffraction (XRD). X-ray diffraction (XRD) patterns of the films were recorded on a Bruker D2 Phaser X-ray diffractometer with Cu K_α radiation (λ = 1.54184 Å) with 0.02° resolution. Films were either spin-coated or drop-casted onto the substrate (either a silicon wafer or glass slide) and were performed at a scan rates of 1.2 and 0.2° min^{-1}, respectively.

2.2.4 Electrical Characterization

2.2.4.1 Electrolyte Conductivity and Charge Transfer

Catalytic activity (charge-transfer resistance) at the CE/electrolyte interface and the diffusion limitations of the redox mediator[212] have significant influences on the important solar cell parameters such as the series resistance (R_S), shunt resistance (R_{SH}, also referred to as the recombination resistance) and thus the overall FF. These were analysed by cyclic voltammetry of symmetrical counter-counter electrode devices, a technique that is often used[213,214]. Here, counter electrodes are fused together with a 25 μm hot-melt surlyn gasket forming a compartment into which the MeCN-based electrolyte solutions (identical to those used in devices) are filled through a pre-drilled injecting hole using a back-filling technique and aid of vacuum (Figure 26). Surlyn-coated aluminium foil heated to 120 °C was then used to seal the injecting hole by the application of pressure. Wires were soldered to each electrical contact for testing. A Bio-Logic VSP potentiostat was used in CV mode to record current-voltage characteristics of the symmetrical devices in the voltage range of -1 to 1 V using a scan rate of 100 mV s^{-1}, and with the reference lead in short circuit with the counter electrode.

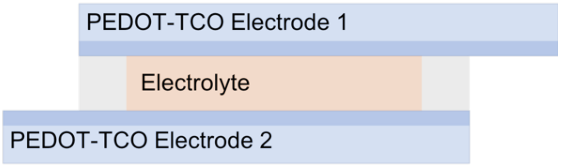

Figure 26. Symmetrical dummy devices used for electrolyte conductivity measurements.

2.2.4.2 Thin Film Conductivity

The solid-state conductivity of thin films is viewed as one of the most important parameters that needs to be evaluated for new HTMs. A variety of techniques exist for measuring conductivity, most of which can be categorized as being two-point or four-point probe techniques and simply involve measuring the I-V slope and sample geometry to calculate the conductivity. Here, the conductivity of films were measured on interdigitated array (IDA) microelectrodes (purchased from BAS ALS, Japan, *product code*: IDA-Au-10μm), which employs the two-probe configuration, Figure 27. The IDAs comprised of 65 gold electrode pairs spaced 10 μm apart on a quartz substrate, surrounded by a non-conducting passivation layer. Each electrode finger was 5 μm wide, 2 mm long and 90 nm thick.

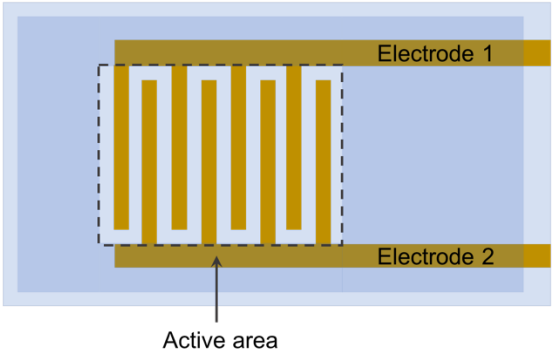

Figure 27. Schematic of interdigitated array (IDA) electrode used for thin film conductivity measurements.

Room temperature conductivity. Measurements were undertaken inside a glove-box to avoid exposure of samples to air. Prior to use, IDA electrodes were thoroughly washed with acetonitrile and dried under a stream of nitrogen. Solutions containing the material under investigation were then drop-cast onto the electrode so that the film was covering both the interdigitated area and the surrounding passivation layer. IDAs coated with such

thin films were then allowed to dry under the nitrogen atmosphere of the glove-box. A Bio-Logic VSP potentiostat in CV mode was then used to record current-voltage characteristics of the two-probe IDA electrodes.

Variable temperature conductivity measurements. Conductivity measurements over the temperature range 10-300 K were performed using a physical property measurement system that uses liquid helium. For these measurements, samples were exposed for a very short time to air upon transferring and loading into the sample chamber of the cryostat. The sample chamber was purged with helium gas and sealed at atmospheric pressure, and measurements undertaken starting at 300 K and cooling down in 10 or 5 K intervals. Using the Keithley 2400 SourceMeter, a potential was applied between −0.5 and +0.5 V at a scan rate of 0.10 V s^{-1}. The conductivities, σ, of the thin films were calculated from the slope of the acquired current-voltage curves by applying the relationship $\sigma = S(d/((2n-1)lh))$ [Sm^{-1}], where S is the slope of the linear fit to the experimental I-V data, d is the electrode spacing, n is the number of electrode pairs, l is the electrode length and h is the film thickness. The film thickness was measured using an optical profilometer on scratches engraved along both sides of the electrode area after acquiring the current-voltage data.

2.2.5 Transient Absorption Spectroscopy (TAS)

Nanosecond transient absorption spectroscopy (TAS) is tool that can provide an invaluable information about the kinetics of interfacial processes occurring within a solar cell. In this thesis, TAS is used to investigate the dye regeneration kinetics in a DSC. In such experiments, a dye-sensitized TiO_2 film is photo-excited by a laser, causing an electron to be injected into the TiO_2 film. The resultant oxidized dye returns to its ground state either by regeneration by the reduced species in the electrolyte, or recombination with the injected electrons in the TiO_2 film. Employment of an inert electrolyte devoid of any redox species (such that the dye cation can only recombine with injected electrons) is used to determine the recombination rate, k_{rec}, whilst an electrolyte containing the

reduced electrolyte species (such that the dye cation can become regenerated) is used for the determination of the dye regeneration rate, k_{rec}.

Sample preparation. Onto cleaned FTO substrates, ~1 um thick TiO_2 films (7 x 7 mm in dimension) comprising 30 nm-sized particles were screen-printed and sintered according to the process shown in Table 1. TiO_2 electrodes were heated with a heat gun at 500 ± 25 °C for 30 minutes prior to being immersed into a 3 μM solution of the dye in MeCN:toluene (1:1) for 24 hours. The dyed TiO_2 working electrodes were then fused to pre-drilled microscope glass slides (as dummy counter electrodes) with a 25 μm hot-melt surlyn gasket, forming a compartment into which the electrolyte solutions were filled through the pre-drilled injecting hole via a back-filling technique and aid of vacuum. Electrolytes comprised 10 mM of the reduced complex species dissolved in MeCN containing 0.1 M LiTFSI and 0.6 M TBP (if indicated). Once filled, the injecting hole was sealed with a sheet of surlyn-coated aluminium foil, with care taken to avoid blockage of the laser through the film.

Experimental set-up. Nanosecond visible transient absorption spectroscopy (ns-TAS) was employed to monitor charge separation dynamics. The measurements were conducted by a home-built transient absorption spectrometer with a home-built transient absorption spectrometer with a N_2 laser (OBB, OL-4300) pumped dye laser (OBB, OL-401, 800 ps pulse duration) as an excitation source. Transient absorption signal was probed by a Xe lamp (Photon Technology International) light through two monochromators (Acton, Princeton Instruments), and detected by a Si based nanosecond detection system (Unisoku Co., Ltd., TSP-2000SN, time resolution: 1.2 ns (FWHM), monitoring wavelengths: 400~1,100 nm) with a fast oscilloscope (Tektronix, TDS 3052C, Digital Phosphor Oscilloscope 500 MHz 5 GS/s) at 2 Hz excitation repetition rate. Transient data were collected with 500 nm excitation with excitation intensity of 3 μJ cm^{-2} at 22 °C

2.2.6 Magnetic Susceptibility

Experimental set-up. Magnetic susceptibility measurements were performed using a Quantum Design MPMS2 SQUID magnetometer. Magnetic samples were prepared by adding powdered crystalline compounds to a 7 mm diameter quartz tube with a raised quartz platform. The sample was restrained with icosane and sealed in the quartz tube. Direct current (dc) magnetic susceptibility data measurements were

2.2.7 Electron Lifetime Measurements

Intensity modulated photocurrent spectroscopy–Intensity modulated photocurrent spectroscopy (IMPS–IMVS). IMVS-IMPS complemented by charge extraction measurements was used to compare the electron lifetimes and electron transient times for DSCs assembled with Co(bpyPY4)-based CTMs as a function of the extracted charge. These measurements were carried out on complete DSCs comprising of 4.0 μm thick mesoporous films (average primary particle size 30 nm) sensitized with the organic dye Y123. The solar cell was kept under open circuit conditions and illuminated by a constant light intensity on top of which frequency modulated sine-wave illumination is added. This IMVS setup employed red and white LEDs as the light source with the light intensity controlled by DC voltage source. A Stanford lock-in-amplifier (SR810) was used to provide a sine wave modulation between 0.1 Hz and 30 kHz to the light source and a high impedance voltage follower with an input impedance of 1012 ohms was used to record the DSC's photovoltage response. The LabVIEW controlled system was employed to capture the amplitude and phase of the resulting AC photovoltages and a LabVIEW fitting program was used for the data analysis. Following each impedance measurement at each light intensity, the DSC was illuminated with unmodulated white light for 10 seconds to attain equilibrium between charge injection and recombination under open circuit conditions after which a computer-controlled mercury-wetted relay switch was used to turn off the light source and to put the device in short-circuit. The extracted charge was measured across a 50 Ω resistor, using an NI-

6251 data logger. All experiments were carried out in an earthed Faraday dark box to eliminate electrical noise.

2.3 Fabrication of Solar Cells

This thesis involves the fabrication of four different types of solar cells; a "zombie" solid-state DSC (Chapter 3), a planar perovskite solar cell (Chapter 4), and a liquid electrolyte-based solar cell (Chapter 5). In all cases, FTO glasses where used as the TCO substrate, which were washed before use in three main steps—first in a 1% v/v solution of Hellmanex in water, followed by water and ethanol, each time under sonication for at least 15 minutes and heating at 50 °C—and then dried under an air stream. Remaining details of the steps used in the fabrication of the solar cells are described in the following sections.

2.3.1 "Zombie" ssDSC (Chapter 3)

Compact TiO_2. A compact TiO_2 blocking layer was deposited on the FTO surface using the spray pyrolysis technique. Cleaned FTO substrates were placed on a hotplate and heated to 450 ºC with a ramp time of 30 minutes. After 5 minutes of heating at 450 ºC to ensure equilibrium temperature was reached, a solution of titanium diisopropoxide bis(acetylacetonate) 75% in isopropanol (1:9 v/v) was sprayed across exposed TCO surface, one round every 10 seconds, for 2 minutes, 12 rounds in total. Sprays were placed in each corner and in the middle to ensure full coverage of the TCO plate. After spraying cycles were complete, the substrates were left on the hotplate for a further 5 minutes at 450ºC before air cooling down to room temperature.

Mesoporous TiO_2. On top of the blocking layer, TiO_2 films (4 x 4 mm dimension) were screen-printed, layer by layer, to the desired thickness. A screen mesh size of 180T was used, which yielded ~1 um thick layers with each print (of the purchased Dyesol TiO_2 pastes), each layer heated at 125 °C for 15 minutes. The total thickness of the mesoporous films was ~10 μm for IV characterization (comprising ~6 μm of 30 nm-sized TiO_2 particles and ~ 4 μm of 400 nm-sized TiO_2 particles) and only ~4 μm thick for IMVS/IMPS measurements (comprising only the 30 nm-sized TiO_2 particles). After the final TiO_2 layer was printed, films were sintered according to the process shown in Table 1 to establish a necking between nanoparticles.

Table 1. Sintering process of TiO_2

	Step 1	Step 2	Step 3	Step 4	Step 5
Ramp (º/min)	10	15	5	7	5
Temperature (ºC)	150	325	375	450	500
Duration (min)	10	5	5	30	15

A $TiCl_4$ post-treatment of mesoporous TiO_2 films was done by immersing them into a 20 mM $TiCl_4$ aqueous solution inside a humidity chamber (a desiccator with lid closed) and heating at 70 °C for 30 minutes. The $TiCl_4$-treated TiO_2 electrodes were reheated with a heat gun at 500 ± 25 °C for 30 minutes prior to being immersed into a 0.3 mM solution of Y123 (purchased from Dyenamo) in a mixture of MeCN:toluene (1:1). After 24 hours of dying, the electrodes were removed from the dye solution and rinsed with MeCN to remove any residual dye.

Platinum CE. Platinum counter electrode were prepared via thermal decomposition of a chloroplatinic acid solution in a fumehood. FTO/glass electrodes of ~2.5 x 1.5 cm dimension were cut and, to the corner of each electrode, a ~1 mm diameter hole was drilled. After standard washing procedures, one to two drops of a 10mM platinic acid (H_2PtCl_6) solution in isopropanol was placed on the conductive side of each pre-drilled FTO electrode, smeared with the tip of pasture pipette, and then allowed to dry. With the active side up, electrodes were inserted into a ceramic tube and fired with a heat gun set to a temperature of 400ºC for 15 minutes and removed for cooling. Electrodes were used within 1 hour of their fabrication.

HTM precursor solutions. Acetonitrile-based HTM precursor solutions were prepared inside a glovebox. The $[Co(bpyPY4)](OTf)_{2.33}$ HTM precursor solution was prepared by dissolving $[Co(bpyPY4)](OTf)_2$ (87.7 mg, 0.20 M), $[Co(bpyPY4)](OTf)_3$, (51.3 mg, 0.1 M) in acetonitrile (0.5 mL), while the $[Co(bpy)_3](OTf)_{2.33}$ precursor solution was prepared by dissolving $[Co(bpy)_3](OTf)_2$ (82.5 mg, 0.20 M), $[Co(bpy)_3](OTf)_3$, (48.7 mg, 0.1 M) in acetonitrile (0.5 mL). For those containing additives, LiTFSI (7.2 mg, 0.05 M) and trifluoromethylpyridine (36.8 mg, 0.50 M) was added. contained Co(III) (200 mM) and

Co(II) (100 mM) in MeCN, as well as LiTFSI (100 mM) and TFMP (500 mM) where indicated.

HTM filling and device assembly. The working and counter electrodes were fused together with a 25 μm hot-melt surlyn gasket, forming a compartment into which the HTM precursor solutions containing the cobalt complexes were filled through the pre-drilled injecting hole via a back-filling technique and aid of vacuum. Removal of the MeCN solvent to obtain a solid HTM was achieved by repeated back-filling followed by a 4 h drying period on a hotplate heated at 70 °C. A glass cover slip backed with hot-melt surlyn was then used to seal the injecting hole. Wires were soldered to each electrical contact for testing immediately after device fabrication.

2.3.2 Planar PSC (Chapter 4)

Compact TiO_2. FTO substrates was patterned using a laser engraver (Universal Laser Systems, VLS3.50) and before being washed using the standard washing procedures (above). A compact TiO_2 blocking layer was deposited onto the FTO surface by spray pyrolysis, employing 2.8 mL of a titanium diisopropoxide bis(acetylacetonate) solution in isopropanol (1:9 vol.) and a substrate temperature of 475 °C. Prior to perovskite deposition, the FTO|c-TiO_2 substrates were further cleaned by ozone plasma for 10 min (Harrick Plasma, PDC-002; plasma intensity set to "high"; air pressure inside the chamber ca 1100 mTorr). All further procedures were carried out in a glove-box under a nitrogen atmosphere.

Perovskite and HTM. The perovskite precursor solution (30 weight %) was prepared by dissolving FABr (52.3 mg) and $PbBr_2$ (153.6 mg) in N,N-dimethylformamide (470 μL). After dissolution, a 47% w/w solution of HBr in water was added (23.4 μL). The spiro-OMeTAD solution was prepared by dissolving spiro-OMeTAD (20.6 mg) in chlorobenzene (250 μL). The [Fe(bpyPY4)](OTf)$_{2.5}$ solution was prepared by dissolving [Fe(bpyPY4)](OTf)$_2$ (21.9 mg) and [Fe(bpyPY4)](OTf)$_{2.9}$ (25.6 mg) in nitromethane (1 mL), giving a Fe(II):Fe(III) ratio of approximately 1:1. A ~1.2 cm^2 perovskite layer was deposited on the FTO|c-TiO_2 substrate by spin-coating 25 μL of the perovskite solution

at 4000 rpm for 30 s with an acceleration of 4000 rpm s^{-1}. Upon 3 s of the spinning, a 380 kPa nitrogen flow was applied for 10 s. The resulting film was annealed on a hotplate at 170 °C for 10 min. After cooling, an HTM layer was deposited by spin-coating either 25 µL of the spiro-OMeTAD solution at 3000 rpm for 30 s with an acceleration of 3000 rpm s^{-1}, or 18 µL of the $[Fe(bpyPY4)](OTf)_{2.5}$ solution at 2000 rpm for 40 s with an acceleration of 200 rpm s^{-1}.

Au counter electrode and final encapsulation. Using an appropriately designed mask, gold counter electrodes were deposited on top of the HTM film by means of thermal evaporation inside a glovebox. As a final step, a 80 nm layer of Au was deposited by thermal evaporation (DDong DD-GCMO3CR). Deposition started when vacuum reached 3 x 10^{-1} Torr. To ensure complete coverage of the exposed HTM film, a slow evaporation rate of 0.1 $Å s^{-1}$ was used initially, which was then increased gradually after 5 nm of gold was evaporated using a deposition speed 1 Å s^{-1} between 5 – 40 nm and 2.5 Å s^{-1} between 40 –80 nm. Device encapsulation was performed under nitrogen atmosphere (glovebox) by dispensing UV-curable epoxy resin from Lumtec (LT-U001) onto the edges of a cover glass with a recess in the middle (purchased from HanaAMT). The glass was then gently pressed on the solar cell devices before being illuminated under UV light (2.5 mW cm^{-2} , peak intensity at 365 nm) for 12 min.

2.3.3 Liquid-based DSC (Chapter 5)

Compact TiO_2. A compact TiO_2 blocking layer was deposited on the FTO surface using one of the following methods. Cleaned FTO substrates were immersed into a 20 mM $TiCl_4$ aqueous solution inside a humidity bath (a desiccator with lid closed) and heated at 70 °C for 30 minutes. Substrates were then removed from the bath, allowed to cool, then rinse thoroughly with distilled water followed by ethanol and allow to dry. As indicated in the text of the relevant chapter, this $TiCl_4$ treatment was done either once or three times consecutively.

Mesoporous TiO_2. On top of the blocking layer, mesoporous TiO_2 films (4 x 4 mm dimension) were screen-printed, layer by layer, to the desired thickness. A screen mesh

size of 180T was used, which yielded ~1 um thick films with each print of the purchased Dyesol TiO_2 pastes. Each layer dried by heating at 125 °C for 15 minutes on the hotplate. The total thickness of the mesoporous films for IV characterization was ~8 μm (comprising ~5 μm of 30 nm-sized TiO_2 particles ~3 μm of 150 –250 nm-sized TiO_2 particles). After the final TiO_2 layer was printed, the films were sintered according to the process shown in Table 1.

PEDOT counter electrode (CE). PEDOT counter electrodes were made via electropolymerization of an aqueous solution of EDOT onto 1 um thick mesoporous ITO films as follows. ITO films (7 x 7 mm dimension) were prepared by screen-printing an ITO paste onto pre-drilled FTO substrates using a screen with a mesh size of 180T, followed by heating at 450 °C for 30 minutes. Acting as the working electrode, the ITO films were immersed into the polymerization solution containing 0.01 M EDOT and 0.1 M SDS in MilliQ that was ultra-sonicated for at least 1 hour prior to its use. A bare FTO glass substrate was used as the counter electrode, and a silver wire used as the reference. A BioLogic in the galvanostatic (constant current) mode was used to apply a constant current of 100 μA per ITO electrode for 3 minutes (the electrode potential was about 0.7 V vs Ag/Ag^+). After electrodeposition, the electrodes were rinsed thoroughly in water, followed by washing in acetonitrile and the application of vacuum for 5 minutes.

Electrolyte filling and device assembly. The working and counter electrodes were fused together with a 25 μm hot-melt surlyn gasket, forming a compartment into which the MeCN-based electrolyte solutions containing the copper complexes were filled through a pre-drilled injecting hole via a back-filling technique and aid of vacuum. The electrolyte solutions (prepared and filled inside a glovebox) consisted of the Cu(II) (200 mM), Cu(I) (40 mM), LiTFSI (100 mM) and TBP (500 mM) in MeCN. Surlyn-coated aluminium foil heated to 120 °C was then used to seal the injecting hole by the application of pressure. Wires were soldered to each electrical contact for testing, both immediately and days after device fabrication.

2.4 Device Characterization

2.4.1 Photocurrent Density—Voltage (I–V)

The standard technique used to evaluate the performance of a solar cell is to measure their photocurrent—voltage (I–V) response under illumination that is calibrated to be 100 mW cm^{-2} = 1 Sun (AM1.5G). During such measurements, cells are irradiated from the light-absorbing material side, a potential is applied (either in forward bias, whereby electrons are injected from the photo-anode side, or in reverse bias, whereby electrons are injected from the counter-electrode side) and the output current measured. The typical I–V output is shown in Figure 28 (solid red curve) from which the important solar cell performance parameters are extracted—namely, the short circuit photocurrent (I_{SC}) the open circuit voltage (V_{OC}), the fill factor (FF), and the overall photon-to-electrical power conversion efficiency (η).

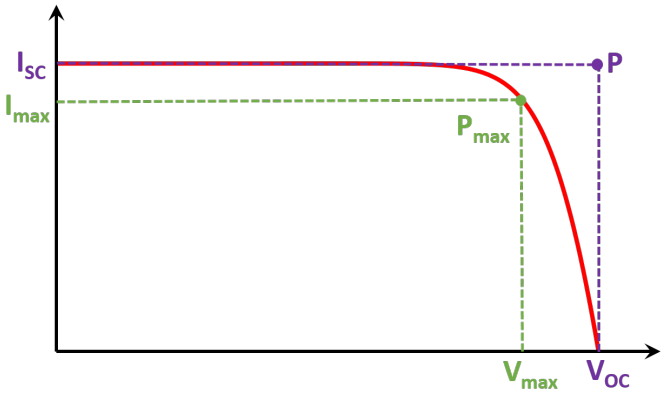

Figure 28. Typical I—V output from a solar cell.

Here, the I_{SC} corresponds to the current at 0 V and it is the maximum current the cell can produce. The V_{OC} corresponds to the maximum voltage the cell can provide to an external circuit. The theoretical maximum power output is P = I_{SC} V_{OC}. However, due to internal losses in the cell (i.e. series resistances and recombination losses), the most power output from the device is P_{max}. The FF is equal to P_{max}/P which is often used as a measure of the overall device quality i.e. the higher the FF, the closer the P_{max} is to the theoretical maximum, P.

The overall photon to power conversion efficiency is given by:

$$\eta = \frac{P_{max}}{P_{in}} = \frac{I_{SC}V_{OC}FF}{P_{in}} \quad \text{Eq. 3}$$

Experimental Set-up. I–V characterization was tested using a Photo Emission Tech. model SS50AAA solar simulator with the current-voltage curves measured by a Keithley 2400 source meter. The simulated sunlight (AM1.5G) was provided by an Oriel sun simulator using a filtered 1000 W xenon lamp. The output light was calibrated using a silicon photodiode provided by Peccell Technologies that was fitted with a colour filter to minimize the optical mismatch between the calibration diode and the DSCs.

Steady state current (specific to section 4.3.5) Steady state current characterization was performed using the same solar simulator employed for the current-voltage characterization. The device was connected to a BioLogic VSP potentiostat to record the current at a fixed voltage taken from the maximum power point of the I–V curve over time every 0.1 s.

Long-term stability (specific to section 4.3.5). Long-term stability measurements were conducted inside a Vötsch Atlas SC3 340 environmental chamber equipped with a solar simulator. The chamber temperature was maintained at 25 °C (actual cell temperature was higher due to continuous irradiation) and the relative humidity inside the chamber was 20%. Solar cells were kept under constant AM1.5G illumination for 120 h under open circuit condition. I–V curves for each cell were measured every 10 minutes. Light intensity fluctuations were monitored through the measurement of a reference Si solar cell and the maximum intensity variation during the experiment was within ±2.5% of the nominal value.

2.4.2 Incident Photon to Current Efficiency (IPCE)

Another standard measurement of solar cells is the incident photon to current efficiency (IPCE) which gives a measure of how efficiently the incident photons of specific wavelengths are being converted into photocurrent. This time, solar cells are exposed to

monochromatic light of known photon flux, $\Phi(\lambda)$, from which the IPCE spectrum is acquired by recording the photocurrent output at each spectral wavelength. The IPCE value at each wavelength depends on the efficiency at which the incident photons are being absorbed and converted into electrons, as given by

$$\mathrm{IPCE} = \mathrm{LHE}\varphi_{\mathrm{inj}}\varphi_{\mathrm{reg}}\varphi_{\mathrm{cc}} \qquad \text{Eq. 4}$$

where LHE is the harvesting efficiency of the light absorber, φ_{inj} is the injection efficiency, φ_{reg} is the regeneration efficiency and φ_{cc} is the charge collection efficiency. The integrated IPCE is equivalent to the I_{SC} derived from the I-V measurement under the same light conditions, i.e.

$$I_{SC} = e\int_{\lambda} \mathrm{IPCE}(\lambda)\Phi(\lambda)d\lambda \qquad \text{Eq. 5}$$

Experimental set-up. IPCE were measured as a function of wavelength by dispersing light from a tungsten filament (Newport 250 W QTH) through a monochromator (Oriel Cornerstone 130) with a 3.5 mm^2 spot. Light intensities of less than 1 mW cm^{-2} were used with short-circuit current recorded using a Keithley 2635 source measure unit. The system was calibrated by placing a calibrated photodiode (Thorlabs FDS-100CAL) in the device under test position and referencing the intensity measured to that of another silicon photodiode that samples a portion of the beam via a beam splitter and serves to account for any intensity fluctuations.

2.4.3 Open-Circuit Voltage Decay (OCVD)

OCVD is a simple technique that is often used to probe the kinetics of recombination by monitoring the transient of the V_{OC} of a device during the relaxation from illumination quasiequilibrium to dark equilibrium. The starting point for the V_{OC} decay measurement is the steady state of a cell illuminated at constant intensity. The illumination source is then switched off, and the V_{OC} of the cell is kept at open circuit is recorded over time with. The apparent electron lifetime is then given by:

$$\tau_e = -\frac{k_B T}{e}\left(\frac{dV_{OC}}{dt}\right)^{-1} \qquad \text{Eq. 6}$$

Experimental Set-Up. OCVD measurements were performed on full devices using a AM1.5G illumination source and the voltage output recorded with a BioLogic VSP potentiostat. Devices were illuminated until a steady state was reached, after which the light was switched off and the voltage transient recorded.

2.4.4 Electrochemical Impedance Spectroscopy (EIS)

Electrochemical impedance spectroscopy (EIS) is a technique widely used to resolve the electron transfer processes occurring in the operation of a solar cell—namely, the charge transfer resistance at the counter electrode, the recombination resistance at the TiO_2/CTM interface, and the resistance of the CTM. EIS works by measuring the current response of the device, I(ω,t), to an applied voltage perturbation, V(ω,t), from which the impedance, Z(ω), as a function of the perturbation frequency can be calculated by;

$$Z(\omega)=\frac{I(\omega,t)}{V(\omega,t)} \qquad \text{Eq. 7}$$

In this thesis, EIS was performed using a Zahner Zennium Electrochemical Work Station ECW IM6 as a frequency response analyser. The resulting impedance spectra (Nyquist plots) were then fitted to an equivalent circuit model using the ZView software, from which R_S (the series resistance), R_{CE} (the charge transfer resistance at the counter electrode), R_{rec} (the charge transfer resistance for electron recombination) and, R_{CTM} (resistance of the CTM, such as diffusion resistance of the redox species in solution) were then extracted. The equivalent circuits used to interpret the spectra were chosen carefully to accurately represent the physical processes occurring within the device at each potential. For DSCs in particular, electron injection from an excited dye molecule to TiO_2 is extremely fast, orders of magnitude higher than the electron diffusion trough the TiO_2 particles due to the exponential density of trap states that slows down electron transport[20]. Therefore, the recombination resistances extracted from EIS measurements of full devices is assumed to be occurring between injected electrons in the TiO_2 with the

redox species in solution. Any recombination between the excited dye molecule to the redox species is assumed to be negligible not accounted for in the impedance.

Experimental set-up and fitting for DSCs (specific to section 5.3.6.3). A 10 mV applied perturbation in the 1 Hz to 1 MHz frequency range at voltage potentials between 0.3 and 1.2 V of full devices were performed when illuminated with an LED white light source calibrated to reach 1 Sun. Nyquist plots were fitted to the model shown in Figure 29 at high voltages where the three arcs were visible; R1 = R_S, R2 = R_{CE}, R3 = R_{rec} and W_S = R_{diff}. For lower voltages, W_S was not obvious and removed from the fitting[215].

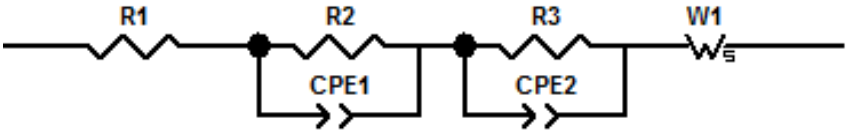

Figure 29. Equivalent circuit model for DSC.

Experimental set-up and fitting for PSCs (specific to section 4.3.5). Measurements were performed under illumination (27 mW cm^{-2}) with an applied potential of 700 mV for the device with spiro-OMeTAD and of 400 mV for the device with $[Fe(bpyPY4)](OTf)_{2.5}$, in the frequency range 1 Hz – 4 MHz. R_{rec} was calculated by fitting the semicircle in the middle frequency range ($50 < Z_{Re} < 1200$ Ω for spiro-OMeTAD and $15 < Z_{Re} < 400$ Ω for $[Fe(bpyPY4)](OTf)_{2.5}$) to the simplified version of the equivalent circuit introduced by Pascoe et al.[216] (R_S – series resistance; C_{con} - constant phase shift element used to simulate capacitive behavior at the interface). R_{rec} does not contribute to the low frequency range, which facilitated analysis of the data.

Chapter 3:

Cobalt Polypyridyl Complexes as Transparent Solution-Processable Solid-State Charge Transport Materials

The following chapter investigates the use of a novel cobalt hexadentate complex as a solution processible HTM in a solid-state dye-sensitized solar cell that uses the Y123 organic sensitizer. The work presented here is based on an article published Advanced Energy Materials[217]*, exposing the exceptional potential of transition metal complexes as solution-processable electronic charge transport materials, an area that has remained largely unexplored.*

Cobalt Polypyridyl Complexes as Transparent Solution-Processable Solid-State Charge Transport Materials.

Chapter contents

3.1 Introduction

Lowering the Inner-Sphere Activation Energy and Improving Stability of Cobalt Complexes using Ligands of High Denticity.

To date, the best performing 1-electron systems for DSC applications rely on Co(II/III) complex systems, with most based upon the polypyridyl ligands such as bipyridine (bpy), terpyridine (terpy), phenanthroline (phen). Their tuneable redox potential, low absorption cross-section and non-corrosiveness towards metal contacts make them ideal candidates for their use as CTMs in solar cells. They are, however, known to suffer mainly in terms of their relatively high inner reorganization energies (ΔG_{inner}) that presents a large barrier for intermolecular charge transfer (see section 1.5) that is reflected in their relatively large self-exchange rate of ($\sim$10 M^{-1} s^{-1})[218] . This can be largely attributed to the large changes in the Co–Ligand bond lengths during charge transfer between the high-spin d^7 and low-spin d^6 states of the Co(II) and Co(III) centers[117,219], that is estimated by:

$$\Delta G_{inner} = \frac{n}{2}\frac{f_{III}f_{II}}{f_{III}+f_{II}}\Delta X^2 \qquad \text{Eq. 8}$$

where f_i are the force constants for the Co(II) and Co(III)-ligand bonds and ΔX is the change in bond distances of n bonds[220]. Minimization of changes to the Co–Ligand bond lengths is therefore key to improving their intermolecular charge transfer properties, both interfacial and bulk (through self-exchange reactions).

Previous studies have successfully been able to reduce the Co–Ligand bond distances of cobalt complexes by the employment of high denticity ligands, namely, (2,6- bis(1,1-bis(2-pyridyl)ethyl)pyridine)cobalt(II/III) ($[Co(PY5Me_2)]^{2+/3+}$) and (6,6′-bis(1,1-di(pyridin-2-yl)ethyl)-2,2′-bipyridine)cobalt(II/III) ($[Co(bpyPY4)]^{2+/3+}$). Moreover, they were shown to exhibit better stability as a result of the enhanced rigidity of the ligand sphere and chelate effect[100]—also seen when comparing cobalt complexes of tridentate ligands to bidentate ligands[221]—an important consideration for the implementation of new materials in solar cells. Due to the rigidity of the reorganized cavity adopted by the high denticity ligands, the

complexes were found to endure very restricted structural change upon reorganization—with only minor changes to the equatorial Co–N bond lengths between Co(III) to Co(II) states—much smaller in comparison to the archetypal bidentate low-denticity cobalt complex, tris-(2,2'-bipyridine)cobalt(II/III) ($[Co(bpy)_3]^{2+/3+}$). From single crystal data analysis, the average change in bond lengths were calculated to be ΔX = 0.15 Å for $[Co(PY5Me_2)]^{2+/3+}$ and an even lower value of ΔX = 0.10 Å for $[Co(bpyPY4)]^{2+/3+}$, both considerably smaller than that of the archetypical cobalt complex $[Co(bpy)_3]^{2+/3+}$ (ΔX = 0.20 Å), which—according to Eq. 8—translates to inner-sphere reorganizational energies that are >50% smaller [115,121]. When tested as redox mediators in DSCs, both $[Co(PY5Me_2)]^{2+/3+}$ and $[Co(bpyPY4)]^{2+/3+}$ redox mediators were found to outperform $[Co(bpy)_3]^{2+/3+}$ in terms of both conversion efficiency and thermodynamic stability, showcasing the benefits associated with the use of high denticity ligands for solar cell applications.

3.2 Motivation and Strategy

The general features of high denticity metal complexes highlighted above make them ideal candidates for investigation as efficient metal complex-based HTM for solar cells, and for which are expected to have greater potential than low-denticity metal complexes in regard to stability and charge transfer ability (interfacial and bulk). Of those mentioned previously, the high denticity hexadentate cobalt complex, $[Co(bpyPY4)]^{2+/3+}$ was shown to attain a small estimated reorganization energy[48] This provided the main motivation in which to employ $[Co(bpyPY4)]^{2+/3+}$ as a solid-state HTM. The strategy used here was to find the optimum blend of $[Co(bpyPY4)]^{2+}$ and $[Co(bpyPY4)]^{3+}$ that allows for an efficient hole-hopping charge transfer mechanism between the Co(II) and Co(III) centers, and to compare it to the traditionally employed $[Co(bpy)_3]^{2+/3+}$ complex.

3.3 Results and Discussion

3.3.1 Synthesis and General Characterization

Synthesis of Co(bpyPY4). The $[Co(bpyPY4)](OTf)_2$ and $[Co(bpyPY4)](OTf)_3$ complexes were synthesized following established procedures[48] and shown in Figure 30. Briefly, the metal trifluoromethanesulfonate (OTf) salt of Co(II) was used for complexation with the bpyPY4 ligand in MeCN (scheme 1). The resulting complex, $[Co(bpyPY4)](OTf)_2$, was recrystallised twice by slow diffusion of diethyl ether (Et_2O) inside the MeCN solution, yielding dark red crystals. Due to the unavailability of Co(III)OTf salts, $[Co(bpyPY4)](OTf)_3$ was obtained by the oxidation of $[Co(bpyPY4)](OTf)_2$ with silver trifluoromethanesulfonate (AgOTF) in MeCN solution (scheme 2) which was also recrystallised twice by slow diffusion of Et_2O yielding yellow-orange crystals. Alternatively, the nitrosonium tetrafluoroborate ($NOBF_4$) oxidant was used for oxidation, resulting with the $[Co(bpyPY4)](OTf)_2(BF_4)$ complex (scheme 3).

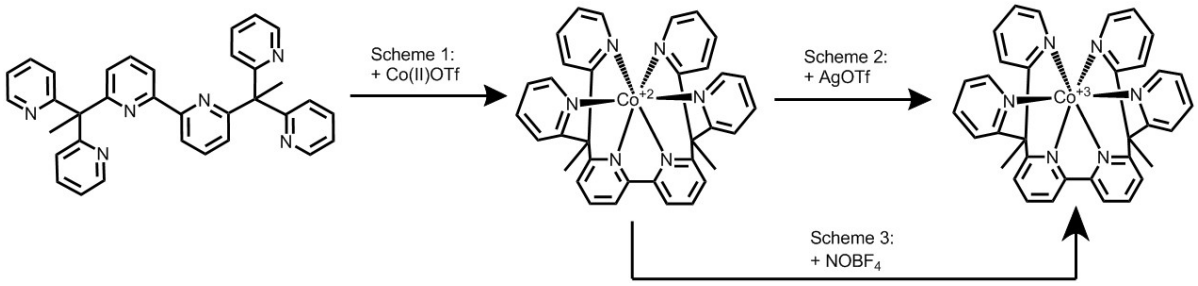

Figure 30. Synthetic scheme for $[Co(bpyPY4)](OTf)_2$ (scheme 1), $[Co(bpyPY4)](OTf)_3$ (scheme 2) and $[Co(bpyPY4)](OTf)_2(BF_4)$ (scheme 3).

Solubility. The use of the OTf^- counter-ions was used to ensure its solubility in organic solvents such as MeCN that are commonly used in the solution processing techniques for the fabrication of DSC devices. The synthesized complexes, including the Co(III) complex containing the BF_4 counter-ion, were found to exhibit excellent solubility in MeCN for the concentrations used in the subsequent studies, of which the highest concentrations used were 200 mM Co(II) and 100 mM Co(III) in the fabrication of solar cells.

Energy level. To determine the HOMO level, cyclic voltammetry was performed on 5mM $[Co(bpyPY4)](OTf)_2$ solutions in MeCN containing 0.1 M *n*-Bu_4PF_6 as a supporting

electrolyte. The cyclic voltammogram shows one-electron oxidation and reduction peaks from which a HOMO level (onset of the first oxidation peak) of -176 mV vs. Fc/Fc^+ (465 V vs. NHE) for $[Co(bpyPY4)]^{2+/3+}$ was obtained, Figure 31.

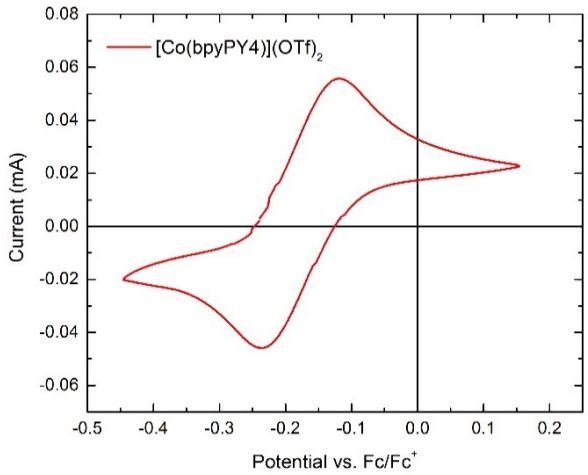

Figure 31. Cyclic voltammogram of $[Co(bpyPY4)](OTf)_2$ measured at a scan rate of 100 mV s^{-1} on 3 mM solutions with 0.1 M $TBAPF_6$ as a supporting electrolyte under nitrogen.

3.3.2 Thin Film Conductivity

The conductivity, σ, is directly proportional to the product of charge mobility, μ, and number density, n, of its charge carriers. For molecular-based conductors, the latter is dependent upon the ratio of oxidized and reduced species. As such, films comprising of various mixtures of $[Co(bpyPY4)](OTf)_2$ and $[Co(bpyPY4)](OTf)_3$, were investigated to determine the optimal composition. Herein, we define mixed films as $[M(L)](Y)_{2+x}$, where M is the metal center, L is the ligand, Y is the counter-ion, and the variable x is given by

$$x = \frac{[M(L)]^{n+1}]}{[M(L)]^{n} + [M(L)]^{n+1}]} \qquad \text{Eq. 9}$$

where n is oxidation number of the reduced species (1, 2, 3, etc.). Hence, $[Co(bpyPY4)](OTf)_{2.33}$ (M = Co, L = bpyPY4, T = OTf and x = 0.33) is a blend composed of $[Co(bpyPY4)](OTf)_2$ and $[Co(bpyPY4)](OTf)_3$ with a 2:1 molar ratio.

Conductivity measurement set-up. To characterize the conductivity, films were deposited onto interdigitated gold electrode arrays (IDAs). See section 2.2.4.2 for full specifications of the IDAs, techniques used for film deposition and the conductivity calculation. Briefly, HTM precursor solutions were prepared by dissolving $[Co(bpyPY4)](OTf)_2$ and $[Co(bpyPY4)](OTf)_3$ in acetonitrile with various compositions (Co^{2+} to Co^{3+}). Films were then deposited by drop-casting the MeCN-based precursor solutions onto the IDA gold electrodes and then measured by means of a 2-probe connection. Devices were kept under inert conditions during fabrication and testing to ensure stability of the films.

Room temperature conductivity. First, the room temperature conductivity of the various film compositions were measured as shown in Figure 32a. Here, pure $[Co(bpyPY4)](OTf)_2$ films showed a very low conductivity of 1.1×10^{-8} S m^{-1} while the addition of $[Co(bpyPY4)](OTf)_3$ reached a maximum conductivity of 3.0 S m^{-1} for x = 0.33, that is, eight orders of magnitude higher. Further increases to the $[Co(bpyPY4)](OTf)_3$ concentration (x > 0.33) caused the conductivity to drop down, which can be attributed to a combination of reduced hole mobility and well as poorer film morphology due to the inherent crystallization of $[Co(bpyPY4)](OTf)_3$.The room- temperature conductivity of a spiro-OMeTAD film with a typical molecular doping level of 10% was also measured under the same conditions, reaching a conductivity value of 4.8×10^{-5} S m^{-1}, demonstrating that films of $[Co(bpyPY4)](OTf)_{2.33}$ possess exceptional conductivity. The linear current-voltage characteristics of the pristine and optimized composition as shown in Figure 32b are indicative of the good ohmic contacts established between the solid films and the gold electrodes.

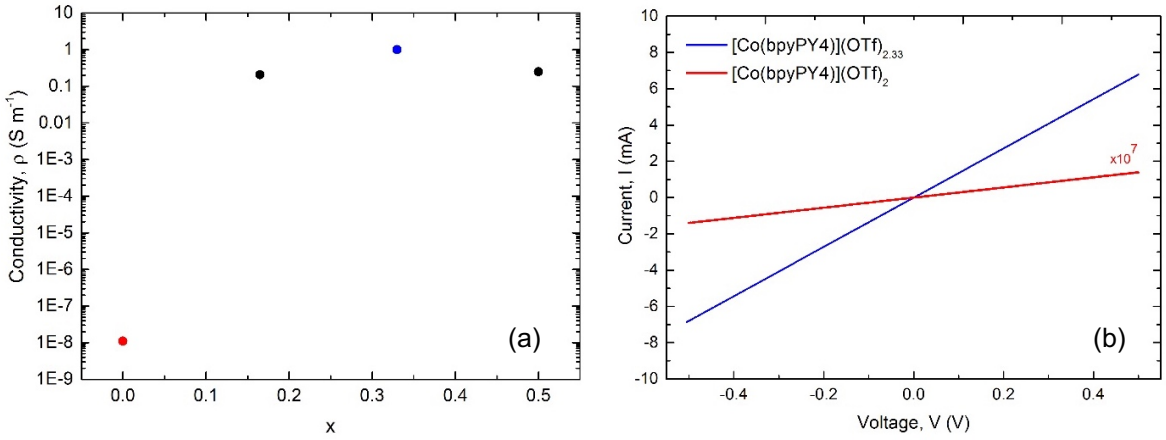

Figure 32. (a) Room-temperature conductivity of thin films composed of various blends of $[Co(bpyPY4)](OTf)_2$ and $[Co(bpyPY4)](OTf)_3$, and **(b)** Room temperature I–V curves of pristine $[Co(bpyPY4)](OTf)_2$ (red) and the optimized composition, $[Co(bpyPY4)](OTf)_{2.33}$ (blue), both showing ideal ohmic behaviour.

Variable temperature conductivity. In order to gain a mechanistic understanding of the charge transport mechanism responsible for the high conductivity of the mixed $[Co(bpyPY4)](OTf)_{2.33}$ films, temperature-dependent conductivity measurements were performed. The resistivity versus temperature ρ(T) plot surprisingly shows an almost linear decrease in resistivity upon cooling from 300 to 30 K, before it begins to level off at about 20 K (Figure 33a), and found to be more than twice as conductive at 4.5 K (7.4 S m^{-1}) than they are at room temperature (3.0 S m^{-1}). Similar temperature-dependent conductivity behaviour was observed for $[Co(bpyPY4)](OTf)_2(BF_4)_{0.33}$ films fabricated from $[Co(bpyPY4)](OTf)_2$ solutions partially oxidized with $NOBF_4$, suggesting that the combination of the $[Co(bpyPY4)]^{2+}$ and $[Co(bpyPY4)]^{3+}$ cations is responsible for both the improved conductivity and the temperature dependence of conductivity. On the other hand, pristine $[Co(bpyPY4)](OTf)_2$ and doped spiro-OMeTAD films display exponential increases in their resistivity upon cooling, Figure 33b. Such exponential behaviour is typical for semi-conducting materials whereby thermally activated hopping is the dominant mode of charge transport.

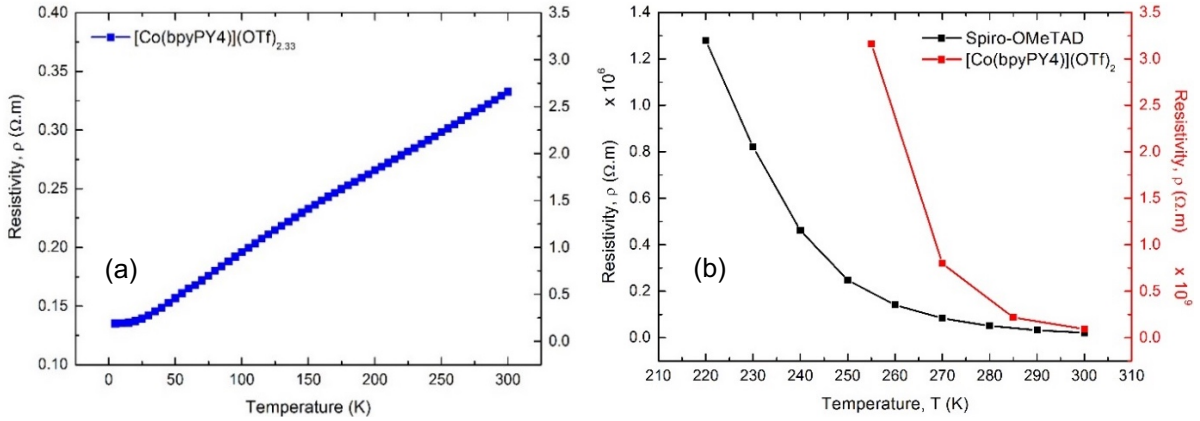

Figure 33. Resistivity curves upon cooling for **(a)** $[Co(bpyPY4)](OTf)_{2.33}$ (blue) and **(b)** $[Co(bpyPY4)](OTf)_2$ (red) and spiro-OMeTAD (black) thin films, drop-casted onto IDA electrodes.

Arrhenius behaviour. Temperature-dependent conductivity of CTMs in which thermally activated charge hopping between molecular species is the dominant charge transport mechanism can generally be described by the Arrhenius equation. For such CTMs, the classical Arrhenius plot of ln(σ) versus 1/T is linear with a negative slope that depends on the activation energy of the charge hopping process. However, the plot shown in Figure 34a clearly illustrates that non-Arrhenius-type transport is dominant for $[Co(bpyPY4)](OTf)_{2.33}$ films throughout the 4.5–300 K temperature range. Instead, it shows a behaviour typically observed for metallic conductors and highly doped degenerate semiconductors showing band-like transport[222,223] where the resistivity is dominated by acoustic phonon scattering. In contrast, pure $[Co(bpyPY4)](OTf)_2$ films, which have only the Co(II) complex present, follow the classical temperature dependence expected for thermally activated charge transport systems and displays a linear Arrhenius plot, a trend that was also found for doped films of the archetypal hopping-transport material spiro-OMeTAD, Figure 34b.

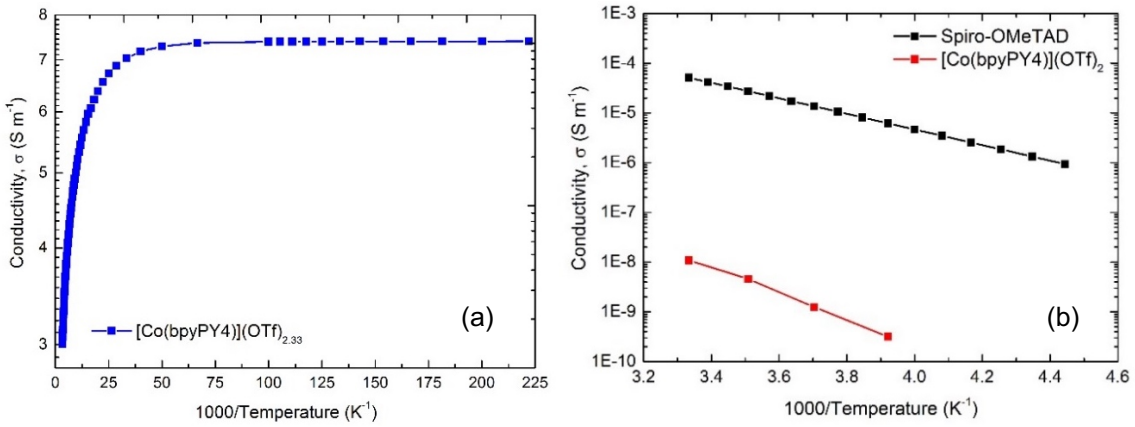

Figure 34. Arrhenius plots of **(a)** [Co (bpyPY4)](OTf)$_{2.33}$ (blue) and **(b)** [Co (bpyPY4)](OTf)$_2$ (red) and doped spiro-OMeTAD (black) thin films, drop-casted onto IDA electrodes.

A similar behaviour has been reported for thin films of poly(3,4-ethylenedioxythiophene) (PEDOT), in which undoped films display thermally activated charge transport, while partially oxidized films whose charge is balanced by tosylate anions (PEDOT:Tos) exhibit negative temperature coefficients[223]. Interestingly, partially oxidized PEDOT films containing the polyelectrolyte polystyrene sulfonate (PEDOT:PSS) displayed thermally activated hopping transport even in the doped state. The differing temperature-dependent conductivities of the two partially oxidized PEDOT materials were attributed to the higher degree of crystallinity in PEDOT:Tos compared to the amorphous PEDOT:PSS films. The CTM studied here is fundamentally different from PEDOT:Tos, because the underlying charge transport phenomena in conducting polymers, such as polaron and bipolaron displacement, cannot occur in [Co(bpyPY4)](OTf)$_{2.33}$ films. The optical appearance of [Co(bpyPY4)](OTf)$_{2.33}$ films also indicates that this CTM is a glass-forming, rather than a crystalline, material.

3.3.3 Thin Film Morphology

X-ray diffraction spectra. To investigate the nanoscale morphology of [Co(bpyPY4)](OTf)$_{2.33}$ films, grazing-angle incident x-ray diffraction (GAXRD) analysis was used, Figure 35. For these measurements, films were spin-coated onto pre-cleaned silicon wafer substrates. Three very broad diffraction peaks are identified at 10.5°, 15.5° and 25.0° that are absent on the GAXRD diffractogram of the silicon substrate. The

broadness of the peaks suggests the films to be mostly amorphous as was suspected, with some indication of short-range order in the nanometer range. Attempts to simulate the $[Co(bpyPY4)](OTf)_{2.33}$ thin film GAXRD diffractogram based on the available $[Co(bpyPY4)](OTf)_2$ single-crystal diffraction data coupled with peak broadening according to the Scherrer equation did not yield solutions with adequate fits.

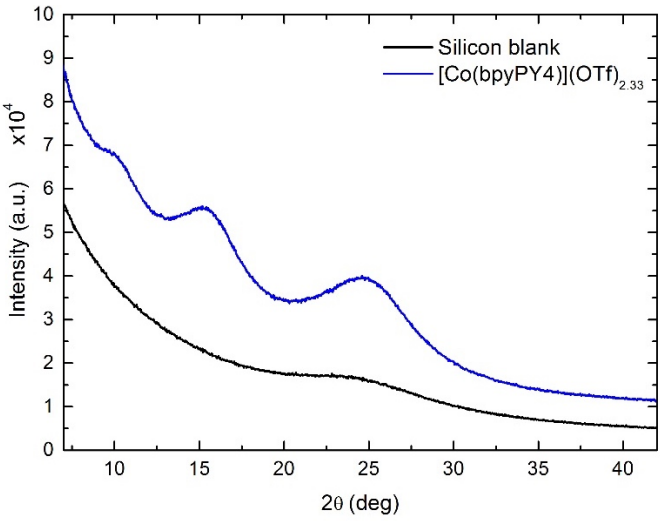

Figure 35. GAXRD of a 1.3 μm thick $[Co(bpyPY4)](OTf)_{2.33}$ film (blue) spin-coated on a single crystalline Si substrate. The diffractogram of the uncoated single crystalline Si substrate (black) is shown for comparison.

Electron microscopy. To gain further understanding of the nanoscale morphology, high-resolution transmission electron micrographs (HRTEMs), Figure 36a, and selected area diffraction patterns (SAEDs), Figure 36b, were obtained. TEM specimens were of drop-casted films onto copper grids for analysis. The $[Co(bpyPY4)](OTf)_{2.33}$ films appear to be primarily amorphous as can be induced from the from the uniform contrast seen in the HRTEM and the diffuse rings obtained in the SAED pattern. This agrees well with the grazing angle GAXRD patterns obtained.

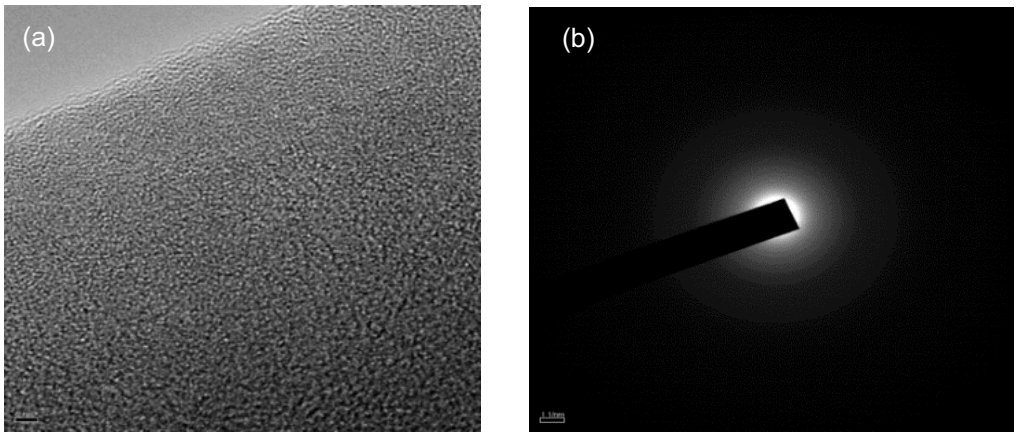

Figure 36. (a) HRTEM and **(b)** SAED pattern of a drop-casted $[Co(bpyPY4)](OTf)_{2.33}$ film.

3.3.4 Spin-Cross Over of Thin Films

Upon cooling, Co(II) polypyridyl complexes have been reported to undergo a high-spin to low-spin transition[224]. In the presence of a trigonal prismatic ligand field, the Co^{2+} ion with a d^7 electron configuration can either adopt the low-spin state (S =1/2) or high-spin state (S =3/2). Magnetic susceptibility measurements were therefore performed to elucidate whether spin-crossover contributes to the unusual temperature-dependent conductivity behaviour in $[Co(bpyPY4)](OTf)_{2.33}$ films.

Magnetic susceptibility. Room-temperature magnetic susceptibility measurements $[Co(bpyPY4)](OTf)_3$, confirmed its expected diamagnetic low-spin state. Temperature-dependent magnetic susceptibility (χ MT) data for $[Co(bpyPY4)](OTf)_{2.33}$ films indeed revealed that χMT continuously decreases from 350 to 100 K and levels off below 100 K (Figure 37a), consistent with a high-spin to low-spin transition of the Co^{2+} ions in $[Co(bpyPY4)](OTf)_{2.33}$. Importantly, the levelling of χMT at T ≤ 100 K and the solid-state structure of $[Co(bpyPY4)](OTf)_2$ both indicate that spin-crossover transition is complete at 100 K, which precludes spin-crossover as an explanation of the low-temperature conductivity behaviour from 100 to 10 K. The decrease in magnetic susceptibility observed for $[Co(bpyPY4)](OTf)_{2.33}$ upon cooling from 360 to 4 K closely matches the magnetic susceptibility changes that were observed for pure $[Co(bpyPY4)](OTf)_2$ (Figure

37b), yet the observed temperature dependence of conductivity is fundamentally different for these materials.

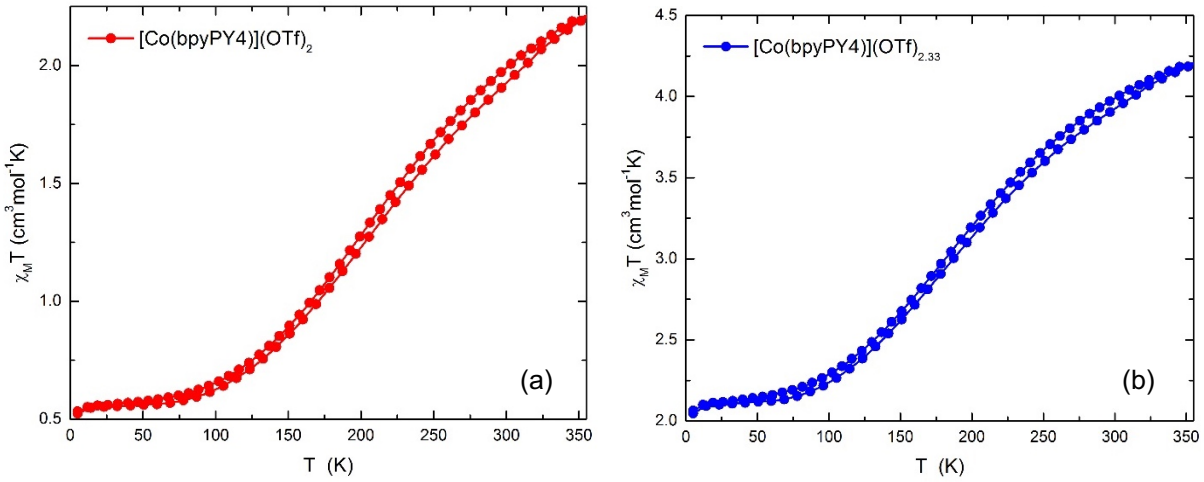

Figure 37. Variable temperature magnetic susceptibility of **(a)** Co(bpyPY4)](OTf)$_2$ and **(b)** Co(bpyPY4)](OTf)$_{2.33}$ measured at 1000 Oe.

3.3.5 Computational Study of the Electronic Structure

To investigate whether differences in the electronic structure of $[Co(bpyPY4)]^{2+/3+}$ and $[Co(bpy)_3]^{2+/3+}$ can account for their distinctively different charge transport properties, Hybrid density functional theory (DFT) calculations using B3LYP/6-311G*/CPCM were performed. Here, geometry optimization was carried out considering a low spin doublet state, $^2[Co(bpyPY4)]^{2+/3+}$, a high spin quartet, $^4[Co(bpyPY4)]^{2+/3+}$, and a closed shell singlet state, $^1[Co(bpyPY4)]^{3+}$.

Spin state, HOMO and LUMO analysis. Calculations obtained were in agreement with the magnetic susceptibility measurements shown previously (section 3.3.4), with the quartet spin state $^4[Co(bpyPY4)]^{2+/3+}$ in favour by 0.16 eV over the $^2[Co(bpyPY4)]^{2+/3+}$ doublet state at room temperature. Likewise, a quartet spin state was observed for the archetypical cobalt complex $[Co(bpy)_3]^{2+/3+}$ at room temperature[225] but with a larger quartet/doublet splitting of 0.21 eV. As depicted in Figure x, the HOMO of the singlet $^1[Co(bpyPY4)]^{3+}$ complex is ligand-based—mainly localized on the bipyridyl unit of the bpyPY4 ligand, with little admixture of metal character—while the LUMO and LUMO+1

are combinations of metal e_g (d_{x2-y2} and d_{z2}) states with ligand states. The frontier orbitals of the $^{2/4}$[Co(bpyPY4)]$^{2+}$ complexes are directly related to the HOMOs and LUMOs of ^{1}[Co(bpyPY4)]$^{3+}$. The one-electron reduction of ^{1}[Co(bpyPY4)]$^{3+}$ leads to ^{2}[Co(bpyPY4)]$^{2+}$ with its singly occupied orbital corresponding to what was the LUMO of ^{1}[Co(bpyPY4)]$^{3+}$. In ^{4}[Co(bpyPY4)]$^{2+}$ formally obtained by splitting two electrons from a doubly occupied orbital of the ^{2}Co(II) complex, two unpaired electrons are localized in molecular orbitals, corresponding to the LUMO and LUMO+1 of ^{1}[Co(bpyPY4)]$^{3+}$, while the lower-energy unpaired electron is partially delocalized across the ligand shell and the metal. This partial ligand character of the unpaired electrons is reflected in a total spin density on the metal of ≈2.7 e.

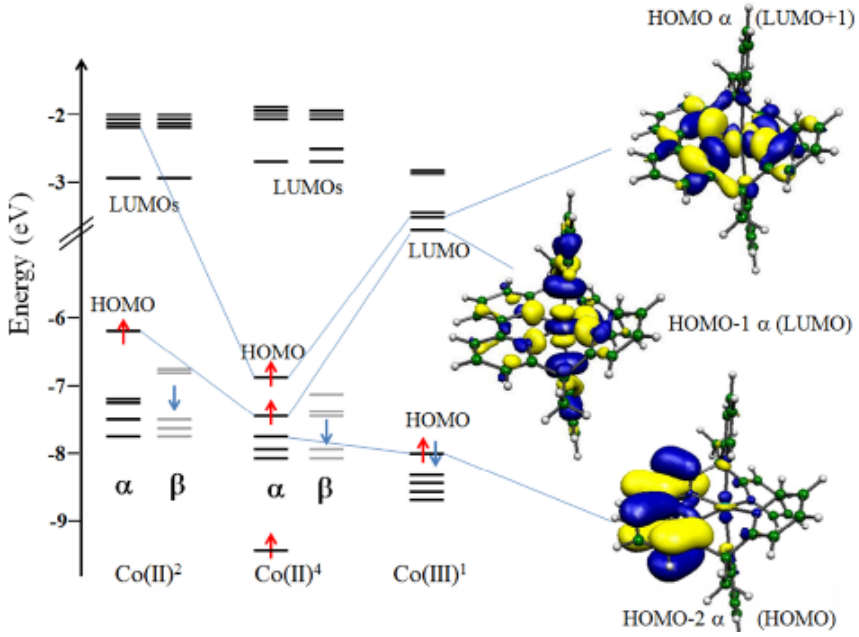

Figure 38. Energy splitting and frontier molecular orbitals of the [Co(bpyPY4)]$^{2+/3+}$ as calculated using B3LYP/6-311G*/CPCM.[226]

Whilst similar admixtures of metal and ligand characters and charge delocalization were found for the frontier orbitals of [Co(bpy)$_3$]$^{2+/3+}$, the stabilization of the doublet state in [Co(bpyPY4)]$^{2+}$ may facilitate electron transfer by partly avoiding a spin-crossing barrier between the low-spin Co(III) and high-spin Co(II) species.

3.3.6 Optical Studies of Solutions and Thin Films

Traditionally, metal complexes have been chosen for their superior light absorption and emission properties. Seminal examples include the thin copper phthalocyanine absorber layer used in C. W. Tang's archetypal two-layer organic solar cell[227], and highly luminescent iridium[228] and cobalt[229] complexes used in organic light emitting diodes (OLEDs). However, as highlighted in section 1.4, the successful application of new HTMs in solar cells often requires that the material itself does not absorb significant fractions of either generated or incident photons. In this regard, $[Co(bpyPY4)](OTf)_{2+x}$ films show exceptional optical properties.

Optical Absorption of solutions and films. Molar extinction coefficients, ε, for $[Co(bpyPY4)](OTf)_2$ and $[Co(bpyPY4)](OTf)_3$ solutions in acetonitrile below 200 M^{-1} cm^{-1} throughout the entire visible spectrum of 400-800 nm, Figure 39a. For a 1.0 μm-thick film, this translates to a transmission fraction of 83% or higher throughout the visible range, independent of the doping level. Metal-to-ligand charge transfer (MLCT) peaks are observed at 450 and 460 nm for both oxidative states—but with $[Co(bpyPY4)](OTf)_3$ lowered in its molar absorptivity extent—and an additional shoulder at 447 nm for $[Co(bpyPY4)](OTf)_2$ only.

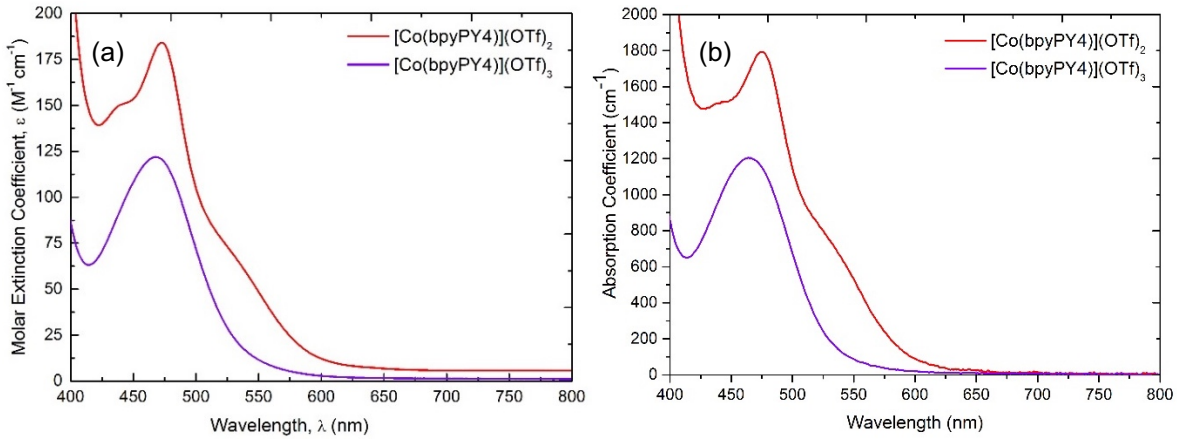

Figure 39. (a) Molar extinction coefficient spectra of thin films spin-coated on glass and **(b)** absorption coefficient spectra of MeCN-based solutions of $[Co(bpyPY4)](OTf)_2$ (red) & $[Co(bpyPY4)](OTf)_3$ (purple).

Electronic coupling. The absence of broadening or shifts in the solution UV–vis and diffuse reflectance spectra of $[Co(bpyPY4)](OTf)_{2.33}$ either in solution or the solid-state, relative to an idealized combination of the individual cobalt(II) and cobalt(III) complexes (calculated by: $A[Co(bpyPY4)](OTf)_{2.33} = 0.33[Co(bpyPY4)](OTf)_3 + (1 - 0.33)[Co(bpyPY4)](OTf)_2$) suggests a lack of electronic coupling between these ions (Figure 40).

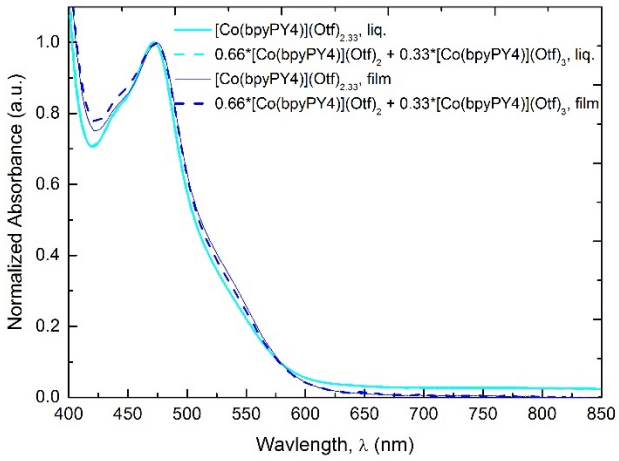

Figure 40. Normalized UV/Vis absorption spectra for solid-state films (dark blue) and MeCN liquid solutions (light blue) of $[Co(bpyPY4)](OTf)_{2.33}$, both experimental (solid lines) and calculated (dotted lines).

3.3.7 Application as HTM in ssDSC

Previous work has demonstrated $[Co(bpyPY4)](OTf)_2/[Co(bpyPY4)](OTf)_3$ to be a viable redox mediator for the fabrication of liquid-electrolyte DSCs with exceptional stability under full sun illumination and with impressive energy conversion efficiencies reaching 9.6% when used in conjunction with the classical organic sensitizer MK2.[48] Here, solid $[Co(bpyPY4)](OTf)_{2.33}$ films were employed in DSCs to demonstrate the applicability of this novel solid-state CTM in electronic devices, and were compared to that of $[Co(bpy)3](OTf)_{2.33}$ films. In this case, the Y123 organic dye sensitizer was used as the light absorber which has been used previously to achieve efficiencies beyond 10%, and with excellent device stability at high temperatures. As depicted from the energy level diagram of the Y123 dye and $[Co(bpyPY4)]^{2+3+}$, Figure 41b, a driving force of 610 mV for

dye regeneration / hole extraction is expected, a value larger than for $[Co(bpy)_3]^{2+3+}$ (500 mV).

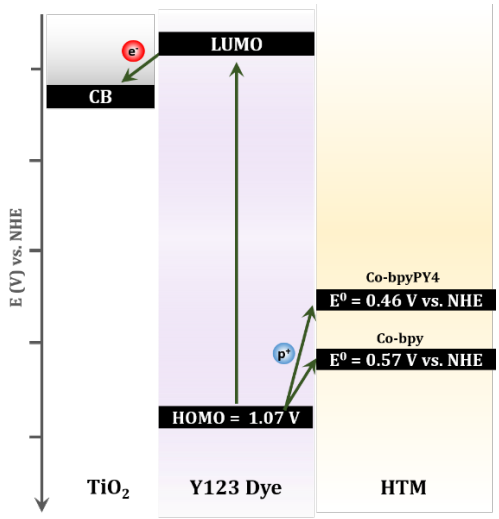

Figure 41. Energy level diagram for a $[Co(bpyPY4)]^{2+/3+}$ and $[Co(bpy)_3]^{2+/3}$ based ssDSC with the Y123 organic dye.

DSC fabrication. Sandwich-type ssDSCs were fabricated employing 10 µm thick TiO_2 photoanodes. Details of fabrication can be found in the experimental section 2.3.1. Briefly, liquid-based DSCs were built as normal. Prior to sealing the HTM precursor solution, vacuum was repeatedly applied to remove the MeCN solvent, followed by heating at 70 °C for a period of 4 h. The HTM precursor solution was prepared neat and with both Li(TFSI) and 4-(trifluoromethyl)pyridine (TFMP) as additives, chosen as they have been shown to significantly improve efficiencies in solid-electrolyte DSCs using spiro-OMeTAD[230].

DSC performance. In the presence of additives, an efficiency of 5.68 % was measured with a respectable short-circuit current density (J_{SC}) of 12.1 mA cm^{-2}, an open-circuit voltage (V_{OC}) of 768 mV, a fill factor of 62 % and an incident photon to current efficiency (IPCE) up to 70 % (Figure 42a-b). These values are higher than those measured for the additive-free HTM (which reached a maximum efficiency of 3.2 %), which can be attributed to the positive blocking effect that Li^+ cations and TBP molecules at the TiO_2 interface can have on the overall device performance. SsDSCs with $[Co(bpy)_3](OTf)_{2.33}$ (bpy = 2,2′-bipyridine) as the HTM reached much lower efficiencies of 0.02% in the

absence and 0.22% in the presence of additives, values that are consistent with the low conductivity (< 10^{-12} S m^{-1}) measured for solid $[Co(bpy)_3](OTf)_{2.33}$ films, and demonstrating that the exceptional performance of $[Co(bpyPY4)](OTf)_{2.33}$ films are not common to all cobalt polypyridyl complexes. Indeed, the 5.68 % efficiency for a solid-state cobalt complex HTM compares very favourably with the highest performance ever reported for a spiro-OMeTAD-based DSC of 7.7%, which is the result of continuous optimization of the initial reported efficiency of just 0.74% reported in 1998[10].

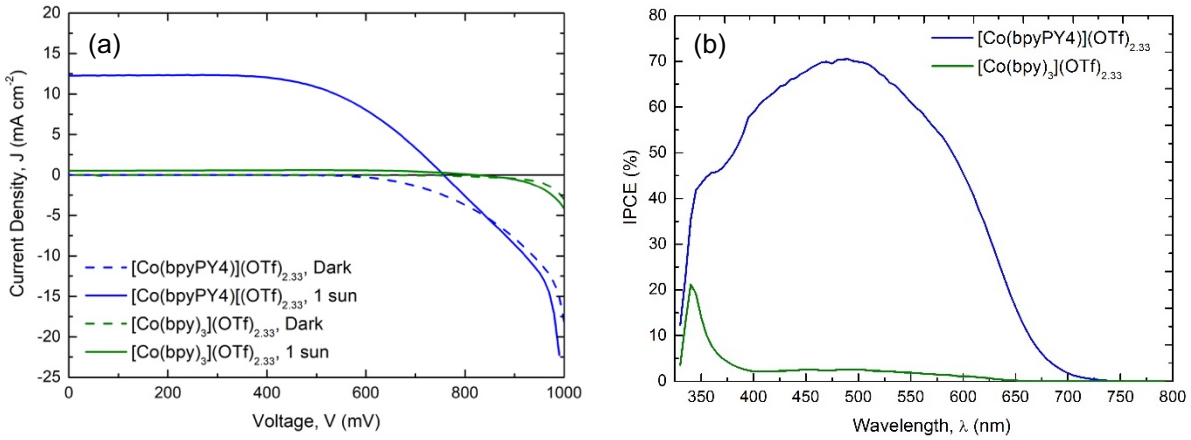

Figure 42. (a) J–V curves and **(b)** IPCE spectra measured for the best-performing Y123 ssDSCs based on the $[Co(bpyPY4)](OTf)_{2.33}$ (blue) and $[Co(bpy)_3](OTf)_{2.33}$ (green) HTMs, measured under standard AM1.5G irradiation (solid curves) and in the dark (dashed curves).

Table 2. Photovoltaic performance data for ssDSCs employing cobalt complexes as HTMs and the Y123 dye, measured under standard AM1.5G irradiation. The average performance with a standard deviation over four devices is provided.

HTM	V_{OC} [mV]	J_{SC} [mA cm^{-2}]	FF [%]	PCE [%]
$[Co(bpyPY4)](OTf)_{2.33}$	654 ± 2	7.07 ± 0.34	70 ± 1	3.23 ± 0.09
$[Co(bpyPY4)](OTf)_{2.33}$ with additives	768 ± 1	12.12 ± 0.26	62 ± 3	5.68 ± 0.06
$[Co(bpy)_3](OTf)_{2.33}$	694 ± 1	0.02 ± 0.01	77 ± 0.02	0.02 ± 0.01
$[Co(bpy)](OTf)_{2.333}$ with additives	877 ± 5	0.66 ± 0.20	73 ± 2	0.21 ± 0.05

Pore-filling ability. As highlighted previously, the pore filling of HTMs into the mesoporous TiO_2 scaffold has been identified as one of the key limitations to device performance[61,62]. Scanning electron microscopic (SEM) images of the cross-section of a device employing the $[Co(bpyPY4)](OTf)_{2.33}$ HTM, Figure 43, indicates good pore-filling

and interpenetration into the dye-sensitized TiO_2 film. This can be ascribed to their small molecular size and good solubility that allows for speedy infiltration when deposited from their precursor solution, enabling the use of a 10 μm thick film for a high short-circuit photocurrent of the device, which would be normally limited to less than 3 for the spiro-OMeTAD HTMs. Their amorphous phase upon solidification (see section 3.3.3) also ensures good contact to the sensitizer for a high proportion of the photocurrent to be collected. Dissolution and subsequent NMR spectroscopic analysis of the $[Co(bpyPY4)](OTf)_{2.33}$ solid-state matrix (with additives) showed the residual acetonitrile to be ≈ 8 mass%, an amount similar to the amount of solvent found in single crystals of $[Co(bpyPY4)](OTf)_3$ (11 mass%), indicating that the method used for solvent removal was sufficient.

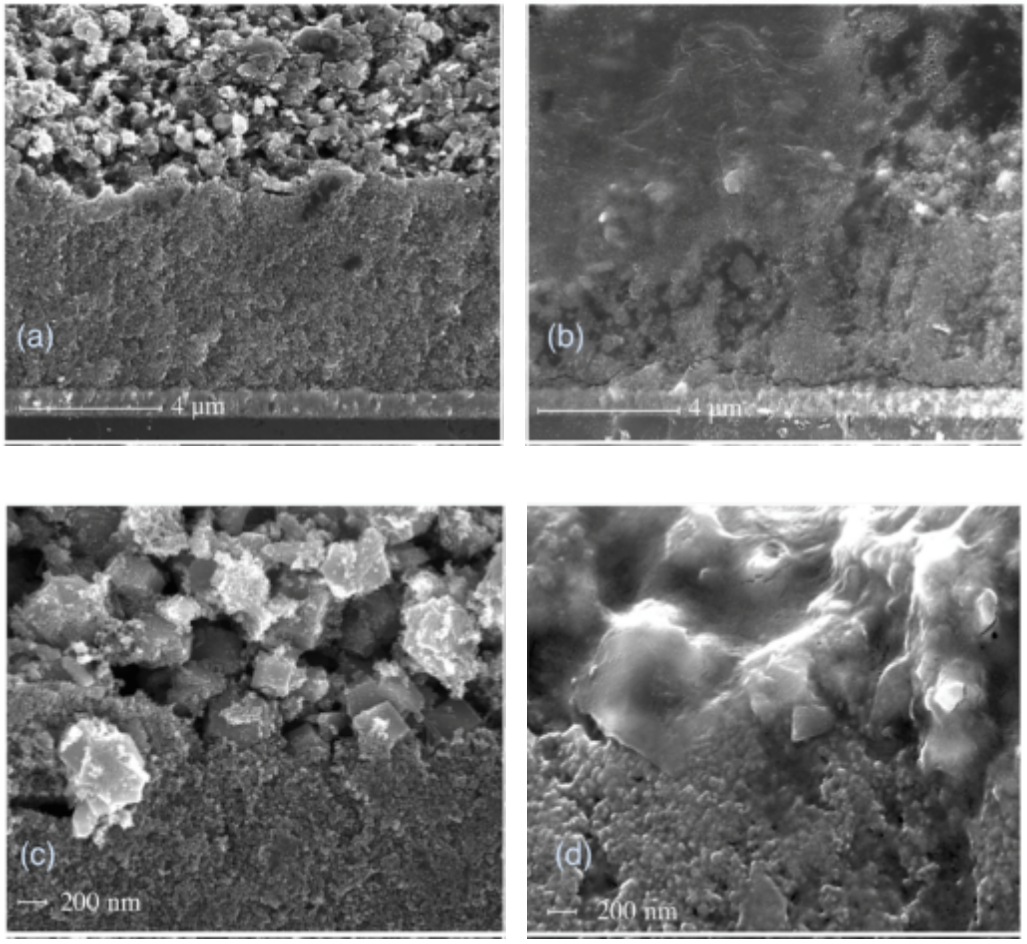

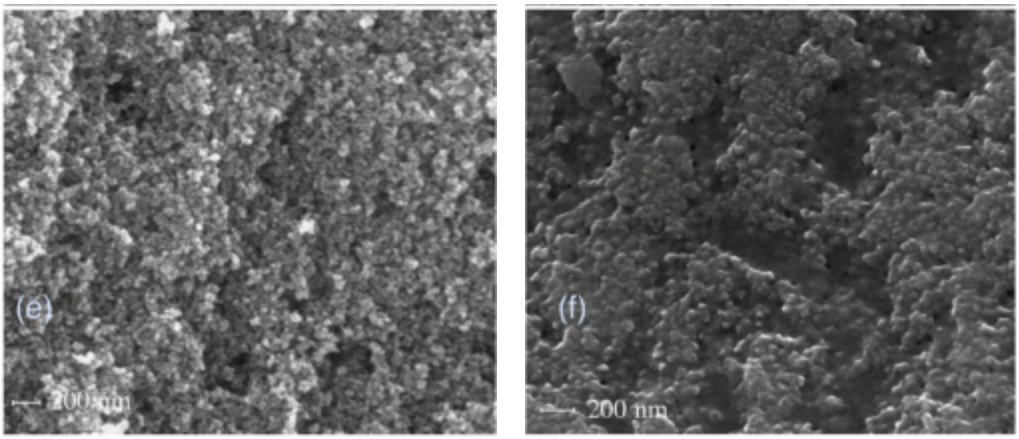

Figure 43. Cross-sectional SEM images of a complete DSCs showing the TiO_2 film solid-state solar cells **(a)**, **(c)**, **(e)** before and **(b)**, **(d)**, **(f)** after infiltration with the solid-state matrix of $[Co(bpyPY4)](OTf)_{2.33}$.

Electron lifetime. To determine the lifetime of photoinjected electrons in DSCs employing a $[Co(bpyPY4)]^{2+/3+}$ liquid electrolyte and $[Co(bpyPY4)](OTf)_{2.33}$ solid-state HTM, intensity-modulated photovoltage spectroscopy (IMVS), complemented by charge extraction experiments was used. Figure 44a reveals that the electron lifetime in the ssDSC is about 2.3 times shorter than for the liquid electrolyte Co-bpyPY4 DSCs, when the comparison is done at identical electron densities in the TiO_2 film. This can be explained in terms of the overall difference in the molar concentration of $[Co(bpyPY4)](OTf)_2$ in the liquid electrolyte (0.100 M) and solid-state CTM (0.55 M), the latter of which was estimated based on the densities of $[Co(bpyPY4)](OTf)_2$ and $[Co(bpyPY4)](OTf)_3$ derived from single-crystal XRD data. Additional IMPS experiments revealed no major difference in electron transit times between liquid electrolyte and solid-state $[Co(bpyPY4)](OTf)_{2.33}$ DSCs.

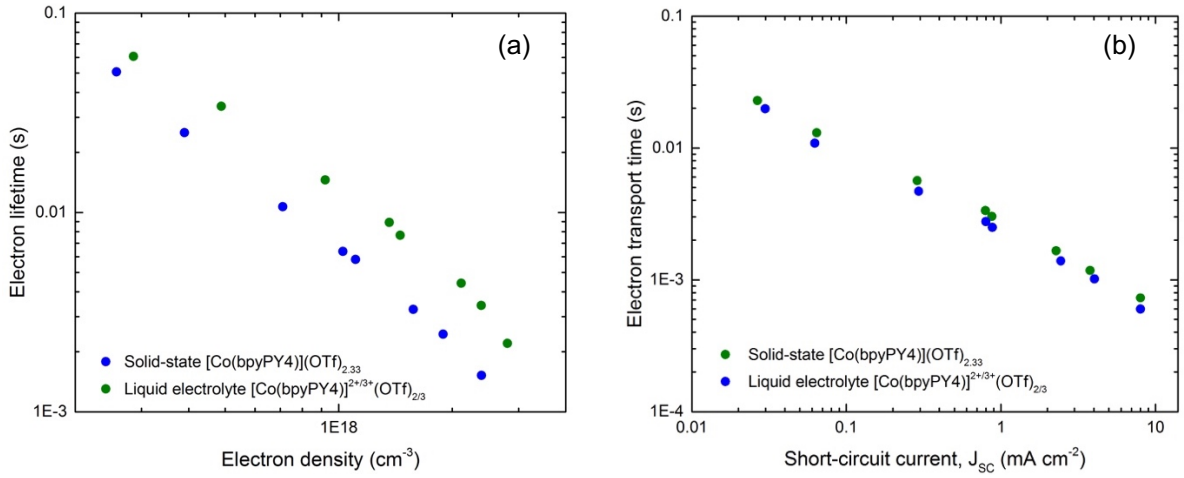

Figure 44. (a) Electron lifetime as a function of electron density in the TiO_2 electrode (obtained from IMVS complemented by charge extraction experiments, and **(b)** electron transport times as a function of J_{SC} as (obtained from charge IMPS measurements), for the solid-state $[Co(bpyPY4)](OTf)_{2.33}$ DSC (blue) shown in Figure 42 and for the liquid-electrolyte DSC with an identical electrolyte composition to the MeCN-based HTM precursor solution (green) containing 200 mM Co(II), 100 mM Co(III), 100 mM LiTFSI and 500 mM TBP.

3.4 Summary and Conclusions

In this chapter, a solid-state HTM based on a Co-bpyPY4 metal complex was investigated where bpyPY4 is a high denticity hexadentate ligand, a ligand that was chosen carefully such that high stability and charge transfer could be attained. The initial idea was that, by employing blends of $[Co(bpyPY4)](OTf)_2$ and $[Co(bpyPY4)](OTf)_3$, a hole-hopping conduction mechanism between Co(II) and Co(III) centers would take place. However, inferences from the electrical conductivity measurements suggested otherwise.

Room temperature conductivity measurements of pure drop-casted $[Co(bpyPY4)](OTf)_2$ films attained a low conductivity (1.1×10^{-8} S m^{-1}), whilst a blended mixture containing 33 % of the oxidized species attained a conductivity that was 8 orders of magnitude higher (3.0 S m^{-1}). A mechanistic understanding of the charge transport mechanism responsible for the high conductivity was acquired through temperature-dependent conductivity measurements. Here, pristine $[Co(bpyPY4)](OTf)_2$ films displayed a resistivity that increased exponentially upon lowering the temperature, a behaviour typical for semiconducting materials where thermally activated hopping that follows the Arrhenius equation is the dominant mode of charge transport. On the other hand, the mixed films displayed a negative temperature coefficient of conductivity ($d\sigma/dT$) and non-Arrhenius behaviour, having a solid-state conductivity of 3.0 S/m at room temperature and 7.4 S/m at 4.5 K. Surprisingly, the XRD and TEM studies show these mixed films to be largely amorphous. The novelty of Co(bpyPY4) is highlighted by the lack of strong $\pi - \pi$ interactions or high crystallinity that is characteristic of organic-inorganic hybrid materials that have negative temperature coefficients of conductivity. An understanding of the underlying mechanism of charge transport still lacks, however, and further studies to elucidate the unusual charge transport properties revealed in this work is required. When applied as a HTM in a ssDSC, impressive solar energy conversion efficiencies of 5.68% were achieved. Solid films of Co-bpy, a bypyridyl transition metal complex commonly used in DSCs, were also applied as a HTM but achieved a much lower efficiency of 0.22 % which was in good correlation with its significantly low conductivity, suggesting that the exceptional properties of Co-bpyPY4 films are not common to other archetypal cobalt polypyridyl complexes.

Chapter 4:

Polypyridyl Iron Complex as a Hole-Transporting Material for Formamidinium Lead Bromide Perovskite Solar Cells

The following chapter investigates the use of a novel iron hexadentate complex as an additive-free, solution-processable HTM in a perovskite solar cell that employs the formamidinium lead bromide absorber. The work presented here is based on an article published ACS Energy Letters[231]*, providing the first evidence of the applicability of a HTM in a PSC of a material in which the conductivity is a result of the redox transformation of a transition metal.*

Polypyridyl Iron Complex as a Hole-Transporting Material for Formamidinium Lead Bromide Perovskite Solar Cells.

Chapter Contents

4.1 Introduction

Cost-Efficient and Additive-Free HTMs for PSCs.

PSCs have shown unprecedented progress in their power conversion efficiencies—increasing from 3.8 to 22% in only a few years—making it the fastest-advancing solar technology on record. With the potential to be produced at low-cost, PSCs are now viewed as one of the most competitive solar cell technologies within the field. Several PSC architectures have been developed during its few years of existence, however, key to the best performing PSCs is the employment of a HTM. Here, the HTM plays the important role of efficiently extracting holes from the perovskite absorber, minimizing losses caused by recombination of photo-generated charges at the TiO_2/perovskite/HTM interface.

To date, spiro-OMeTAD is the most commonly used HTM, possessing a number of desirable attributes (i.e. a favourable glass transition temperature, appropriate energy level for hole extraction, low absorption within the visible spectrum, and good solubility in non-polar solvents, see section 1.4.2.4) that make them ideal in their application as HTMs for solution-processible PSCs. However, spiro-OMeTAD is expensive to produce (~$500 AUD/g) involving a multistep synthetic approach and time consuming purification process that accounts for more than 30% to the overall module cost and thus constituting one of the major drawbacks towards the cheap manufacturing of PSCs[147,232]. What's more, spiro-OMeTAD suffers from an inherently low conductivity, necessitating the use of additives and/or dopants such as LiTFSI (to facilitate oxidation of spiro-OMeTAD in the presence of oxygen to achieve hole-hopping conduction[233]) and TBP (understood only to prevent phase segregation of LiTFSI and hence improve HTM morphology[234,235]) to reach the necessary electrical conductivities that realize the high device efficiencies reported. Not only does the use of additives add costs on top of the already expensive spiro-OMeTAD, but unpredictable variations in the performance and stability of the entire device caused by (i) the lack of control of the oxidized spiro-OMeTAD concentration due to changes in the Li^+ ion concentration[236], (ii) diffusion and phase segregation of the additives within the HTM layer[121,122], and (iii) the hygroscopic properties of the additives that lead to accelerated cell

degradation[178], all suggest the additive approach to be inappropriate for PSCs. An alternative method to alleviate the issues associated with additives is to directly incorporate the oxidized form of spiro-OMeTAD. This has shown to provide a highly reproducible means of controllably increasing the conductivity of spiro-OMeTAD—up to 10^{-3} S cm^{-1} with the addition of 14% $spiro^{2+}$—without relying on oxidation in air[238]. This, however, does not avoid the prohibitively high costs of spiro-OMeTAD, as well as the inherent issue associated with its high sensitivity to various factors such as the current–voltage sweep direction[239,240] and changes to the level of oxygen or light exposure[179]. Thus, the development of stable, additive-free HTMs with inherently good charge transport ability to replace spiro-OMeTAD has been a major priority within the field that aims towards low-cost and stable PSCs.

A variety of additive-free HTMs have been investigated, with polymeric and organic compounds making up the majority of research efforts due to their flexibility in structure–property variation. Work on metal complex-based HTMs have also been done, but with an exclusive focus on planar molecules with high π-stacking capacity like phthalocyanines[192–194] and other extended π-conjugated molecules[195,196] and often requiring dopants as described in section 1.4.2.

4.2 Motivation and Strategy

The advantages associated with the use of high-denticity metal complexes—namely, their improved stability and low activation energy barriers for charge transfer—have been highlighted in section 1.5, and their successful application as an additive-free HTM demonstrated in section 3.3.7. Our success with the use of a high-denticity complex with lowered reorganization energy, indeed, provided the impulse for which to continue their exploration as HTMs for solar cells, this time, exploring the use of an iron metal center, i.e. (6,6′-bis(1,1-di(pyridin-2-yl)ethyl)-2,2′-bipyridine)iron ([Fe(bpyPY4)]).

Iron is the most vastly abundant of all metals on earth (comprising nearly 5.6% of the earth's crust and nearly all of the earth's core[241]), available at low cost and making it an optimum choice of material in the lead-up towards the industrial-scale production of PSCs. Moreover, possess relatively small energy barriers for charge transfer and therefore higher self-exchange rates compared to cobalt complexes due to their typically low-spin states[189,242]. This equates to a higher solid-state conductivity assuming hope-hopping is the dominant mode of conduction. For DSCs, the use of iron complexes has often resulted with poor efficiencies—in some cases, eliminating the photovoltaic effect altogether—due to the extremely kinetically fast charge recombination reactions between electrons in the TiO_2 and the oxidized iron species it can undergo[122]. In a PSC, the direct contact between TiO_2 and the HTM is typically shielded by a > 100 nm thick perovskite layer, eliminating the recombination pathway that exists between the ETM and CTM that can undermine the performance of solar cells. Here, the aims were to find the optimum blend of $[Fe(bpyPY4)]^{2+}$ and $[Fe(bpyPY4)]^{3+}$ that allows for an efficient hole-hopping charge transfer mechanism between the Fe(II) and Fe(III) centers, and investigate its application in a PSC and compare it with that of the traditionally employed spiro-OMeTAD HTM complex.

4.3 Results and Discussion

4.3.1 Synthesis and General Characterization

Synthesis of Fe(bpyPY4). The $[Fe(bpyPY4)](OTf)_2$ complex was synthesized following established procedures[48] as shown in Figure 45. Briefly, the metal trifluoromethanesulfonate (OTf) salt of Fe(II) was used for complexation with the bpyPY4 ligand in MeCN (scheme 1). The resulting complex was recrystallised twice by slow diffusion of diethyl ether (Et_2O) inside the MeCN solution to retrieve dark red crystals. $[Fe(bpyPY4)](OTf)_3$ was also synthesized through the same procedure as used for $[Fe(bpyPY4)](OTf)_2$, using the $Fe(OTf)_3$ salt reagent (90% purity) instead (scheme 3). A second method was also used to synthesize $[Fe(bpyPY4)](OTf)_3$ by the oxidation of $[Fe(bpyPY4)](OTf)_2$ with $NOBF_4$ of high oxidizing power (scheme 2). This, however, was found to be an inefficient oxidation process as was indicated by changes to the UV/Vis spectra of $[Fe(bpyPY4)](OTf)_3$ with increasing amount of $NOBF_4$ (exceeding 1 eq.) shown in Figure 46. The former method was therefore used for all subsequent studies.

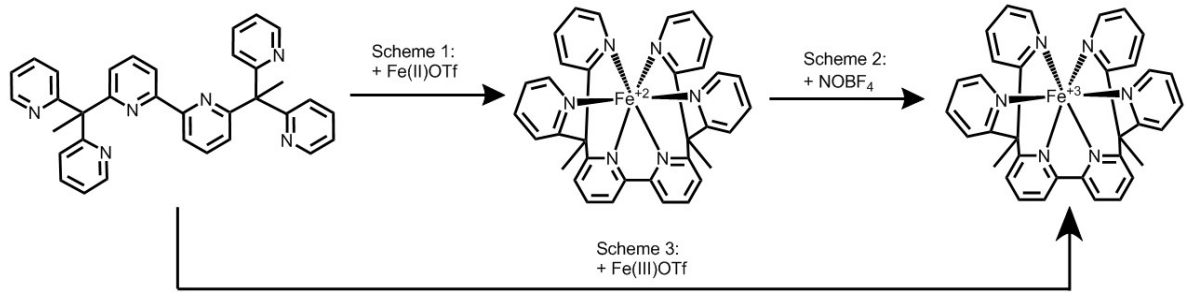

Figure 45. Synthetic schemes for $[Fe(bpyPY4)](OTf)_2$ (scheme 1), $[Fe(bpyPY4)](OTf)_2(BF_4)$ (scheme 2) and $[Fe(bpyPY4)](OTf)_3$ (scheme 3).

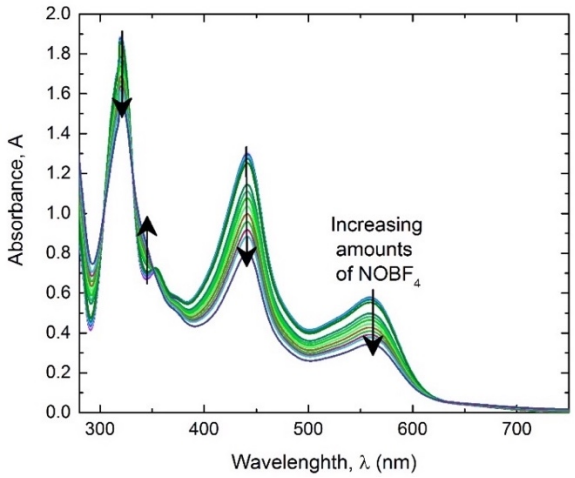

Figure 46. Oxidation of [Fe(bpyPY4)](OTf)$_2$ with increasing amounts of $NOBF_4$ (0 to 2 eq.)

Structure. The molecular structures of $[Fe(bpyPY4)]^{3+}$ and $[Fe(bpyPY4)]^{2+}$, as derived from single crystal XRD data of crystals grown from materials synthesized through schemes 1 and 3 are shown in Figure 47. Here, the bpyPY4 ligand is coordinated to the iron centers and adopts octahedral geometries in both Fe(II) and Fe(III) states with very similar coordination spheres. The refinement of these data suggests a triclinic lattice with a P-1 space group for the Fe(II)-based complex and a monoclinic lattice with a P21/n space group for the Fe(III)-based complex. Changes in the metal-ligand bond lengths between pairs of identical Fe-N bonds in the Fe^{2+} and Fe^{3+} states are tabulated in Table 3. Analysis reveals extremely small changes in all directions with a calculated average of ΔX = 0.014 Å, indicative of the extremely minor geometrical changes that are experienced during the charge transfer between the Fe(II) and Fe(III) centers. This is around six times smaller than the Fe–N bond changes reported for an iron bipyridyl complex ($\Delta X \sim 0.067$)[243], and a ΔG_{inner} that is < 95% smaller (according to Eq. 8, see section 3.1).

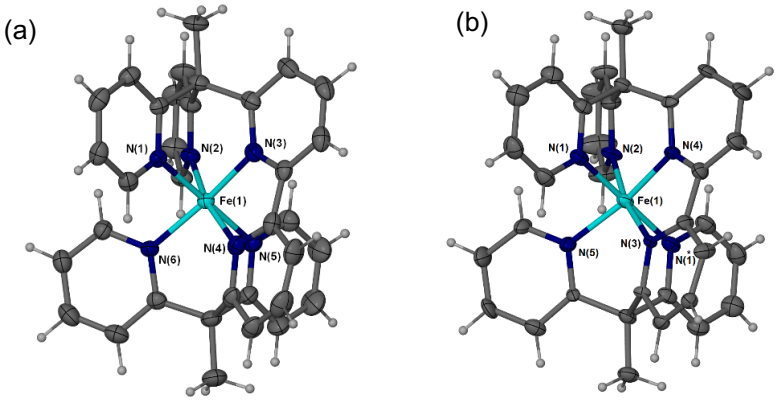

Figure 47. Spatial structures of the **(a)** $[Fe(bpyPY4)]^{2+}$ and **(b)** $[Fe(bpyPY4)]^{3+}$ cations as derived from single crystal XRD.

Table 3. Metal-Ligand bond lengths for $[Fe(bpyPY4)])OTf)_2$ and $[Fe(bpyPY4)])OTf)_3$

Metal-Ligand	$[Fe(bpyPY4)])OTf)_2$ (Å)	$[Fe(bpyPY4)])OTf)_3$ (Å)	ΔX (Å)
Fe-N1	1.9764	1.976	0.0004
Fe-N2	1.9764	1.958	0.0184
Fe-N3	1.972	1.942	0.03
Fe-N4	1.92	1.933	0.013
Fe-N5	1.977	1.975	0.002
Fe-N6	1.939	1.96	0.021

Solubility. The iron complexes all contained the OTf^- counter ion, and, as was expected, were found to exhibit excellent solubility in solvents such as MeCN and nitromethane (as was deemed necessary for its use in a perovskite solar cell) and of which the highest concentrations used were 50 mM Fe(II) and 50 mM Fe(III) during the fabrication of solar cells.

Energy level. To confirm its compatibility with the light absorbing materials available, cyclic voltammetry (CV) was the method used to determine the highest occupied molecular orbital energy level (HOMO). CV was performed on 5mM $[Fe(bpyPY4)](OTf)_2$ solutions in CH_3CN containing 0.1 M *n*-Bu_4PF_6 as a supporting electrolyte. From the CV shown in Figure 55, the complex undergoes a chemically reversible oxidation with a midpoint potential of 0.54 V vs. $Fc^{0/+}$ attributed to the Fe(II/III) transition, equating to –5.57 eV vs. vacuum assuming that the formal potential of the $Fc^{0/+}$ redox couple is 5.1 eV [244]. This HOMO energy level position was found to be significantly lower than was found

for spiro-OMeTAD measured under the same conditions, between –5.14 eV vs. vacuum (comparing well with literature[169]).

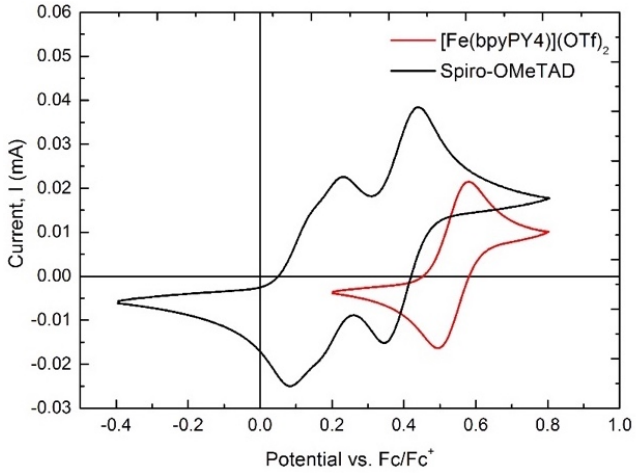

Figure 48. Cyclic voltammograms of a 3 mM solution of [Fe(bpyPY4)])$OTf)_2$ in MeCN and 2.3 mM solution of spiro-OMeTAD in MeCN:CBZ (3.38:1), each measured at a scan rate of 100 mV s^{-1}, with 0.1 M $TBAPF_6$ as a supporting electrolyte under nitrogen.

4.3.2 Thin Film Conductivity

As explained in section 3.3.2, the conductivity is in a first approximation is proportional to the density number of charge carriers which, for a molecular based conductor, can be controlled by tuning the ratio of oxidized to reduced molecular species. Here, two-probe interdigitated array (IDA) microelectrodes were used to assess the conductivity of drop-casted films. Following the same naming convention as used in the previous chapter, we define $[Fe(bpyPY4)](OTf)_{2+x}$ films as the compositional mixture of Fe(II) and Fe(III) with $0 \leq x \leq 1$ (see Eq. 9, section 3.3.2).

Preparation of HTM precursor solution. Inside a glovebox, equimolar solutions (50mM) of $[Fe(bpyPY4)](OTf)_2$ and $[Fe(bpyPY4)](OTf)_3$ were prepared in MeCN. Solutions of various compositions (from Fe^{2+} to Fe^{3+}) were then prepared by mixing the required amounts of the aforementioned solutions. For comparison with a standard hole conducting material, a 10% oxidized spiro-OMeTAD solution in chlorobenzene was prepared. Briefly, spiro-OMeTAD dissolved in dichloromethane was oxidized by reaction with an equimolar amount of Ag(OTf) to give spiro-OMeTAD(OTf) and Ag^0. Silver

particles were removed by filtration and spiro-OMeTAD(OTf) purified via precipitation from the solution with diethyl ether. 10 mol % of spiro-OMeTAD$(OTf)_2$ was added to the spiro-OMeTAD solution used for the experiments.

Room temperature conductivity. Linear current-voltage dependencies were obtained for all blends, demonstrating ideal ohmic contact with the gold electrodes, while the iron-free ligand molecule showed very little conductivity. Here, it was observed that even a small addition of [Fe(bpyPY4)]$(OTf)_3$ to [Fe(bpyPY4)]$(OTf)_2$ increased the conductivity by three orders of magnitude from 10^{-7} S m^{-1} to 10^{-4} S m^{-1}, while further enhancements (x > 0.1) were not that significant (Figure 49). A maximum room temperature conductivity of 2.4 x 10^{-4} S m^{-1} was achieved with 80 mol% [Fe(bpyPY4)]$(OTf)_3$, almost five-fold higher than 5.1 x 10^{-5} S m^{-1} measured under the same conditions for the reference organic HTM, 10% oxidized spiro-OMeTAD.

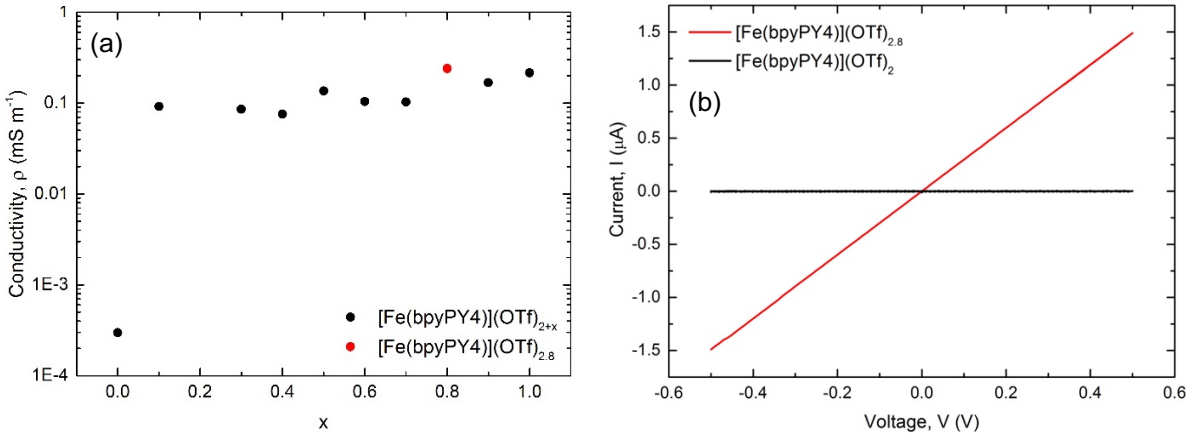

Figure 49. (a) Room-temperature conductivity of various blends of the [Fe(bpyPY4)]$(OTf)_2$ and [Fe(bpyPY4)]$(OTf)_3$, and **(b)** I–V curve of pristine [Fe(bpyPY4)]$(OTf)_2$ (red) and the film of optimized composition, [Fe(bpyPY4)]$(OTf)_{2.8}$ (red), showing ideal ohmic behaviour

Variable temperature conductivity and Arrhenius behaviour. Conductivity measurements were undertaken for [Fe(bpyPY4)]$(OTf)_{2.8}$ and doped spiro-OMeTAD thin films at different temperatures (210-300 K range). Both HTMs exhibited an exponential increase of resistivity with lowering temperature (Figure 50a). The corresponding Arrhenius plot (Figure 50b) shows the expected linear relationship that is typical for semiconducting materials in which thermally activated hopping is the dominant mode of charge transport. The corresponding activation energies derived from the linear fits to

the experimental data were 0.36 eV for $[Fe(bpyPY4)](OTf)_{2.8}$ and 0.31 eV for the 10% oxidized spiro-OMeTAD thin films, the latter value consistent with the one found in literature[245].

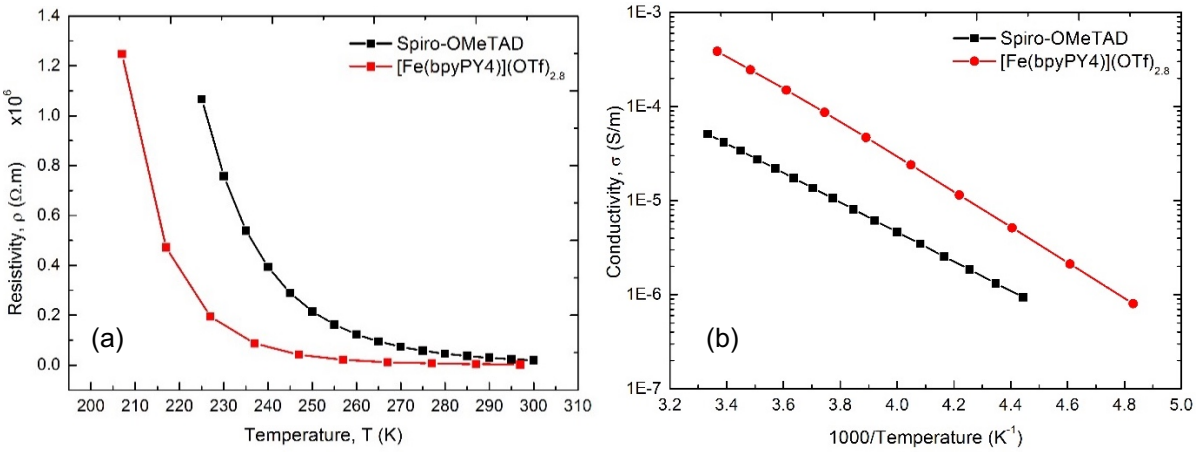

Figure 50. (a) Resistivity curves and **(b)** Arrhenius plots of the conductivity of the $[Fe(bpyPY4)](OTf)_{2.8}$ (red) and 10% oxidized spiro-OMeTAD (black) thin films drop-cast onto IDA electrodes.

4.3.3 Thin Film Morphology

X-ray diffraction of films. XRD patterns of $[Fe(bpyPY4)](OTf)_{2.5}$ films obtained by drop-casting and spin-coating show that the film morphology is independent of the deposition strategy (Figure 51a). GAXRD of a spin-coated $[Fe(bpyPY4)](OTf)_{2.5}$ film on a silicon substrate was also obtained (Figure 51b). In all spectra, three very broad diffraction peaks are identified at 9.5°, 14.5° and 24.2°. The broadness of the peaks suggest films to be mostly amorphous, with some indication of short-range order in the nanometer range. The features of the spectra found here are very much alike to the one obtained for the cobalt analogue in section 3.3.3. Thus, it appears as though the central metal atom plays little role in determining the morphology of spin-coated thin films and are possibly arising from the ligand forming the majority of the thin films studied here.

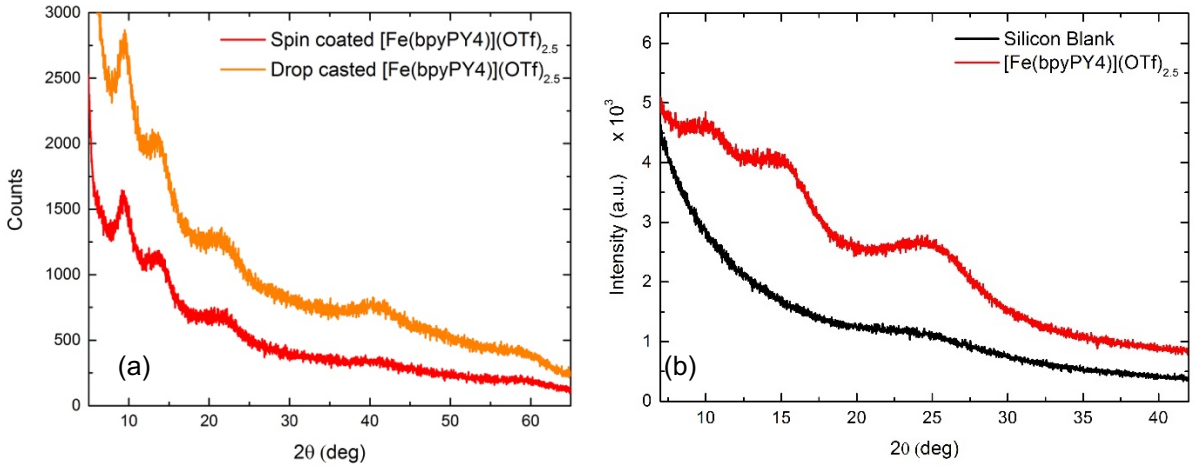

Figure 51. (a) XRD patterns of films deposited by drop-casting (orange) and spin-coating (red). **(b)** GAXRD of a 0.95 μm thick film spin-coated onto a single crystalline Si substrate (red), and the uncoated substrate (black).

Electron Microscopy. Nanoscale morphology of drop-casted films was investigated further by electron microscopy, and both a high-resolution transmission electron micrograph (HRTEMs, Figure 52a) and selected area diffraction pattern (SAED, Figure 52b) are shown. On the contrary to what was observed for the cobalt analogue, the HRTEM image shows drop-casted films of $[Fe(bpyPY4)](OTf)_{2.5}$ to possess micro-crystallites with ribbon-like morphology that stems from a nucleation point. The SAED patterns from individual crystal ribbons were obtained at various diffraction angles, displaying high symmetry single-crystal diffraction spots.

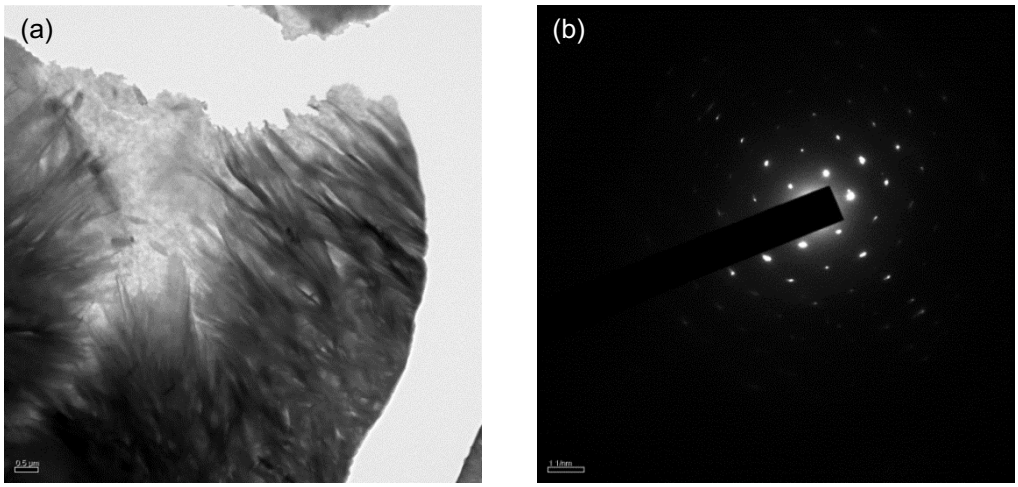

Figure 52. (a) HRTEM and **(b)** SAED pattern of a drop-casted $[Fe(bpyPY4)](OTf)_{2.5}$ film.

4.3.4 Optical Studies

Optical Absorption of solutions and films. In the UV/Vis absorption spectra of solutions, three major peaks resulting from one ligand-based transition (320-325 nm) and two metal-to-ligand charge transfer transitions (440-450 and 560-570 nm) can be identified for both $[Fe(bpyPY4)](OTf)_2$ and $[Fe(bpyPY4)](OTf)_3$, and an additional characteristic weak peak observed at 350 for $[Fe(bpyPY4)](OTf)_2$ which disappears as a broadened shoulder around 330 nm in the case of $[Fe(bpyPY4)](OTf)_3$, Figure 53. Maximum extinction coefficients of 18600 M^{-1} cm^{-1} (321 nm) and 12000 M^{-1} cm^{-1} (324 nm) for $[Fe(bpyPY4)](OTf)_2$ and $[Fe(bpyPY4)](OTf)_3$, respectively. The UV/Vis spectra for the corresponding thin films are shown in Figure 53b, with similar characteristic peaks observed.

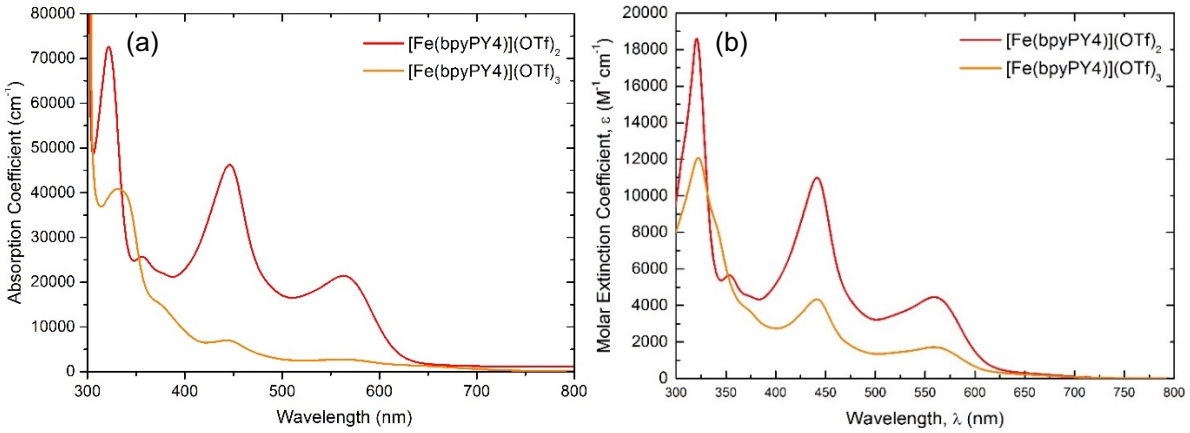

Figure 53. (a) Molar extinction coefficient spectra of thin films spin-coated on glass and **(b)** absorption coefficient spectra of MeCN-based solutions of $[Fe(bpyPY4)](OTf)_2$ (red) & $[Fe(bpyPY4)](OTf)_3$ (orange).

Electronic coupling. To investigate the presence of electronic coupling, the experimentally determined absorption spectra of $[Fe(bpyPY4)](OTf)_{2.5}$ are compared to those calculated from the individual spectra of the components using the (calculated by: $A[Fe(bpyPY4)](OTf)_{2.5} = 0.5[Fe(bpyPY4)](OTf)_3 + (1 - 0.5)[Fe(bpyPY4)](OTf)_2$), Figure 54. The absence of broadening and minor shifts in the UV/Vis, of both solution and the solid films, relative to the calculated combination of the individual reduced and oxidized species suggests a lack of electronic coupling between the ions.

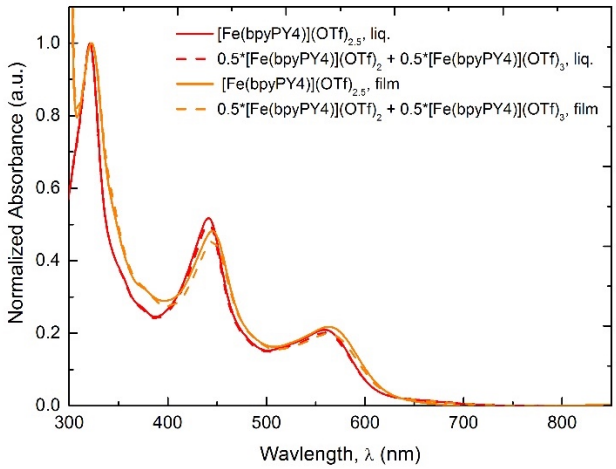

Figure 54. Normalized UV/Vis absorption spectra for solid-state films and MeCN liquid solutions of [Fe(bpyPY4)](OTf)$_{2.5}$, both experimental (solid lines) and calculated spectra (dotted lines).

4.3.5 Application as HTM in PSC

Energy level compatibility of components. In section 4.3.1, a HOMO level of –5.57 eV vs. vacuum was obtained. In comparison to a vast majority of the HTMs investigated thus far, this HOMO is relatively low, and thus necessitates the use of a light absorbing material which also has a deep HOMO level, and more positive with respect to itself to provide the essential driving force for hole extraction. This HOMO level was found to be particularly matched with the $FAPbBr_3$ perovskite light absorber. Upon inspection of the constructed energy level diagram (Figure 55), a driving force of 0.37 eV for hole injection from $FAPbBr_3$ into [Fe(bpyPY4)](OTf)$_{2.5}$ is estimated. Moreover, a V_{OC} exceeding that attained with spiro-OMeTAD is expected.

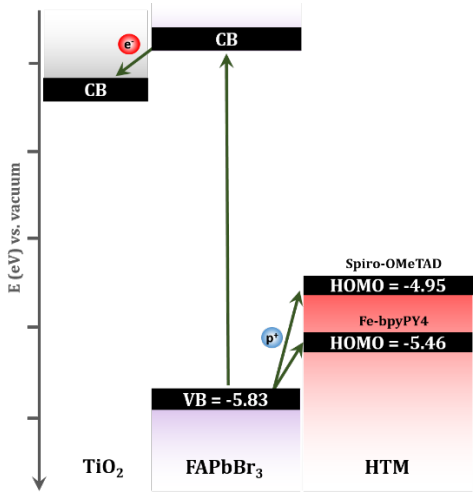

Figure 55. Energy level diagram for a Fe(bpyPY4) and spiro-OMeTAD-based PSC with the $FAPbBr_3$ perovskite light absorber.

$FAPbBr_3$-based PSC Fabrication. Given their compatibility, $FAPbBr_3$ based PSCs cells were fabricated employing $[Fe(bpyPY4)](OTf)_{2+x}$ as the HTM to showcase the applicability of these solution-processable materials as HTMs in solar cells. PSCs with a planar Au/HTM/$FAPbBr_3$/c-TiO_2/FTO architecture (FTO – glass covered with fluorine-doped tin(IV) oxide; c-TiO_2 – compact titania blocking layer) were fabricated and encapsulated under nitrogen (see section 2.3.2 for experimental details). $[Fe(bpyPY4)](OTf)_{2+x}$ is poorly soluble in the relatively nonpolar solvents commonly employed for the HTM deposition in PSCs. This problem was addressed by using nitromethane to prepare the Fe-based HTM deposition solutions. Importantly, this solvent did not dissolve or damage the $FAPbBr_3$ layers, thus enabling the use of more polar HTMs in all solution-processed PSCs. Planar $[Fe(bpyPY4)](OTf)_{2+x}$-based perovskite devices with the structure FTO/c-TiO_2/$FAPbBr_3$/HTM/Au were built by spin coating a nitromethane-based precursor solution of $[Fe(bpyPY4)](OTf)_{2+x}$. The SEM cross-section of a device reveals the pinhole-free layers of the device and the dense monolayer of perovskite crystal grains (Figure 56).

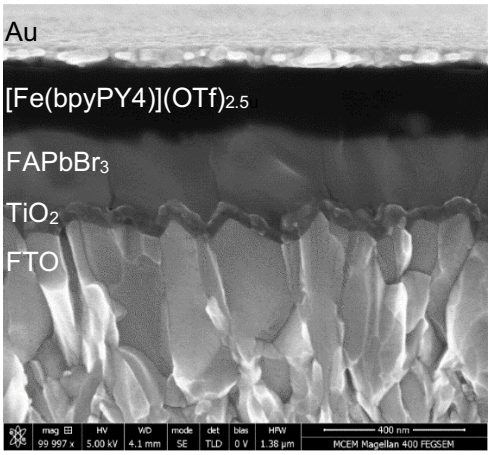

Figure 56. Cross-sectional SEM image of a $FAPbBr_3$ perovskite device with $[Fe(bpyPY4)](OTf)_{2.5}$ as the HTM.

Optimization of devices. Initial tests on PSCs based on $[Fe(bpyPY4)](OTf)_{2+x}$ with $0 \leq x \leq 1$ revealed that the HTM must contain at least a small amount of Fe(III) to enable reasonable photovoltaic performance, which is most probably due to the very low conductivity of $[Fe(bpyPY4)](OTf)_2$ as was observed in section 4.3.2. Furthermore, the PCE peaked at x = 0.5, though differences in the solar cell efficiencies at higher Fe(III):Fe(II) ratios were not significant. Thus, detailed device performance studies reported herein were undertaken for x = 0.5, i.e. $[Fe(bpyPY4)](OTf)_{2.5}$. In the preliminary experiments, 4-tert-butylpyridine (TBP) and lithium bis(trifluoromethanesulfonyl)imide (LiTFSI) were introduced into the HTM solutions. However, further studies indicated that the best performance of the solar cells based on both spiro-OMeTAD and $[Fe(bpyPY4)](OTf)_{2+x}$ are achieved with additive-free HTM layers.

Device performance A summary of the photovoltaic parameters for a representative population of the $FAPbBr_3$ solar cells with $[Fe(bpyPY4)](OTf)_{2.5}$ or spiro-OMeTAD as HTM is reported in Table 1. The current density vs. potential (J–V) curves for both scan directions and incident photon to current efficiency (IPCE) spectra are exemplified in Figure 57. The best-performing device fabricated with $[Fe(bpyPY4)](OTf)_{2.5}$ reached a highest efficiency of 2.2%. (average of 2.0%, with V_{OC} = 855 mV, J_{SC} = 6.0 mA cm^{-2}, FF = 42%), whilst the best performing device fabricated with spiro-OMeTAD- achieved a highest efficiency of 5.2% (average of 4.9 %, with V_{OC} = 1310 mV, J_{SC} = 6.6 mA cm^{-2}, FF = 60). Remarkably, the spiro-OMeTAD-based devices performed best without the use of the

common additives to HTM, TBP and LiTFSI. Inspection of the data in Table 4 indicates that low FF and V_{OC} contribute to lower efficiencies of the PSCs based on the iron complex HTM.

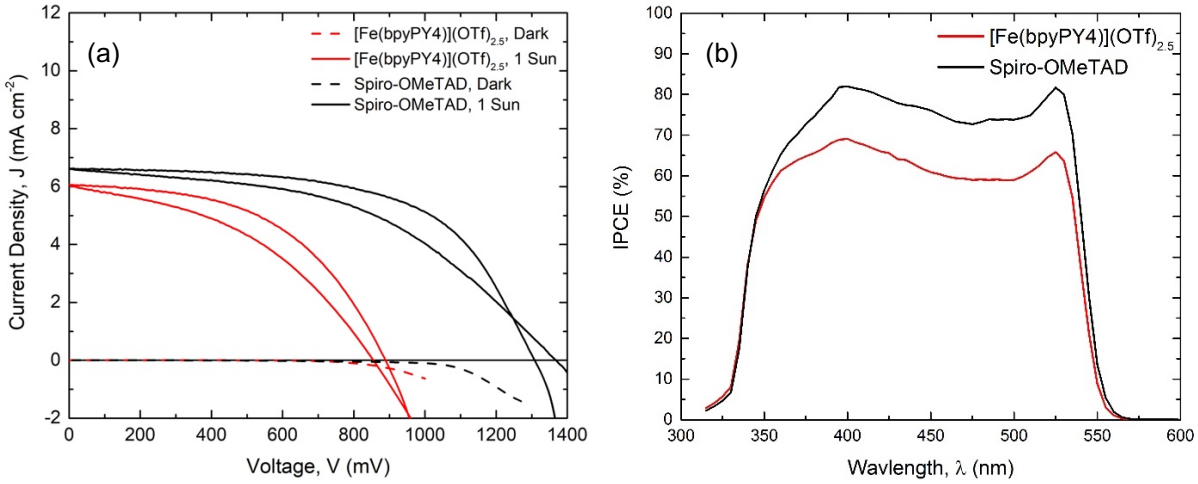

Figure 57. (a) J–V curves and **(b)** IPCE spectra for the best-performing $FAPbBr_3$ PSCs based on the $[Fe(bpyPY4)](OTf)_{2.5}$ (red) and spiro-OMeTAD (black) HTMs, measured under standard AM1.5G irradiation (solid curves) and in the dark (dashed curves).

Table 4. Photovoltaic performance data for PSCs employing different HTMs and $FAPbBr_3$, measured under standard AM1.5G Irradiation.

HTM	V_{OC} [mV]	J_{SC} [mA cm^{-2}]	FF [%]	PCE [%]
Spiro-OMeTAD	1290 ± 40	6.3 ± 0.4	61 ± 6	4.9 ± 0.4
$[Fe(bpyPY4)](OTf)_{2.5}$	760 ± 60	6.1 ± 0.3	42 ± 2	2.0 ± 0.3

Quasi-steady-state and long-term stability. Quasi-steady-state measurements at maximal power potentials for the $[Fe(bpyPY4)](OTf)_{2.5}$ devices (Figure 58a) produced conversion efficiencies that were close to those derived from the short-circuit to forward bias sweeps of the J–V curves (Figure 57). To test the long-term stability, sealed devices were subjected to long-term light-soaking (120 hours) (at a light intensity of 100 mW cm^{-2}, a temperature of 25°C, and humidity level of 20%) and were maintained at the optimal electric power output during ageing using maximum power point tracking. As shown in Figure 58b, the efficiency of $[Fe(bpyPY4)](OTf)_{2.5}$-based devices reduced down to ~40% of its initial efficiency after 40 hours, whilst the spiro-OMeTAD-based devices experienced a larger drop to only ~22% of its initial efficiency.

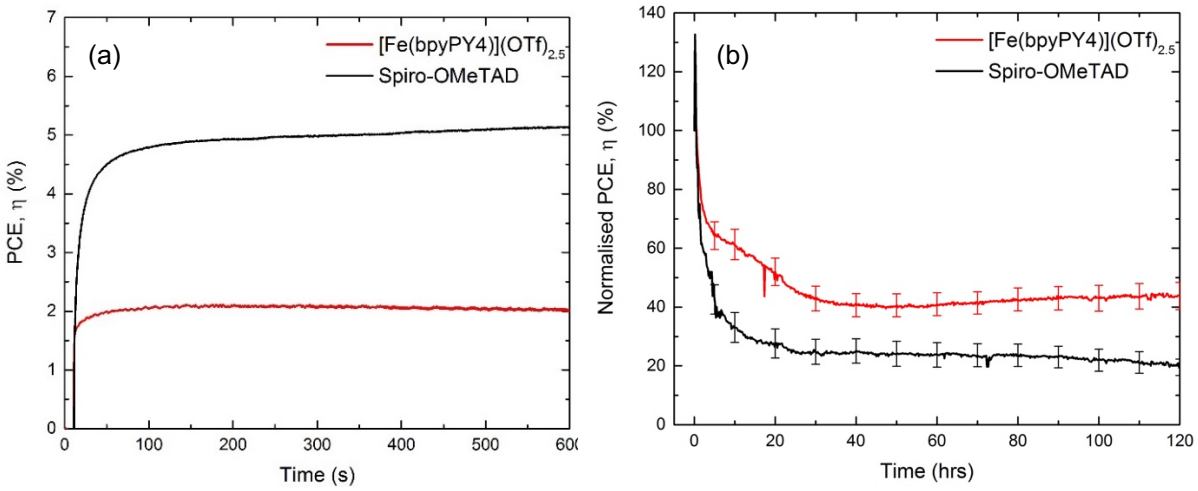

Figure 58. (a) Maximum-power-point PCE transients measured under standard AM1.5G irradiation for the best-performing spiro-OMeTAD-based (black curve, applied voltage 926 mV) and $[Fe(bpyPY4)](OTf)_{2.5}$-based (red curve, applied voltage 529 mV) solar cells. **(b)** Evolution of photo-conversion efficiency (PCE) of encapsulated $FAPbBr_3$-based planar solar cells fabricated with spiro-OMeTAD (black) or $[Fe(bpyPY4)](OTf)_{2.5}$ (red) as a HTM under continuous 1 sun irradiation at 25 °C (actual cell temperature was higher due to continuous irradiation) and 20% relative humidity.

Hole extraction. To confirm hole extraction, fluorescence quenching of the $FAPbBr_3$ perovskite in contact with $[Fe(bpyPY4)](OTf)_{2.5}$ and spiro-OMeTAD HTMs were performed. As shown in Figure 59, highly efficient charge injection from $FAPbBr_3$ into $[Fe(bpyPY4)](OTf)_{2.5}$ was proven by the more than 99% intensity suppression when deposited on top of the perovskite layer.

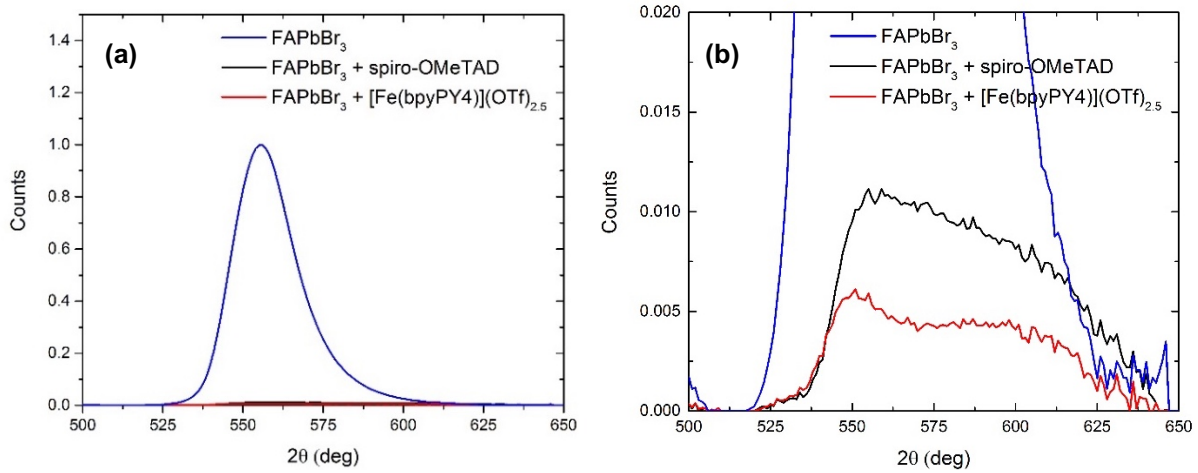

Figure 59. Photoluminescence quenching of $FAPbBr_3$ perovskite films **(a)** at full range and **(b)** zoomed in. An excitation wavelength of 380 nm was used.

Rectifying behaviour. J-V characterization of the FTO/c-TiO_2/[Fe(bpyPY4)](OTf)$_{2.5}$/Au diode (Figure 60) shows perfect rectifying behaviour and demonstrates a built-in voltage of 600 mV and negligible photocurrent suggesting that the HTM layer itself does not produce additional shunt resistance and does not contribute significantly to the lower FF of the diodes. The small photocurrent (300 μA cm^{-2} at −0.3 V) is generated by titania as confirmed in control experiments undertaken with no Fe(bpyPY4)](OTf)$_{2.5}$ present.

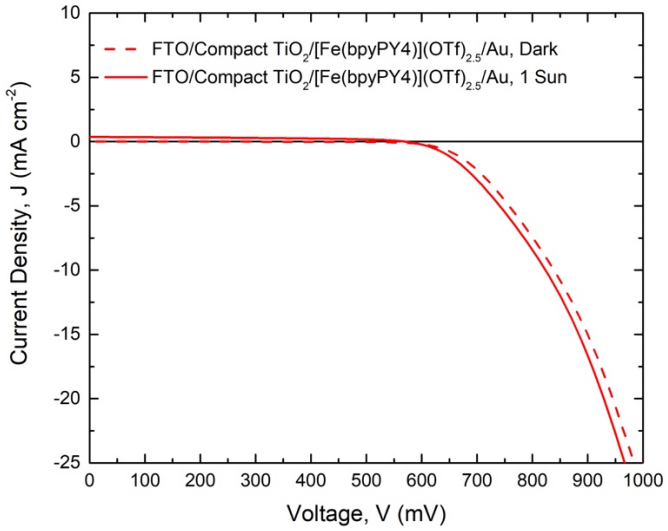

Figure 60. J-V curve of the FTO/c-TiO_2/[Fe(bpyPY4)](OTf)$_{2.5}$/Au diode.

V_{OC} limitations. Data in Figure 55 suggest that the open-circuit voltage for the [Fe(bpyPY4)](OTf)$_{2.5}$ HTM should be higher than for spiro-OMeTAD, which contrasts with our experimental observations. The underlying reasons for lower than expected V_{OC} achieved with the [Fe(bpyPY4)](OTf)$_{2.5}$ HTM integrated with the $FAPbBr_3$ perovskite, however, could not be established. In principle, this can be rationalized in terms of its insufficient driving force for the charge transfer between [Fe(bpyPY4)](OTf)$_{2.5}$ and $FAPbBr_3$ as defined by the small differences between their HOMO and E_{VB} together with its expected fast recombination kinetics (see section 4.3.1) that can facilitate recombination losses at the perovskite/HTM interface. This hypothesis is supported by a more than 3-fold higher recombination resistance derived from electrochemical impedance spectra recorded for the spiro-OMeTAD-based solar cell (1250 Ω) as compared to that obtained for the device with [Fe(bpyPY4)](OTf)$_{2.5}$ as a HTM (400 Ω)

around their open circuit voltages. However, further scrutiny is needed to establish the reasons for the comparatively low V_{OC} and FF achieved here with the new HTM.

4.4 Summary and conclusions

In conclusion, a non-planar iron complex based on a hexadentate polypyridyl ligand as a solid-state, solution-processable, additive-free HTM for a PSC was investigated. The conductivity of films containing blends of $[Fe(bpyPY4)](OTf)_2$ and $[Fe(bpyPY4)](OTf)_3$ were measured, in which the films of $[Fe(bpyPY4)](OTf)_2$ resulted in a 10^3-fold increase in conductivity upon addition of 80 mol% of its oxidized counterpart. Compared to the benchmark 10% oxidized spiro-OMeTAD films, $[Fe(bpyPY4)](OTf)_{2.8}$ exhibited higher conductivity and a more negative HOMO. Unlike the cobalt analogue investigated in Chapter 3, the resistivity behaviour for both pristine and mixed films displayed Arrhenius conductive behaviour. SEM and TEM show films of $[Fe(bpyPY4)](OTf)_{2.8}$ to possess micro-crystallites with ribbon-like morphology, again, in striking contrast to what was observed for the cobalt analogue.

The electronic configuration of this iron complex necessitated the use of a perovskite material with a sufficiently low valence band energy (E_{VB}), formamidinium lead bromide ($FAPbBr_3$) perovskite, to maximize the open circuit voltage of the resulting devices. Here, an energy conversion efficiency of 2.2 % was achieved when applied as an additive-free HTM in a planar $FAPbBr_3$ PSC. Despite the higher conductivity and lower HOMO level, the open-circuit voltage of the PSCs employing the Fe-based HTM was lower than expected and inferior to the V_{OC} of the devices with a conventional organic hole-transport material. Extended studies on the origins of this phenomenon are identified as future work. Most importantly, the present report provides the first demonstration of the capacity of a transition metal complex to sustain efficient hole transport in all-solid-state PSCs via the redox activity of the metal center. We anticipate that this finding might open up new possibilities for design of efficient and versatile hole transporting materials for perovskite and other solar cells.

Chapter 5:

Copper Bis-Phenanthroline Complexes as Redox Mediators for Dye-Sensitized Solar Cells

The following chapter describes the use of copper bis-phenanthroline complexes as redox mediators in liquid-based DSCs. Furthermore, an investigation of the role of 4-tert-butylpyridine (TBP) on the performance of DSCs employing the copper complexes is investigated.

Copper Bis-Phenanthroline Complexes of Redox Mediators for Dye-Sensitized Solar Cells

Chapter contents

5.1 Introduction

DSCs are promising, inexpensive technologies, with a unique property of being able to perform exceptionally well under diffuse and low-light conditions[99,183–186]. Iodide/tri-iodide redox couples have been the traditional choice of redox mediator[41]. However, as highlighted in section 1.4.1, the major drawbacks associated with its corrosive nature, large potential loss due to its fixed redox potential and mismatch with commonly used dyes has ultimately hampered its future potential[41]. Since then, a major shift from halogen-based redox mediators to the transition metal complex mediators based on the one-electron transfer mechanism has taken place, with Co(III/II)-based complexes taking lead due its several features—such as non-volatility, non-corrosiveness, low absorptivity, and more positive/tuneable redox potentials through ligand manipulation—and have reached device efficiencies as high as 14.3%[246]. Their main downfall, however, is their relatively large reorganization energy barrier attributed to the spin changes (high-spin Co^{2+} to low-spin Co^{3+}) of the cobalt metal center during the redox process, necessitating a driving force greater than 0.25 V for efficient dye regeneration that constitutes a significant potential loss[221]. Various efforts to reduce the reorganization energy have indeed taken place, such as the use of a strong field ligand (trithiacyclononane, ttcn) that force both the Co^{2+} and Co^{3+} oxidation states to adopt low-spin configurations[120], as well as the use of high-denticity pentadentate and hexadentate ligands (PY5Me_2 and bpyPY4) that form rigid structures and minimize changes in the Co-Ligand bond lengths (see section 3.1). A completely different approach has been to employ alternative redox active metal centers, in particular, those based on the abundant and relatively non-toxic Cu(II/I) metal center that can undergo fast reorganization. With efficiencies now going beyond the 10% mark[206], a revisitation of copper complexes as redox mediators for DSCs has taken recently taken place.

Reducing the Inner-Sphere Reorganization Energy of Copper Complexes

Like Co(III/II) complexes, Cu(II/I) complexes, too, can suffer from high reorganizational energies. This, however, is a result of the different preferred geometries that are normally adopted by the 4-coordinate Cu(I) (tetrahedral) and typically 4- or 5-coordinate Cu(II)

(square-planar or trigonal bipyramidal) species[247]. Thus, ligand design is of crucial importance in attaining the much desirable low reorganization energy. The key approach is to employ ligands that force the copper-ions to remain 'fixed' in certain geometries during the redox transformation from Cu(I) to Cu(II) (and vice versa)[191,248] thus allowing for fast exchange kinetics that lead to efficient dye regeneration at small overpotentials. Notable examples include bis(2,9-dimethy-1,10-phenanthroline)copper(II/I) ($[Cu(dmp)_2]^{+/2+}$) and bis-(4,4',6,6'-tetramethyl-2,2'-bipyridine)copper(II/I) ($[Cu(tmby)_2]^{+/2+}$). When employed as redox mediators, impressive solar efficiencies of 8.3%[249] and 10.3%[250], respectively, are obtained with high open circuit voltages (>1 V) well-exceeding that of the traditionally used Co(III/II) complexes, and driving forces as low as 0.1 V for efficient dye regeneration[118]. More impressively, solar conversion efficiencies of 8.2%[202] and 11%[56] have been recently achieved as solid-state HTMs in the so-called "zombie" ssDSC. Indeed, the fast redox properties exhibited by the said complexes have been attributed to their low internal reorganization energies, λ_{in}, caused by the distorted geometries induced by the bidentate pyridyl-based ligands in addition to their fast diffusion properties (in an electrolyte) in addition to their relatively lower-lying redox potentials that allow for higher device photovoltages.

5.2 Motivation and Strategy

The small reorganization of the copper complexes has been highlighted as one of the key attributes towards their impressive performances as both redox mediators in DSCs and HTMs in ssDSCs. Among those reported thus far, $[Cu(dmp)_2]^{+/2+}$ is the most well-studied copper based redox mediator and has been calculated to attain the fastest electron self-exchange rate (23 $M^{-1}s^{-1}$) and the lowest inner sphere reorganization energy (λ_{in} = 0.281 eV)[56]. Here, the strategy is to further reduce the reorganization energy of the phenanthroline-based copper complex by the addition of bulky substituents to the ligand that increase sterical hindrance and which force the ligand conformations of both oxidation states to be the same. The aims were to employ the newly designed copper complex as redox mediator, and to probe whether a reduction in reorganization is beneficial towards regeneration of the light absorbing material and its conductivity.

5.3 Results and Discussion

5.3.1 DFT Calculations of the Reorganization Energy

To develop a preliminary understanding, a computational estimation of the reorganization energies for a series of copper phenanthroline-based complexes was performed. Systematic substitutions at the 2-,9-positions of the phenanthroline ligand with groups of increasing bulkiness was used for calculations, i.e. methyl < butyl < *tert*-butyl < phenyl (Figure 61). For the purpose of making simple comparisons, the inner sphere reorganization (which arises purely as a result of the geometrical adjustment of the molecule) was used here to provide an upper bound value for the charge transport energetics. The purpose of this study was to develop trends only, providing insights into the relative effects each substituent has on the reorganization of the complex and to develop a basis upon which to continue these studies.

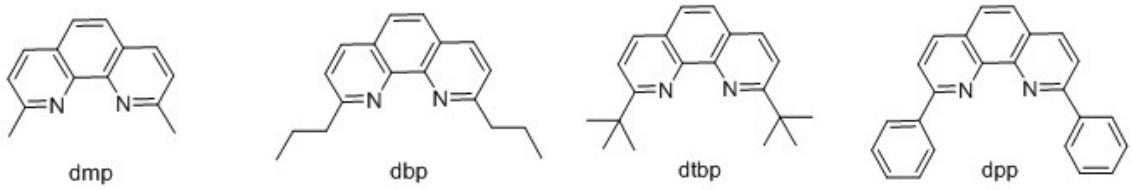

Figure 61. Ligand designs; 2,9-dimethyl-1,10-phenantroline (dmp, the reference ligand), 2,9-dibutyl-1,10-phenantroline (dtp), 2,9-tert-butyl-1,10-phenanthroline (dtbp) and 2,9-diphenyl-1,10-phenantroline (dpp).

Calculation method. The estimations for obtaining the free energies and optimised ground state geometries were carried out based on density functional theory (DFT) using Gaussian-09 rev. A. 02 package (see section 2.2.5 for details). Briefly, the crystal structures of previously determined $Cu(dmp)_2$ complexes, wherever available, were used as initial guesses to obtain structurally optimised ground state structures. The level of theory employed was B3LYP coupled with ς def2-svp[154], which has previously been identified to work well in estimating the structural parameters and reorganization energies of copper-phenanthroline complexes[251]. Calculations were performed in the gas phase to avoid the complications of outer sphere contributions, and the inner sphere reorganization energy, λ_i calculated according to literature[252,253], in which the individual contributions by the reduced λ_{red} and oxidized λ_{ox}states were summed.

DFT results. As shown in Figure 62, the simulated minimum energy structures of the Cu(I) and Cu(II) complexes adopt distorted tetragonal geometries. Substituents at the 2,9 positions were found to cause a systematic drop of the reorganization energies of the formed complexes with increasing bulkiness—values of 58.2, 40.8, 38.9 and 32.4 kJ/mol calculated for the methyl-, butyl-, *tert*-butyl, and phenyl substituents, respectively (Table 5)—correlating well with overall differences in the dihedral angles between the Cu(I) and Cu(II) geometries as shown.

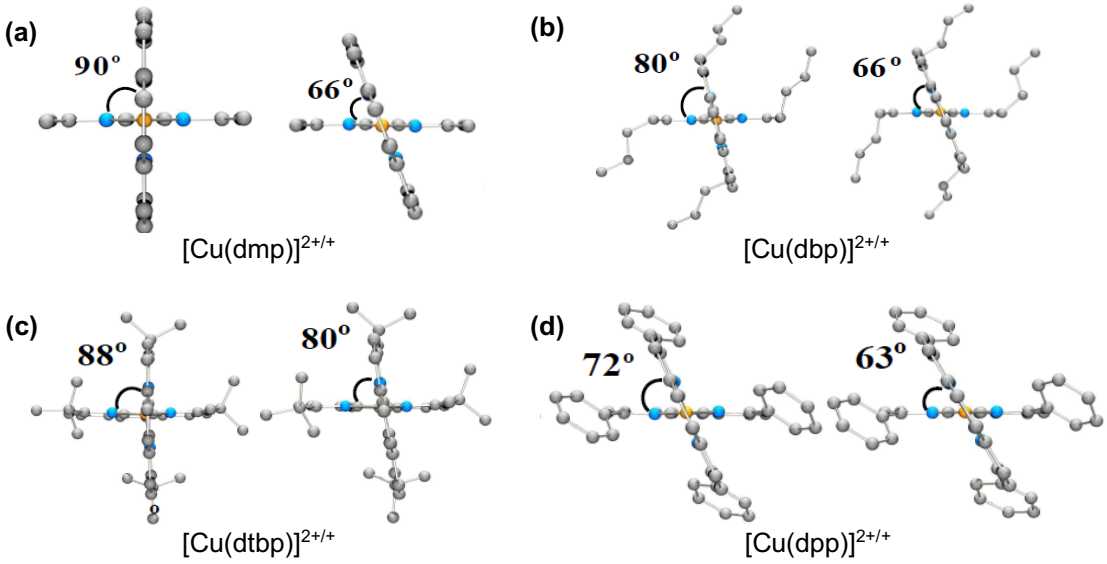

Figure 62. Minimum energy structures of the various substituted Cu(I) (left) and Cu(II) (right) phenanthroline complexes, provided by Dr. Shravan Acharya; **(a)** bis(2,9-dimethyl-1,10-phenantroline)copper(I/II) ($[Cu(dmp)]^{+/2+}$), **(b)** bis(2,9-dibutyl-1,10-phenantroline)copper(I/II) ($[Cu(dbp)]^{+/2+}$), **(c)** bis(2,9-tert-butyl-1,10- phenanthroline)copper(I/II) ($[Cu(dtbp)]^{+/2+}$), and **(d)** bis(2,9-diphenyl-1,10-phenantroline)copper(I/II) ($[Cu(dpp)]^{+/2+}$).

Table 5. Reorganization energies (kJ/mol) of the oxidized (λ_{ox}) and reduced (λ_{red}) forms, and the total internal reorganization energies (λ_i) of the various copper complexes, along with the differences in dihedral angles between the two oxidation states.

Substituent at the 2,9 position	Copper complex	λ_{red} (kJ mol^{-1})	λ_{ox} (kJ mol^{-1})	λ_i (kJ mol^{-1})	Δ in dihedral angle (°)
Methyl (reference)	$[Cu(dmp)_2]^{+/2+}$	28.5	29.7	58.2	24
Butyl	$[Cu(dbp)_2]^{+/2+}$	20.1	20.7	40.8	14
Tert-butyl	$[Cu(tdbp)_2]^{+/2+}$	19.4	19.5	38.9	8
Phenyl	$[Cu(dpp)_2]^{+/2+}$	16.7	15.7	32.4	9

With DFT simulations indicating the phenyl-substituents at the 2-,9-position of the phenanthroline ligand to induce greatest reduction on the reorganization energy of the

formed copper complex (nearly half that of the reference complex, $Cu(dmp)_2$), only $Cu(dpp)_2$ was exhaustively studied from this point forward. For a more systematic study, attempts were made to synthesize all of the abovementioned copper complexes, however, $Cu(dbp)_2$ was difficult and $Cu(dtbp)_2$ impossible to achieve synthetically.

5.3.2 Synthesis and General Characterization

Synthesis of $[Cu(dpp)_2]$-complexes. The dpp ligand was synthesized through treatment of 1,10-phenanthroline with phenyllithium followed by rearomatization using MnO_2. Complexation of the dpp ligand was achieved with CuI, followed by a counterion exchange using an excess of LiTFSI to obtain $[Cu(dpp)_2](TFSI)$ as red crystals. $[Cu(dpp)_2](TFSI)_2$ was obtained by the oxidation of $[Cu(dpp)_2](TFSI)$ with $NOBF_4$, followed by counterion exchange using an excess of LiTFSI. The newly synthesized materials were verified via CHNS measurements.

Structure. Figure 63 shows the crystal structure of $[Cu(dpp)_2]^+$ as determined by single crystal XRD analysis of a $[Cu(dpp)_2](TFSI)$ crystal grown by slow ether diffusion into a MeCN solution of the complex. The structure shows two 2,9-diphenyl-1,10-phenantroline ligands coordinating to the Cu(I) metal center in a distorted tetragonal fashion. The structure obtained here is more flattened with respect to $[Cu(dmp)_2]^+$ due to the π- π interaction between the phenyl rings of each phenanthroline unit in the complex[254]. Single crystals of $[Cu(dpp)_2](TFSI)_2$ large enough for single crystal analysis could not be obtained for analysis.

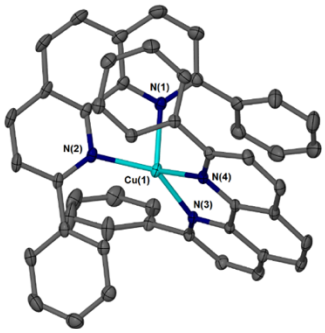

Figure 63. Spatial structure of the $[Cu(dpp)_2]^+$ cation as derived from single-crystal x-ray crystallography.

Solubility. In general, both $[Cu(dmp)_2]^{+/2+}$ and $[Cu(dpp)_2]^{+/2+}$ complexes were soluble in most of the common organic solvents such as MeCN, dichloromethane (DCM) and ethanol (EtOH) at high concentrations (maximum of 200 mM for Cu^{+} and 40mM for Cu^{2+}) as required for their application as redox mediators in liquid DSCs. These concentrations were found to be close to saturation. For $[Cu(dmp_2)](TFSI)_2$ in particular, a noticeable colour change occurs upon dissolution in MeCN—going from a purple solid to a green solution—indicative of a coordination of the MeCN solvent molecules to the Cu(II) centers. This colour change was not observed when dissolved in DCM, where it maintained a purple colour in solution due to the non-coordinating nature of DCM. Both $[Cu(dmp)_2]^{+/2+}$ and $[Cu(dpp)_2]^{+/2+}$ were found to have a low solubility in apolar solvents such as CBZ and toluene.

Energy Level. Evaluation of the energy levels of the copper complexes dissolved in MeCN solution were performed via cyclic voltammetry (CV). See section 2.2.2 for details. Briefly, CV measurements were done for 5 mM solutions of each copper complex in the presence of 0.1 M $TBAPF_6$ as a supporting electrolyte and measured at a scan rate of 100 mV s^{-1} in the voltage range of -0.05 V and 0.65 V where no ligand oxidations/reductions occur. The potentials were measured vs. $Ag/AgNO_3$. A ferrocenium/ferrocene (Fc^{+}/Fc) redox couple as an internal reference was used, and conversion to the NHE scale was done using $E_{1/2}(Fc) = 0.63$ V vs. NHE. As presented in Figure 64, the CVs show reversible waves corresponding to the Cu(II/I) redox reaction with $\Delta E_{p/p}$ values of ~ 85 mV and half-wave potentials of $E_{1/2} = 0.933$ V vs. NHE for $Cu(dmp)_2$ (correlating well with literature[129]), and $E_{1/2} = 0.932$ V for $Cu(dpp)_2$.

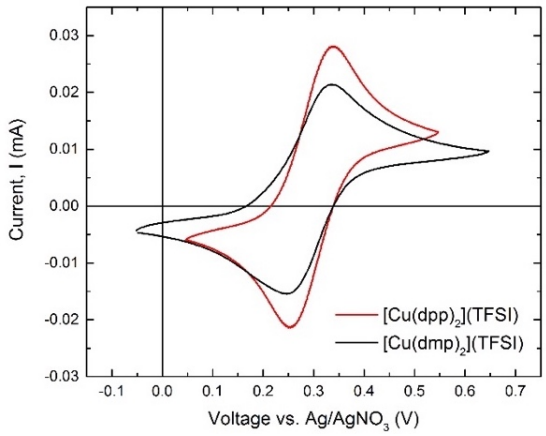

Figure 64. Cyclic voltammograms for $[Cu(dmp)_2]^+$ and $[Cu(dpp)_2]^+$ complexes (measured at a scan rate of 100 mV s^{-1} on 5 mM solutions of each complex in acetonitrile with 0.1 M $TBAPF_6$ as a supporting electrolyte under nitrogen.

Optical Absorption. As shown in Figure 65, spectra for MeCN-based solutions show molar extinction coefficients for $[Cu(dpp)_2]^+$ to be below 3500 $M^{-1}cm^{-1}$ throughout the entire visible spectrum of 350-800 nm, inferior to that of $[Cu(dmp)_2]^+$ and that of the organic dye Y123 (48,000 $M^{-1}cm^{-1}$ at 530 nm)[204]. This allows for a substantial fraction of the incident photons to be harvested by the Y123 dye molecules for charge generation as required. Absorption maxima for both Cu(I) complexes occur at λ_{max} = 440−460 nm, which is typical for Cu(I) and for which can be assigned to the metal-to-ligand charge transfer (MLCT) transitions, whilst the absorption signals in the UV region can be assigned to $\pi \rightarrow \pi^*$ transitions[118]. Broad absorption signals extending up to 1200 nm are observed for $[Cu(dpp)_2]^{2+}$ and $[Cu(dmp)_2]^{2+}$.

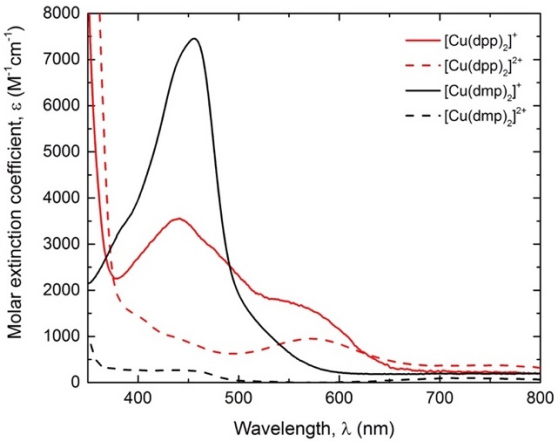

Figure 65. Molar extinction coefficients of 0.1 mM Cu(I) and 1 mM Cu(II) complexes in MeCN.

5.3.3 Electrolyte Conductivity and Charge Transfer at the CE

To evaluate the electrolyte conductivity as well as the charge-transfer resistance at the counter electrode, cyclic voltammetry of symmetrical devices was performed. The electrolyte solutions and counter electrodes used in symmetrical cells are identical to those previously reported[129] and for which are to be used in DSCs in section 5.3.5. The electrolytes contained 0.20 M Cu(I), 0.04 M Cu(II), 0.1M LiTFSI and 0.6 M 4-*tert*-butylpyridine (TBP) in MeCN (some excluding the TBP additive), and two electrodes

comprised of an electrodeposited PEDOT film on ITO (see section 2.1.4) which have been identified as excellent catalysts for copper complexes[255].

Current-voltage characteristics of symmetrical devices. Immediate comparison of the I–V curves measured in the absence and presence of TBP for $Cu(dmp)_2$ (Figure 66a) and $Cu(dpp)_2$ (Figure 66b) shows marked differences in the charge transport abilities of each complex. In the TBP-free electrolyte solutions, the complexes appear to exhibit slightly different charge transport ability. The cell resistance, R_{CV} which is a function of the electrolyte conductivity and overpotentials for electron transfer across the electrolyte/electrode interface, was approximated from the inverse of the slope around 0 V and was calculated to be ~37.7 Ohm cm^2 for $Cu(dpp)_2$, slightly lower than 41.5 Ohm cm^2 for $Cu(dmp)_2$. This is roughly four times greater than values previously reported in literature for $Cu(dmp)_2$[256], suggesting that the electrodes used in this study can be further improved. The limiting current densities, J_{lim}, at both forward and reverse bias for $Cu(dpp)_2$ (J_{lim} ~ 11.1 mA cm^{-2}) are lower than for $Cu(dmp)_2$ (J_{lim} ~12.9 mA cm^{-2}) indicative of its larger diffusion-limitation. When TBP is added, I–V curves become distorted and display peak currents that are nearly halved with respect to their TBP-free electrolytes, with values of 6.5 mA cm^{-2} for $Cu(dmp)_2$ and 5.5 mA cm^{-2} for $Cu(dpp)_2$ measured. The flattening of the curve around 0 V observed for $Cu(dpp)_2$ in particular suggests a problem with overpotential. Similar studies on the electrolyte conductivity of the well-established $Co(bpy)_3$ complex in the presence and absence of TBP shows the conductivity to remain largely unaffected by the presence of TBP[256]. Thus, an increase in the viscosity of the electrolyte is not likely a valid explanation for the heavily deteriorating effect TBP has on the conductivity of the copper complexes under investigation. An intuitive explanation for the observed behaviour would be that TBP is interacting with the copper complexes, hindering both the charge transport mobility and most likely charge transfer at the PEDOT counter electrodes. The effects of TBP are investigated further in sections 5.3.5 and 5.3.6.

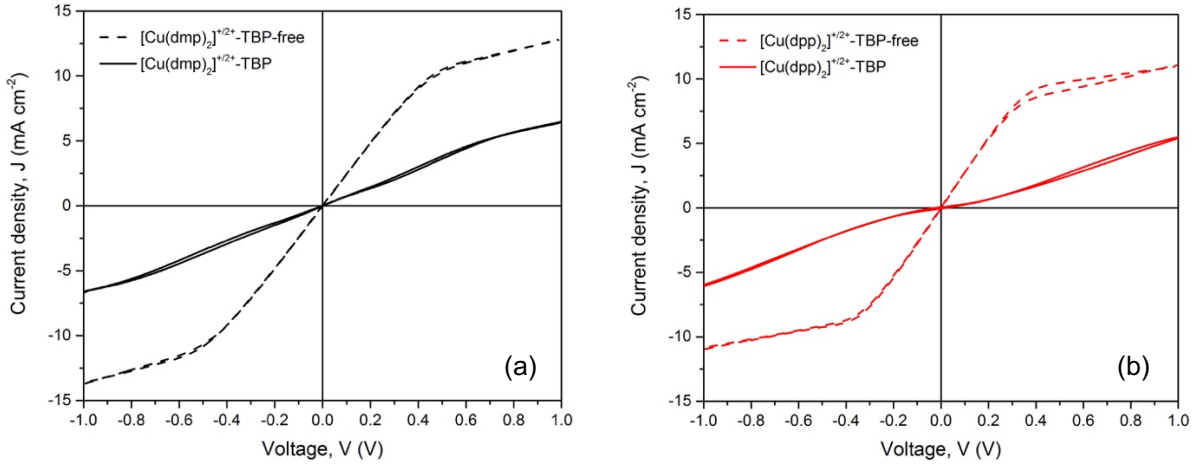

Figure 66. Cyclic voltammograms of symmetrical cells comprising of two PEDOT counter electrodes and an electrolyte solution containing **(a)** $[Cu(dmp)_2]^{+/2+}$ and **(b)** $[Cu(dpp)_2]^{+/2+}$ redox mediators, in the absence (dotted line) and presence (solid line) of TBP. The composition of electrolytes used was 0.2 M Cu(I), 0.04 M Cu(II), 0.1 M LiTFSI and 0.6 M TBP (where indicated).

5.3.4 Dye Regeneration Kinetics

It is proposed that by reducing the reorganization energy of the copper complex, dye regeneration becomes easier. To test that this is indeed the case, the rates of dye regeneration, k_{reg}, were investigated for both $[Cu(dmp)_2]^+$ and $[Cu(dpp)_2]^+$, where the latter is expected to be faster, based on the calculated reorganization energies. Having redox potentials that differed only 0.001 mV (see section 5.3.2) means that the driving force for dye regeneration for each complex is roughly the same, and the resulting regeneration rates to depend mainly upon the differences in reorganization energies between the copper complexes.

Experimental set-up. See section 2.2.5 for full experimental details. Briefly, sandwich-based devices for TAS measurements were fabricated using a Y123-sensitized TiO_2 film as the working electrode and a glass slide as a dummy counter electrode. An electrolyte solution containing the copper species of interest was filled in between via a vacuum backfilling technique. Using a 500 nm excitation with excitation intensity of 3 μJ cm^{-2}, the signal decay of the oxidized dye was monitored at 800 nm where the absorption was determined to be predominant (and where the ground state dye molecule and copper complexes do not absorb). The electrolytes contained 10 mM of the Cu(I) species of interest in MeCN in addition to the standard concentration of 0.1 M LiTFSI, and 0.6 M TBP

where indicated. The presence of Cu(II) was neglected since the Cu(I) species is responsible for dye regeneration. An inert electrolyte deficient of Cu(I) was also measured that would yield the recombination lifetime, k_{rec}, of injected electrons with that of the oxidized dye. Lifetimes were estimated from the half-life, $\tau_{1/2}$, time, i.e. when the initial optical density, OD_{t0}, decreases to half its value (i.e. $OD_{t0}/2 = OD(\tau_{1/2})$).

Transient absorption decay (TAD) results. Figure 67 shows the absorption signal decays for all electrolytes. The different profiles clearly show that the rate of the dye regeneration depends on the species present in solution. In the absence of Cu(I), the k_{rec} lifetime was determined to be 69.0 μs. In the presence of Cu(I), the k_{reg}'s of the dye was determined to be smaller for $[Cu(dpp)_2]^+$ (7.24 μs) than $[Cu(dmp)_2]^+$ (25.4 μs) in good correlation with its lower reorganization energy calculated from DFT calculations.

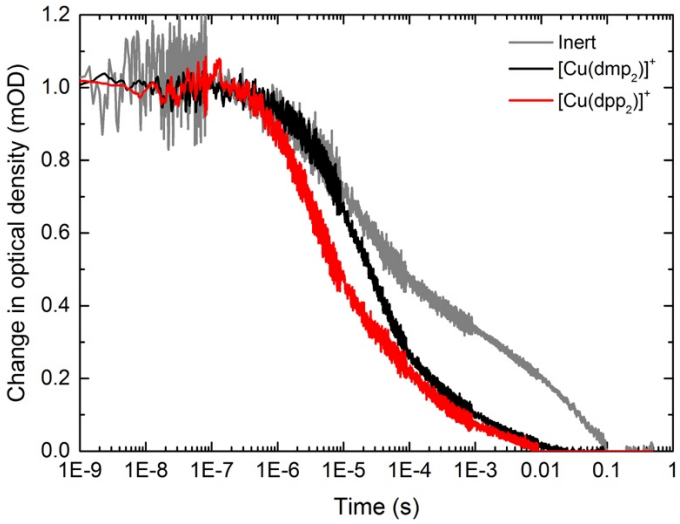

Figure 67. Nanosecond laser transient absorption spectroscopy measurements of Y123 on ~1μm thick TiO_2 films in contact with MeCN-based electrolytes containing $[Cu(dmp)_2]$TFSI (black) and $[Cu(dpp)_2]$TFSI (red) in the presence of the LiTFSI additive. An inert electrolyte containing LiTFSI only (grey) was also measured. Note that TBP was excluded in these measurements. An excitation wavelength of 500 nm and probe wavelength of 800 nm were used.

Table 6. Dye regeneration half lifetimes of the Y123 dye in contact with the copper complexes as extracted from the TAD spectra shown in Figure 67.

Redox Mediator	$\tau_{1/2}$ (μs)
Blank	69.0
$[Cu(dmp)_2]^+$	25.4
$[Cu(dpp)_2]^+$	7.24

5.3.5 Application as Redox Mediator in DSC

Energy level compatibility of components. The redox potentials derived for the complexes (see section 5.3.2) and the HOMO LUMO levels of the commercially available dye Y123[204] are shown in the energy level diagram (Figure 68). Energetic alignment of the redox potential of the complexes with that of the HOMO level of Y123 allows for dye regeneration with a driving force of ~140 mV, a value that has previously been reported to be sufficient for dye regeneration for such complexes[206,257]. As depicted, a high V_{OC} exceeding 1 V is expected for DSCs employing both copper complexes in combination with the Y123 dye as a result of the large energy gap between the quasi-Fermi level of TiO_2 and the redox potential of Cu(II/I) (a theoretical potential difference of $E_{Cu(L)} - E_{TiO_2} = 0.93 + 0.46 = 1.39$ V) together with the expected efficient interfacial charge transfer from Cu(I) to the oxidized dye.

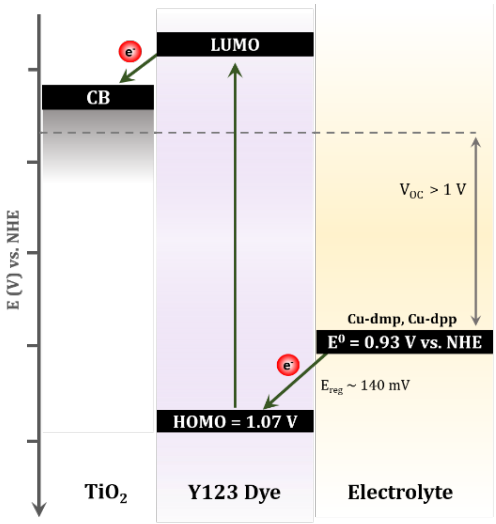

Figure 68. Energy level (vs. NHE) diagram of TiO_2, Y123 and the $[Cu(dmp)_2]^{+/2+}$ and $[Cu(dpp)_2]^{+/2+}$ redox couples.

Device fabrication. Hereby, all devices were fabricated with a ~8 µm mesoporous TiO_2 layer (5 µm of 30 nm TiO_2 particles + 3 µm of 400 nm TiO_2 particles), and were sensitized with the dye Y123 (see section 2.3.3 for details). The underlying blocking layer was deposited by a 3 x $TiCl_4$ treatment, which, through initial optimization tests, was found to be necessary in order to build pin-hole free blocking layers that eliminated excessive

recombination of electrons in the TCO with the Cu(II) species. The electrolytes were formulated following the same composition and concentrations as previously published for $Cu(dmp)_2$[257]. Given the deteriorating effect of TBP was found to have on the electrolyte conductivity (see section 5.3.3), Cu(II/I)-based electrolytes were also prepared in the absence of the TBP additive and tested for their performance in devices. Electrolytes comprised of 0.20 M Cu(I), 0.04 M Cu(II), 0.10 M LiTFSI and 0.6 M TBP in acetonitrile, with TBP omitted in some electrolyte solutions as indicated. PEDOT electrodeposited onto a ~1 μm thick mesoporous ITO film on an FTO substrate were used as counter electrodes due to better fill factors and overall performance compared to PEDOT electrodeposited onto bare FTO electrodes. This better performance can be attributed to its higher surface area that produces more catalytic active sites, thereby reducing the charge transfer resistance at the electrolyte/PEDOT-ITO interface[258], as well as the smaller separation between electrodes that increases electron collection efficiency[259].

Current-voltage characteristic of DSCs. Photovoltaic performance of the DSCs are shown in Figure 69 and the corresponding photovoltaic parameters tabulated in Table 7. Typical J–V curve were observed for TBP-containing electrolytes, whereas TBP-free electrolytes showed huge current and voltage limitations. For TBP-containing electrolytes (Figure 69a), devices employing the $Cu(dpp)_2$ reached an average efficiency of 3.31% (J_{SC} = 6.91 mA cm^{-2}, V_{OC} = 0.926V and FF = 51.8 %), approximately a third of what was measured with the $Cu(dmp)_2$ complex which reached an average efficiency of 9.80% (J_{SC} = 14.17 mA cm^{-2}, V_{OC} = 1.07 V and FF = 64.7 %). As expected, high V_{OC}'s ~ 1 V were attained in devices employing both copper complexes, attributed both to the large energy difference between the electrolyte redox potential and the TiO_2 quasi-Fermi level in combination with low recombination losses. However, evidently, devices made with $Cu(dpp)_2$ suffered from a significantly lower J_{SC}, less than half that measured for the $Cu(dmp)_2$ complex. The nonlinear relation between J_{SC} and light intensity for devices employing $Cu(dpp)_2$ (Figure 70) confirms the limitations in mass transport within the electrolyte, which is not the same case for $Cu(dmp)_2$, again, correlating well with literature[257], which can only partly explain the observed huge differences in

performance. Interestingly, devices employing TBP-free electrolyte solutions (Figure 69b) performed extremely poorly, with similar photocurrents of ~ 4 mA cm^{-2} measured for both complexes (~ 50% to 70% lower than their TBP-containing counterparts), and significant drops in V_{OC} (~35% lower), indicating significant recombination losses. Thus, despite the conductivity being hampered by the presence of TBP, here, it is evident that TBP is critical in order to achieve high-efficiency devices, increasing overall efficiencies by 6 times for $Cu(dmp)_2$ and nearly 3 times for $Cu(dpp)_2$. Dark current densities as high as 100 mA cm^{-2} were reached for TBP-free electrolytes—an order of magnitude higher than that measured for TBP-containing electrolytes—again, confirming the huge impact TBP has on the electrolyte conductivity as was observed in symmetrical cells. This is investigated further in section 5.3.6.

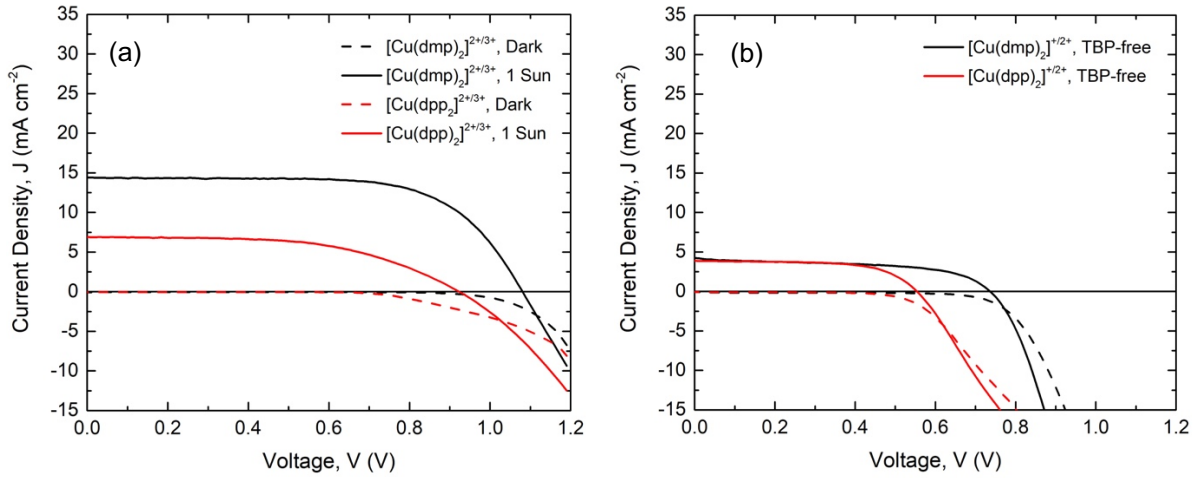

Figure 69. J-V curves for champion DSCs employing copper complexes as redox mediators in conjunction with the Y123 dye, measured under dark (dashed line) and standard AM1.5G irradiation (solid line). The electrolyte composition employed was 0.2 M Cu(I), 0.04M Cu(II), 0.1 M LiTFSI, with **(a)** 600 mM TBP and **(b)** 0 mM TBP.

Table 7. Best photovoltaic performance data for DSCs employing copper complexes as redox mediators in conjunction with the Y123 dye, measured under standard AM1.5G Irradiation. The electrolyte composition employed was 0.2 M Cu(I), 0.04M Cu(II), 0.1 M LiTFSI, in the absence and presence of TBP as indicated.

Redox Mediator	TBP [mM]	V_{OC} [V]	J_{SC} [mAcm^{-2}]	FF [%]	PCE [%]
$[Cu(dmp)_2]^{+/2+}$	0	0.727 ± 0.007	4.19 ± 0.06	54.4 ± 0.2	1.68 ± 0.03
	600	1.068 ± 0.018	14.17 ± 0.61	64.7 ± 1.9	9.80 ± 0.77, best: 10.4
$[Cu(dpp)_2]^{+/2+}$	0	0.575 ± 0.007	3.49 ± 0.12	57.0 ± 5.0	1.23 ± 0.13
	600	0.926 ± 0.007	6.91 ± 0.01	51.8 ± 3.9	3.31 ± 0.24, best: 3.5

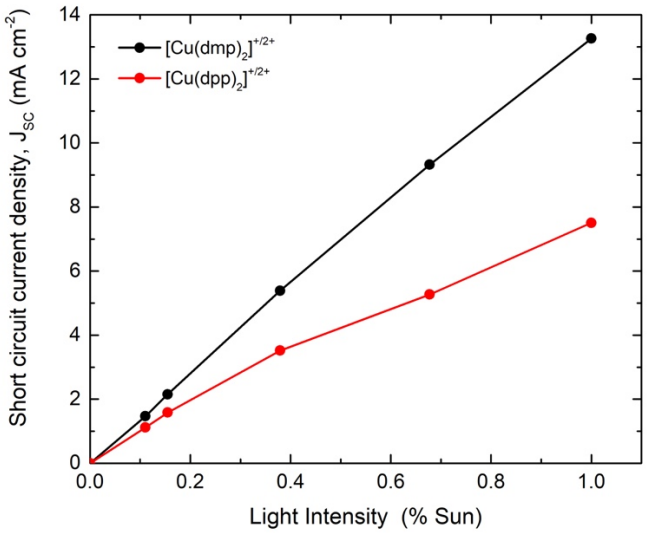

Figure 70. Short circuit current density vs. light intensity curves of best devices employing $[Cu(dmp)_2]^{+/2+}$ (black) and $[Cu(dpp)_2]^{+/2+}$ (red), both in the presence of TBP.

IPCE. For devices containing TBP, spectra shown in Figure 71 display wide spectral responses yielding maximum IPCE values between 55% and 65% in the range of 350 to 650 nm. Compared to traditionally employed cobalt complexes that attain IPCE values reaching 85%[260], maxima below this value can be attributed to quenching of photo-excited dye molecules and charge recombination (investigated further in sections 5.3.6.3 and 5.3.6.4), as well as optical losses by the relatively high extinction coefficient copper complexes employed here. In particular, the noticeable dip in the IPCE spectra for both complexes around 450 nm can be attributed to the peak light absorption by the Cu(I) species as evident from their UV-Vis absorption (see section 5.3.2). Interestingly, the J_{SC} calculated from the overlap integral of the IPCE for $Cu(dpp)_2$ (10.44 mA cm^{-2}) is more than twice that of what was measured in devices during J–V characterization under full sun illumination conditions. Moreover, in the absence of TBP, the IPCE measured for devices employing $Cu(dpp)_2$ is even higher (≈ 20%) than what was measured for the more efficient $Cu(dmp)_2$-based devices. Both shape (and magnitude) of IPCE in absence of TBP indicates significant problems with recombination. IPCE spectra were measured under low light intensities, and so differences in trends can be assumed to be a result of the diffusion limitation experienced by $Cu(dpp)_2$ under full light conditions (see Figure 70) in which charge transport is heavily hindered due to the significant amount of charge carriers that need to be transported across the electrolyte layer.

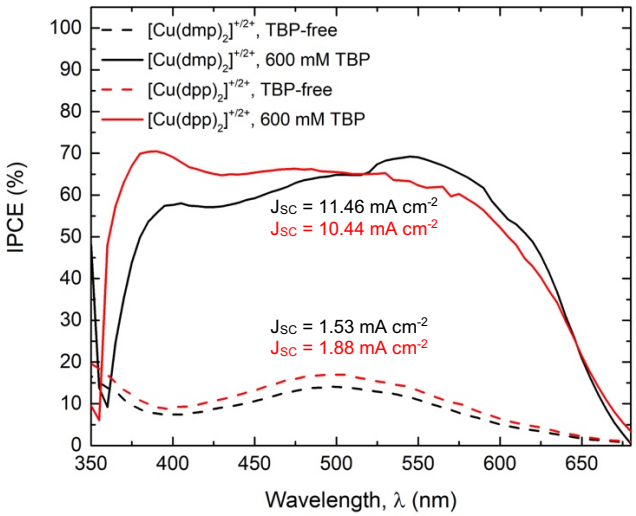

Figure 71. IPCE of best devices employing $[Cu(dmp)_2]^{+/2+}$ (black) and $[Cu(dpp)_2^{+/2+}$ (red), in the absence (dashed) and presence (solid) of the TBP additive.

5.3.6 Investigation of the Role of TBP

The role of TBP in iodide/tri-iodide and cobalt complex-based electrolytes has been thought to be well understood; (i) adsorbing onto bare TiO_2 surfaces to prevent recombination between injected electrons with that of the oxidized redox mediator, and (ii) raising the TiO_2 fermi level, leading to higher open circuit voltages and improved fill factors[44,45,47,261–263]. The use of TBP as an additive in electrolyte solutions for DSC applications has thus been indispensable, frequently incorporated in high concentrations to improve efficiencies in DSCs and reports of TBP-free devices (or alternatives to TBP) now very rare. However, initial symmetrical cell data obtained here (section 5.3.3) and previously reported electrochemical[262] and conductivity[256] studies, suggest an indisputable interaction between TBP and the copper complexes that affects its conductivity. Moreover, its presence and absence is the difference between working and poorly-working devices (section 5.3.5), indicating TBP to be playing a much more important role in copper complex-based electrolytes in DSCs than originally presumed. Here, a thorough investigation of the interactions between TBP and the copper complexes and dye is provided, along with an investigation of its effects on key recombination processes.

5.3.6.1 TBP interaction with Copper Complex

UV/Vis absorption spectroscopy. UV-Vis spectra of MeCN-based solutions comprising the copper complexes in the absence and presence of TBP (using the same molar ratios as that used in devices, i.e. Cu(I):TBP is 1:3 and Cu(II):TBP is 1:15) were measured and compared. No significant changes to the spectra of Cu(I) was observed with the addition of TBP (Figure 72a-d). Spectra of Cu(II), on the other hand, show significant changes with the addition of TBP (Figure 72e-h), giving a simple yet clear indication that TBP is interacting with the Cu(II) species in solution. For pristine $[Cu(dmp)_2]^{2+}$, absorption maxima appear at ~ 715, and 1010 nm (Figure 72e). When TBP is added, a shoulder appears at 450 nm which then eventuates to a peak after several days (Figure 72f). This peak is reminiscent of the one corresponding the $[Cu(dmp)_2]^{1+}$ complex, suggesting the reduction of $[Cu(dmp)_2]^{2+}$ to $[Cu(dmp)_2]^{1+}$ induced by the addition of TBP. Moreover, the absorption peaks in the higher wavelength region become slightly blue-shifted, indicative of a possible coordination occurring between TBP and the $[Cu(dmp)_2]^{2+}$ complex. Absorption spectra of the pristine $[Cu(dpp)_2]^{2+}$ solution shows distinct peaks at ~600 nm and ~790 nm (Figure 72g), which then undergo slight shifts and increasing variations in peak heights over several days—growth of the ~600 nm peak and dampening of the ~790 nm peak—upon the addition of TBP (Figure 72h). Again, these results point towards an interaction and possible coordination of TBP with $[Cu(dpp)_2]^{2+}$. To ensure that the observed changes over time are driven directly by the addition of TBP, the absorption spectra of all TBP-free solutions were also measured over time. Indeed, UV-Vis spectra of both pristine solutions of $[Cu(dmp)_2]^{2+}$and $[Cu(dpp)_2]^{2+}$ (as well as those of all Cu(I) solutions) show negligible change over time that indicate good stability in their initial states in the atmospheric conditions under which these measurements were conducted.

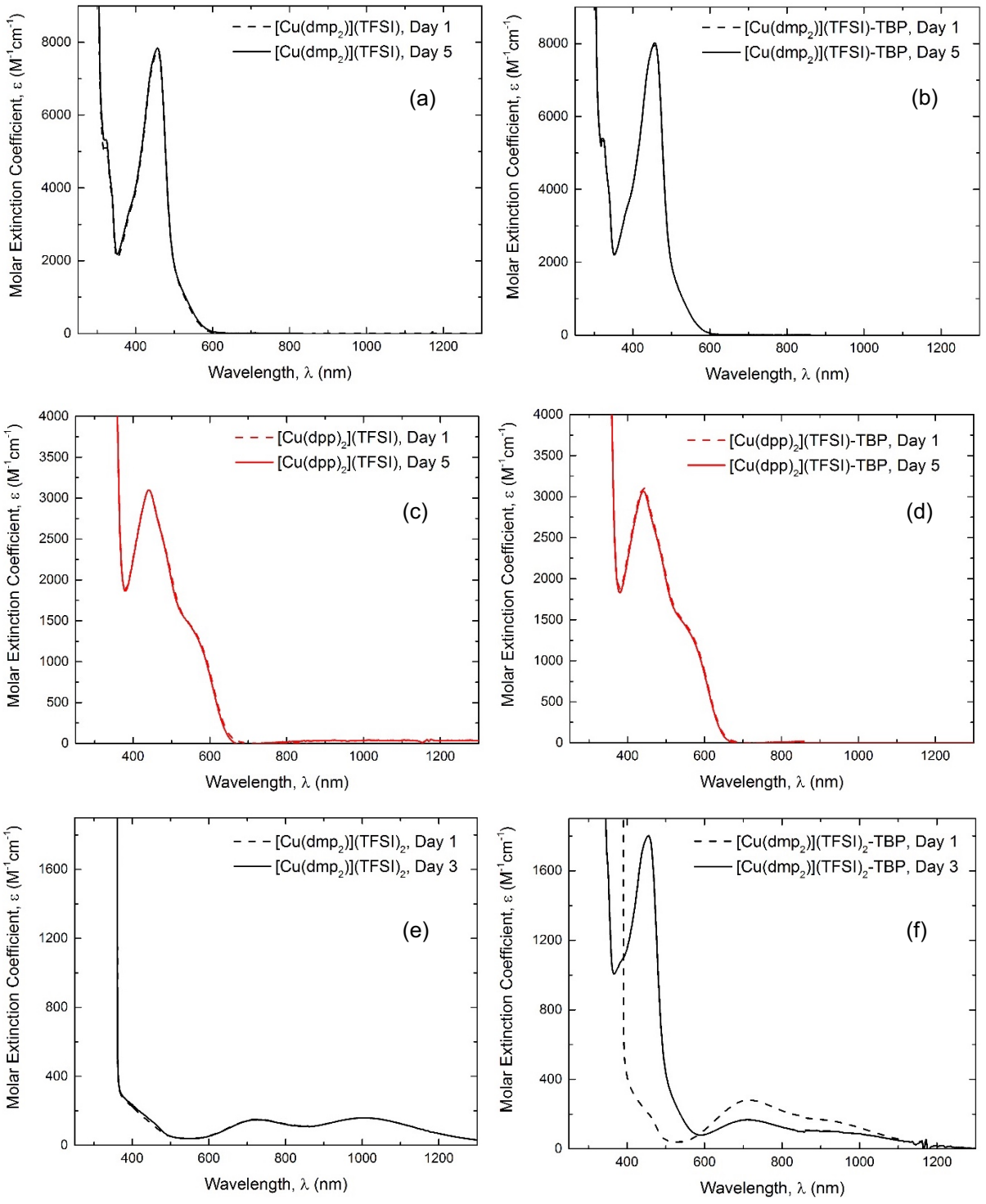
[Cu(dmp2)](TFSI), Day 1
[Cu(dmp2)](TFSI), Day 5
(a)
[Cu(dmp2)](TFSI)-TBP, Day 1
[Cu(dmp2)](TFSI)-TBP, Day 5
(b)
[Cu(dpp)2](TFSI), Day 1
[Cu(dpp)2](TFSI), Day 5
(c)
[Cu(dpp)2](TFSI)-TBP, Day 1
[Cu(dpp)2](TFSI)-TBP, Day 5
(d)
[Cu(dmp2)](TFSI)2, Day 1
[Cu(dmp2)](TFSI)2, Day 3
(e)
[Cu(dmp2)](TFSI)2-TBP, Day 1
[Cu(dmp2)](TFSI)2-TBP, Day 3
(f)
Molar Extinction Coefficient, ε (M-1cm-1)
Wavelength, λ (nm)

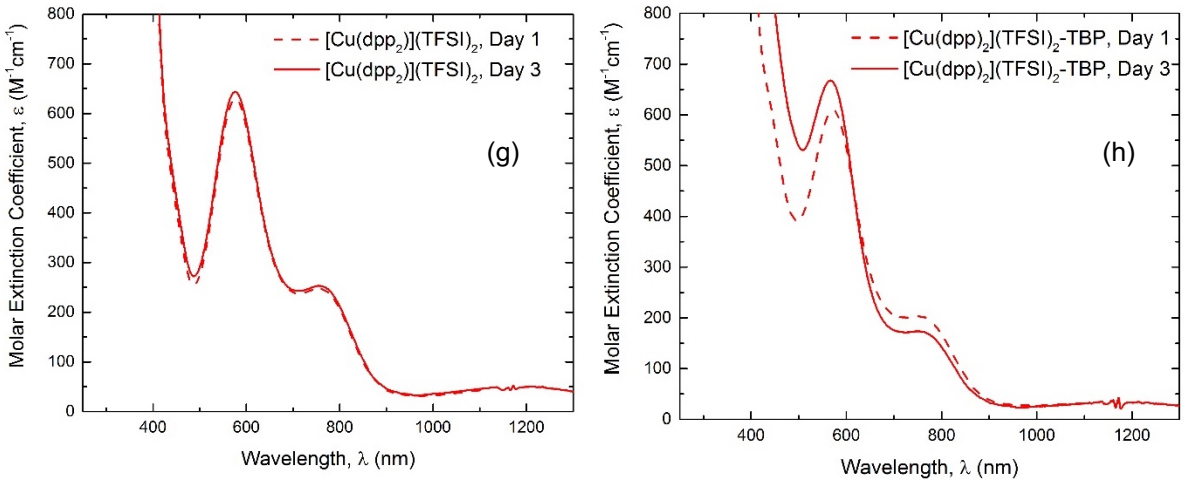

Figure 72. UV-Vis absorbance spectra of **(a)-(d)** 0.1 mM Cu(I) complexes and **(e)-(h)** 0.5 – 1.0 mM Cu(II) complexes, in the absence (left) and presence (right) of the TBP additive in MeCN.

UV/Vis titration experiments. The formation of a Cu(II)-TBP complex was further studied by UV/Vis titration experiments. However, in MeCN, peak separation was not very distinctive (compare Figure 72a&g with Figure 72f&h), and the possibility of competitive coordination of Cu(II) with MeCN solvent molecules rendered it to be an unsuitable solvent for this experiment. As such, titration experiments were conducted in the non-coordinating solvent, DCM. Starting with a pristine solution of the $[Cu(dmp)_2]^{2+}$ species in DCM, TBP was added in 0.1 eq. increments to a maximum of 1.1 eq. The resulting spectra are shown in Figure 73a. Here, increasing amounts of TBP resulted with a dampening of the peak at 530 nm and growth of the peak at 700 nm, and in between, a clear isospectic point at 640 nm is observed, confirming the coordination of $[Cu(dmp)_2]^{2+}$ with TBP. No colour change was observed upon excess addition of MeCN to the $[Cu(dmp)_2]^{2+}$-TBP DCM solution, indicating a stronger coordination with TBP with respect to MeCN. For $[Cu(dpp)_2]^{2+}$, it was found that the addition of TBP caused only very slow changes to the spectra with time. Thus, only 0.3 eq. of TBP was added and the spectra and measured over time. Here, an increase of the peak at 580 nm and dampening of the peak at 775 nm is observed (Figure 73b).Though the coordination is occurring at a much slower rate, it nonetheless confirms a weak interaction between the TBP and $[Cu(dpp)_2]^{2+}$ complex.

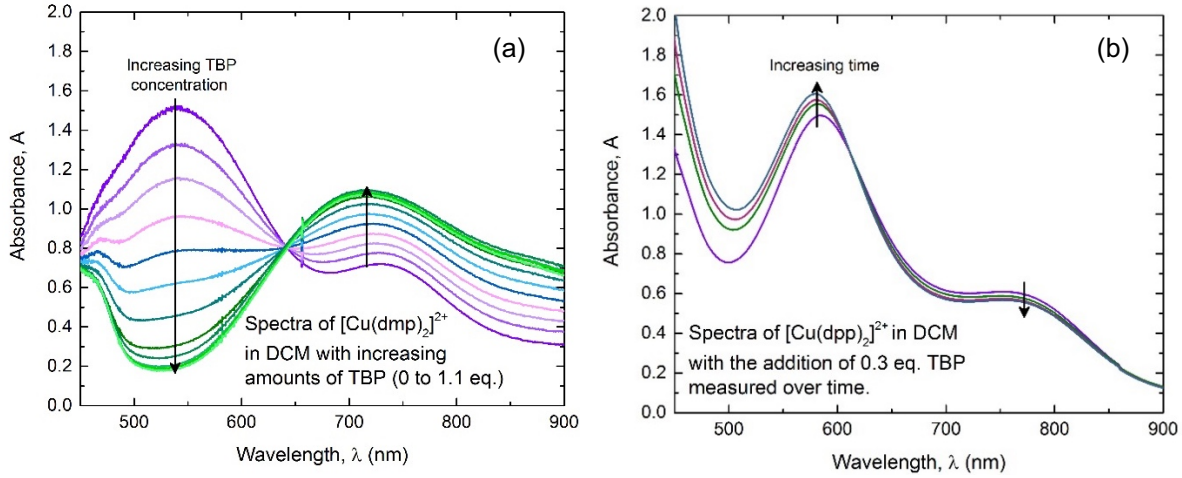

Figure 73. UV-Vis absorbance spectra of **(a)** $[Cu(dmp)_2](TFSI)_2$ with increasing amounts of TBP in DCM, and **(b)** $[Cu(dpp)_2](TFSI)_2$ with 0.3 eq. of TBP measured over ~1.5 hours.

Single crystal analysis. Crystals that were successfully grown by the slow diffusion of diethyl ether into a mixture of $[Cu(dmp)_2](TFSI)_2$ and TBP in MeCN and were analysed via single crystal analysis, providing further confirmation of the coordination of Cu(II) with TBP. The crystal structure (Figure 74) shows the TBP to coordinate to the $[Cu(dmp)_2]^{2+}$ center through the pyridine unit at the fifth coordination site. Unfortunately, crystals could not be grown from a mixture of $[Cu(dpp)_2](TFSI)_2$ and TBP.

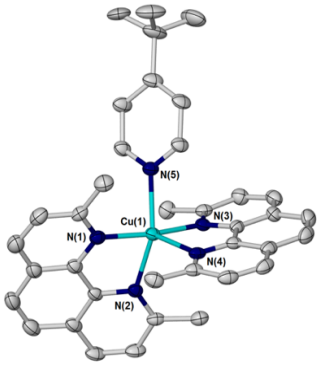

Figure 74. Spatial structure of the $[Cu(dmp)_2TBP]^{2+}$ cation as derived from single-crystal x-ray crystallography.

5.3.6.2 TBP interaction with Y123 dye

UV/Vis absorption spectroscopy. UV/Vis spectra were obtained for a Y123-sensitized electrode (TiO_2 of ~1 µm thickness), both with and without a TBP post-treatment. The

electrode was immersed into the same dye solution as used for DSC fabrication for ~1 hour only (minimizing the formation of aggregates), and the spectrum measured. A TBP post-treatment of the same electrode was done by immersion into a MeCN-based solution containing 600 mM TBP (the same concentration used in the electrolyte compositions used for DSC fabrication), and the resulting spectrum measured. As shown in the normalized absorption spectra (Figure 75), the post-treated films show a slight red shift, suggesting an interaction of TBP with the Y123 dye molecules. Further clues of an interaction of TBP with the dye is seen in section 5.3.6.4.

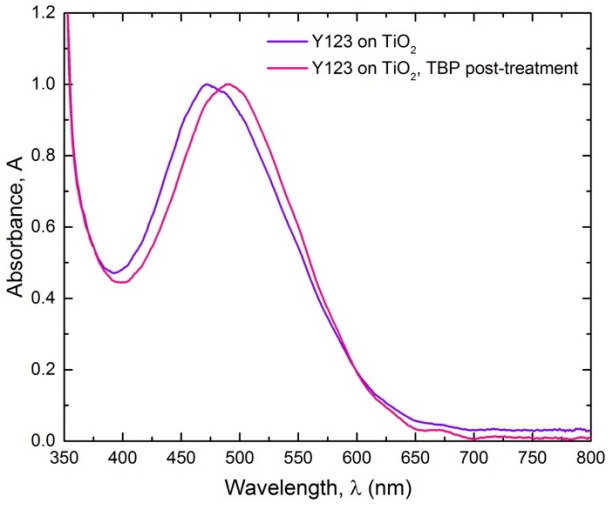

Figure 75. Normalized UV/Vis absorbance of Y123 adsorbed onto a ~1 µm thick TiO_2 film, without any post-treatment (purple) and with TBP post-treatment (pink).

5.3.6.3 Recombination of injected electrons with Cu(II)

When a photoexcited electron gets injected into TiO_2, the electron can diffuse through until it extracted at the TCO contact. The electron injection is extremely fast, orders of magnitude higher than the electron diffusion trough the TiO_2 itself due to the exponential density of trap states that slows down transport. As such, recombination of electrons in TiO_2 with holes in the redox species is a common culprit for poor performance, in particular, for lowering the FF[264]. Thus, to probe the recombination of electrons in TiO_2 with that of the redox species, electrochemical impedance spectroscopy (EIS) measurements of full devices was performed.

Electrochemical Impedance Spectroscopy. EIS of full devices were performed for both TBP-containing and TBP-free electrolytes and were measured at various applied voltages. The resultant nyquist plots were fitted to the model shown in section 2.4.4 to obtain the resistance values that are plotted in Figure 76. For both complexes, the diffusion resistance (R_{diff}) increases considerably in presence of TBP (Figure 76a), most likely a result of their interactions with TBP (see section 5.3.6.1) that slows down both mass diffusion and the rate of self-exchange reactions. $Cu(dpp)_2$, however, attains generally higher R_{diff} values than $Cu(dmp)_2$ (both with and without TBP), a trend in-line with its diffusion-limited behaviour observed in previous sections. Another plausible explanation for the faster diffusion behaviour of $[Cu(dmp)_2]^{2+}$ is its strong interaction with TBP, allowing TBP to be tightly bound to the complex and making the whole molecule-"sphere" smaller with respect to the $[Cu(dpp)_2]^{2+}$ (which can undergo a weak (constant) exchange with TBP). Recombination resistances (R_{rec}) could not be obtained for TBP-free electrolytes, as spectra were dominated by the charge transfer resistance at the counter electrode (R_{CE}). This is not a surprising result, due to the rapid charge transfer at the interface expected for low-reorganization energy complexes, and thus partially explaining their relatively poor device performance (section 5.3.5). Interestingly, R_{rec} for TBP-containing electrolytes (Figure 76b) was found to be very similar for each complex (particularly near V_{OC}) and therefore cannot account for the differences observed in device performances, suggesting that the diffusion resistance of the electrolyte is playing a dominant role.

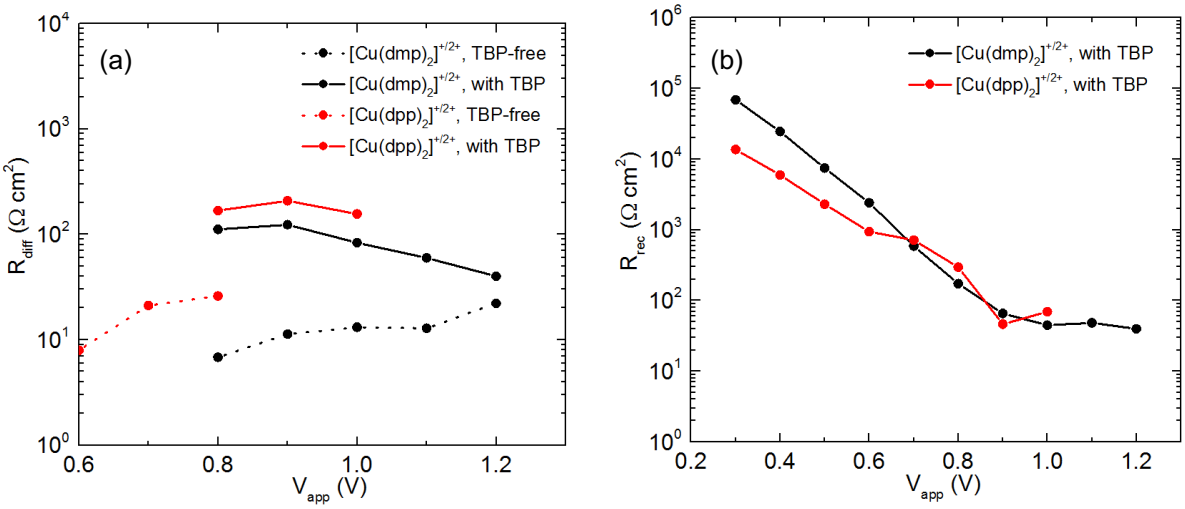

Figure 76. (a) Diffusion resistance (R_{diff}) and **(b)** recombination resistance (R_{rec}) for Y123-based DSCs employing $[Cu(dmp)_2]^{+/2+}$ (black) and $[Cu(dpp)_2]^{+/2+}$ (red) redox mediators in the presence (solid line) and absence (dotted line) of TBP, measured at various applied voltages.

5.3.6.4 Recombination of excited dye electrons with Cu(II)

In a DSC, quenching of an excited dye can occur via two main pathways; electron injection into the TiO_2, or, recombination with the Cu(II) species in the electrolyte, the former of which is often assumed to occur on a much faster time scale thus sustaining the function of the solar cell. In this section, recombination of excited dye electrons with the Cu(II) species in the electrolyte was considered as a potential loss mechanism. The interaction between the excited dye and the Cu(II) complexes in the absence and presence of TBP was investigated via steady-state and time-resolved fluorescence quenching experiments.

Steady-state fluorescence quenching of Y123 in solution. Fluorescence emission spectra were measured for solutions of Y123 (1 μM) in MeCN before and after the addition of ~1.25 eq. of the Cu(II) quencher solution of interest. Normalized emission spectra are shown for comparison in Figure 77. As can be seen, the addition of all investigated Cu(II) species result with a significant drop in the Y123 emission that are indicative of their strong quenching effects. For $[Cu(dpp)_2]^{2+}$-TBP and $[Cu(dpp)_2]^{2+}$, similar quenching effects are observed (~90% quenching efficiency), whilst $[Cu(dmp)_2]^{2+}$-TBP shows a significantly smaller quenching effect (~60%) compared to its TBP-free $[Cu(dmp)_2]^{2+}$ counterpart (~85%). One explanation could be the efficient blocking power that TBP has when tightly coordinating to $[Cu(dmp)_2]^{2+}$, which needs to be "released" before it is reduced to $[Cu(dmp)_2]^{+}$, thus preventing fast recombination reactions that would otherwise occur in the absence of TBP. These measurements suggest that considerable quenching of the dye is occurring by both complexes, and that the addition of TBP can partially contribute towards the 6 times enhancement of performance for devices employing $Cu(dmp)_2$.

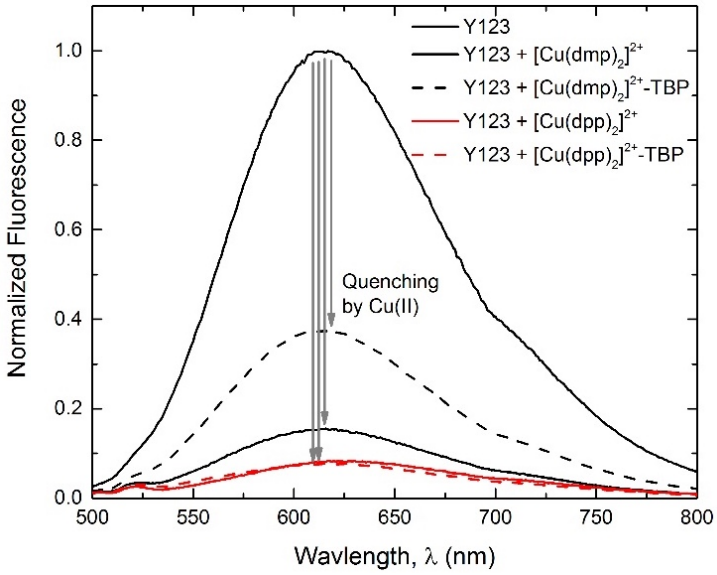

Figure 77. Steady-state emission spectra of Y123 with the addition of various Cu(II) quenchers in MeCN. Starting with a 10^{-6} M solution of Y123 in MeCN (the host species, grey bold line), ~1.25 eq. of $[Cu(dmp)_2](TFSI)_2$ (black) or $Cu(dpp)_2](TFSI)_2$ (red) was added, in the absence (solid line) and presence (~1.25 eq., dotted line) of TBP. Spectra were recorded at least three times each (spaced at least 1 minutes apart), to ensure an equilibrium state was reached. An excitation wavelenght of 450 nm was used.

Time-resolved fluorescence decay of Y123 adsorbed onto Al_2O_3. Time-resolved fluorescence measured using the TC-SPC method (Figure 78) was done to investigate the dye lifetime in contact with an electrolyte solution containing the Cu(II) species of interest, both in the presence and absence of the TBP. In order to replicate the conditions in an actual device as much as possible, measurements were conducted on Y123 adsorbed onto an inert Al_2O_3 surface immersed into an MeCN-based solution containing the quencher of interest. This would avoid any possible interaction between the anchoring cyanoacrylic groups of the dye molecules to the copper complexes themselves. Despite their rather unexpected similarities, the fluorescence decay curves confirm a decrease in lifetime in the presence of $[Cu(dmp)_2]^{2+}$ and $[Cu(dpp)_2]^{2+}$. Interestingly, the fluorescence data suggest that the presence of TBP alone is responsible for the prolonged lifetime of the dye. For $[Cu(dpp)_2]^{2+}$ in the presence of 1 eq. of TBP, a longer lifetime is observed due to the interaction of free (weakly bounded) TBP molecules with the dye. For $[Cu(dmp)_2]^{2+}$ in the presence of 1 eq. of TBP, the lifetime is only slightly increased since the TBP molecule is tightly bound to the Cu(II) centre. When increased to 15 eq., the presence of free TBP molecules in solution can interact with the dye and, in turn, slow

down the fluorescence decay rate. These results support previous data in which a TBP interaction with the dye is observed (section 5.3.6.2), but also highlights their ability to significantly slow down unfavourable dye relaxation.

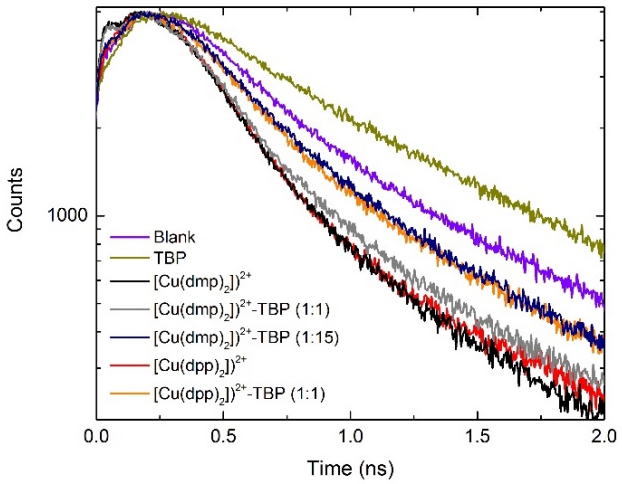

Figure 78. Fluoerscence decay of Y123 on Al_2O_3 immersed in MeCN-based solutions containing various Cu(II) quenchers in the abence and presence of TBP. Mesoporous Al_2O_3 films on microscopic glass slides (prepared by spin coating Al_2O_3 paste and heating at 450 ˚C for 30 minutes) were immersed into a 0.1 mM Y123 solution in dry MeCN overnight inside a glovebox. After dying, films were washed with MeCN, dried, and placed vertically into the cuvette filled with a 6 μM solution of the copper quencher in MeCN.

5.3.6.5 Alternative bases to TBP

Current-Voltage performance of Devices. Given the observations that TBP strongly interacts with the copper complexes in solution, devices were also made with a comparatively milder lewis base, p-trifluoromethylpyridine (TFMP), as well as that of 2-methylbenzimidazole (NMBI), and their performances examined in parallel to TBP (Figure 79a). Like TBP, these bases have been used previously as electrolyte additives in DSCs to block recombination[121,265]. Interestingly, devices worked well with the NMBI additive, but very poorly with the TFMP (Figure 79b).

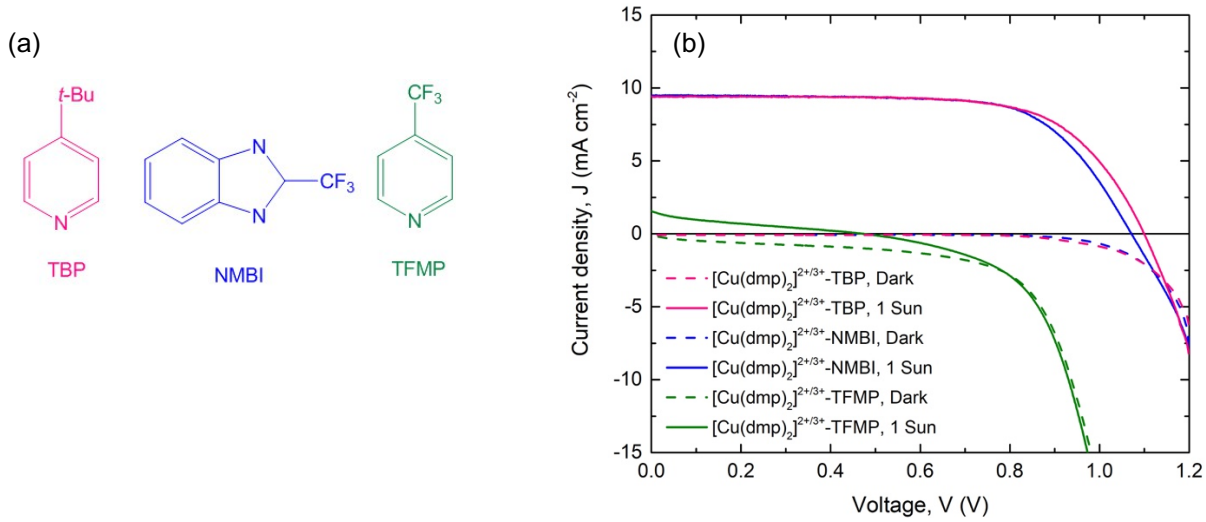

Figure 79. (a) Molecular structures of the various base additives, and **(b)** J–V of DSCs in the presence of TBP (pink), NMBI (blue) and TFMP (green) base additives.

Table 8. Best photovoltaic performance data for DSCs employing copper complexes as redox mediators with various base additives in conjunction with the Y123 dye, measured under standard AM1.5G irradiation. The electrolyte composition comprised of 0.2 M Cu(I), 0.04 M Cu(II), 0.1 M LiTFSI and 0.6 M of base as indicated.

Redox mediator	Base additive	V_{OC} [mV]	J_{SC} [mA cm^{-2}]	FF [%]	PCE [%]
$[Cu(dmp)_2]^{+/2+}$	TBP	1.11	9.66	68.08	7.28
	NMBI	1.07	9.49	68.48	6.96
	TFMP	0.47	1.57	19.48	0.15

UV/Vis spectra study of solutions. UV-Vis absorption spectra for $[Cu(dmp)_2]^{2+}$ and $[Cu(dpp)_2]^{2+}$ in DCM, with the addition of NMBI and TFMP were also attained (Figure 80). Like TBP, NMBI appears to interact with Cu(II). As for the TFMP base, there were no significant changes observed in the absorption spectra. Overall, these results correlate well with the trends observed in the device performances shown in Figure 79, where the interaction of $[Cu(dmp)_2]^{2+}$ with bases such as TBP and NMBI appears to be key in their ability to perform as a good redox mediator for application in devices.

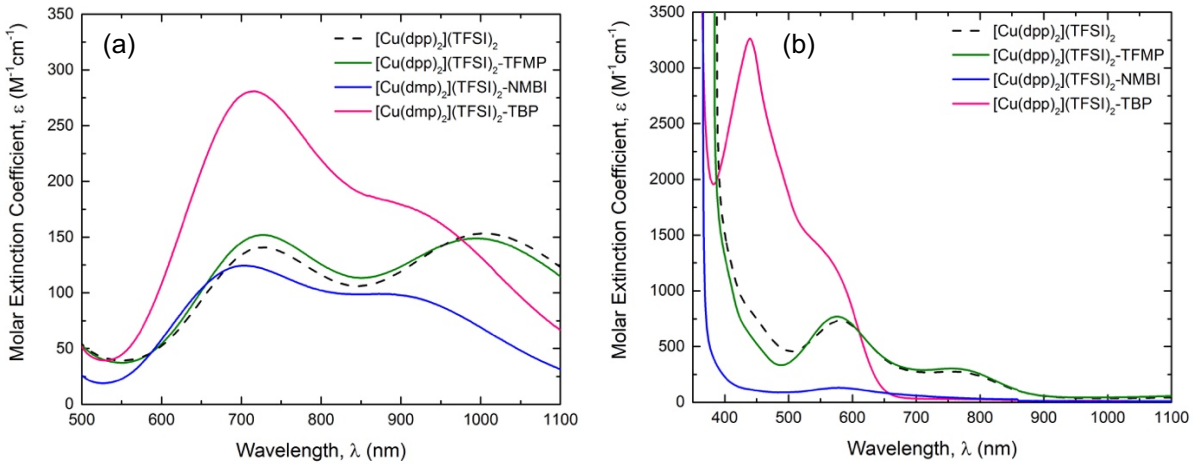

Figure 80. UV-Vis spectra of **(a)** $[Cu(dmp)_2](TFSI)_2$ and **(a)** $[Cu(dpp)_2](TFSI)_2$ complexes measured in DCM in the absence (black dotted) and presence of 1 eq. of TBP (pink), NMBI (blue) and TFMP (green) additives bases.

5.4 Summary and Conclusions

In conclusion, copper complexes based on phenanthroline ligands as redox mediators for DSCs were thoroughly investigated. DFT simulations showed that the use of bulky phenyl groups at the 2-,9- positions of the phenanthroline ligand to replace the methyl groups with respect to the reference complex ($[Cu(dmp)_2]^{+/2+}$) was effective at reducing the angular offset and lowering the overall reorganization energy by nearly 2 times. TAS measurements indeed confirmed faster dye regeneration kinetics exhibited by the newly developed $[Cu(dpp)_2]^{+}$ complex due to its lower reorganization energy, however, the performance of $[Cu(dpp)_2]^{+/2+}$ as a redox mediator in a DSC was still inferior to that of the reference complex. Moreover, the performance of both copper complexes as redox mediators in the absence of the common electrolyte additive, TBP, were significantly worse (up to 3 times for $Cu(dmp)_2$) despite the deteriorating effect TBP was found to have on their conductivity.

Simple UV/Vis studies suggested that an interaction between TBP and the Cu(II) species in the electrolyte solution can strongly influence recombination processes and can partially explain for significant differences in the performance between $Cu(dpp)_2$ and $Cu(dmp)_2$ in presence of TBP. It appears as though a strongly coordinating base to help block recombination with electrons in the excited dye is key to achieving high efficiencies. This was only realized for $[Cu(dmp)_2]^{2+}$, which was further confirmed by the employment of NMBI and TFMP as alternative base additives, the latter of which achieved a poor efficiency due to its lack of coordination.

Overall, the work presented in this chapter has highlighted an effective way in which to reduce the reorganization of copper complexes thereby improve charge transfer kinetics. Their implementation as solid-solid HTMs is identified as future work. Furthermore, the work presented has shed significant light into the different loss mechanisms occurring within DSCs employing copper complexes of low reorganization energy as redox mediators, with further studies required to elucidate the underlying mechanisms for the marked differences in performances observed in this study.

Chapter 6:

Conclusions and Future Outlook

Thin film solar cells based on dyes and perovskite as light absorbers receive significant attention within the scientific community due to their potential to meet future energy needs at low-cost. In an effort to push efficiencies higher and lower production costs, a significant amount of research within the field has been largely dedicated towards the development of new and improved materials in place of traditional material components. The research presented in this thesis contributes to the field of alternative solution-processible CTMs based on non-planar transition metal complexes.

Similar to their organic counterparts, transition metal complexes have almost unlimited variability of their chemical structure, providing ample opportunity for their solubility, morphology, conductivity, and energy levels to be fine-tuned to meet specific requirements. The transition metal complexes explored in this thesis were largely focused on those designed to attain a low energy activation barrier for charge transfer between its redox active centers. Two strategies were employed; in the first two research chapters, complexes of high denticity polypyridyl ligands were explored, and in the final research chapter, complexes of ligands featuring bulky substituents were explored.

In **Chapter 3**, the use of a high-denticity ligand was identified as a suitable ligand system to use for a Co(II/III) metal center, as this would provide a rigid structure that ensured both good stability (through the chelate effect) as well as a low activation energy for fast charge transfer and charge conduction via self-exchange. Film containing blends of Co(II) and Co(III) were characterized in terms of their electrical conductivity. The optimum blend, Co(bpyPY4)](OTf)$_{2.33}$, was found to be 8 orders greater with respect to its pristine Co(II) form, and 3 orders greater with respect to the conventional HTM, doped spiro-OMeTAD. Interestingly, Co(bpyPY4)](OTf)$_{2.33}$ films displayed a negative temperature coefficient of conductivity, in contrast to the Arrhenius semiconducting behaviour observed for pristine Co(II) films, doped spiro-OMeTAD, and molecular-based HTMs in general. While negative temperature coefficients are typically only observed for highly crystalline materials with extended planar π-systems or evidence of strong intermolecular coupling[266], a morphology analysis of the [Co(bpyPY4)](OTf)$_{2.33}$ films by GAXRD revealed some low short-range ordering and no evidence of long-range crystallinity, indicating it to be a unique transparent,

non-crystalline CTM in which thermally activated charge hopping does not appear to be the prevailing charge transport mechanism. Further studies are required to elucidate the unusual charge transport properties revealed in this work. When employed as a HTM in a ssDSC, respectable solar energy conversion efficiencies of 5.7% (with additives) and 3.23 % (without additives) were attained. Moreover, it was found to exhibit excellent pore-infiltration that enabled the use of a thick mesoporous scaffold, one of the major performance-limiting factors currently faced in ssDSCs. Overall, the work presented in this chapter has exposed the potential of transition metal complexes as solution processible HTMs for solid-state solar cells. Thus far, there are only two other examples of non-planar transition metal complexes have been successfully applied as HTMs in a ssDSCs[56,202].

In **Chapter 4**, a continuation of the exploration of a transition metal complex with a high-denticity ligand was undertaken. Here, a Fe(II/III) center was employed. Films composed of blends of Fe(II) and Fe(III) exhibited conductivities that were 3 orders higher than the pristine Fe(II) films and that of the benchmark 10% oxidized spiro-OMeTAD films. The resistivity behaviour for both pristine and mixed films displayed typical Arrhenius conductive behaviour, whilst electron microscopic images portrayed polycrystalline morphology. These finding are both in striking contrast to what was observed for the cobalt analogue, demonstrating the drastic changes to the properties of complex system upon changing a metal center. When applied as a HTM in a PSC that employed the wide band-gap $FAPbBr_3$ light absorber with a necessarily low-lying HOMO level, a power conversion efficiency of 2.0% (maximum of 2.2%) was obtained, whilst the spiro-OMeTAD HTM attained an power conversion efficiency of 4.9% (maximum of 5.2%). The open-circuit voltage of the PSCs employing the Fe-based HTM was lower than expected and inferior to the V_{OC} of the devices with a conventional organic spiro-OMeTAD HTM. While lower recombination resistance in the [Fe- (bpyPY4)](OTf)$_{2.5}$-based devices as compared to that in PSCs with the spiro-OMeTAD hole-transporting layer suggested charge recombination as a plausible explanation, extended studies on the origins of this phenomenon are identified as future work. The work present in this chapter has provided the first demonstration of the capacity of a transition metal complex to sustain efficient hole transport in an all-solid-state PSC via the redox activity of the metal center. Exclusion of performance-deteriorating additives

further highlights this a promising class of materials for further investigation as alternative HTMs.

In **Chapter 5**, copper complexes featuring phenanthroline ligands were explored as alternative redox mediators for DSCs that eliminate the complicated redox chemistry exhibited by the traditional iodide / triiodide redox couple, as well as the mass diffusion and large potential losses suffered by the use of cobalt complex-based redox mediators of high reorganization energy. DFT calculations suggested that the use of bulky phenyl substituents on the phenanthroline ligand ($[Cu(dpp)_2]^{2+/3+}$) in place of methyl groups as in the reference complex ($[Cu(dmp)_2]^{2+/3+}$) lowered the reorganization energy by almost two times. Indeed, TAS measurements confirmed faster dye regeneration kinetics of the newly designed $Cu(dpp)_2$ complex, however, improvements to the overall device efficiency were not attained. Furthermore, TBP was crucial in attaining the high efficiencies, despite t hugely deteriorating effect on the conductivity. Reasons for the poorer performance of $Cu(dpp)_2$ (3.5%) with respect to the reference complex (10.4%) is suspected to be attributed to its poor diffusion caused by the constant (weak) interactions with TBP molecules present in the electrolyte. $Cu(dmp)_2$ exhibited a strong interaction with TBP, which is believed to be effective at reducing unfavourable quenching of the excited dye. The work presented in this chapter has highlighted a plausible method in which to improve intermolecular charge transfer in copper complex-based systems, but also highlights the lack of understanding for such systems in their employment as redox mediators in DSCs. The work presented in chapter is expected to be published following further data collection and analysis that facilitates our understanding of the important role TBP plays in such copper complex-based electrolyte systems in DSCs.

Overall, the investigations presented in this thesis demonstrates the huge versatility and enormous potential of transition metal complexes as CTMs for their application in solar cells and other solution-processed electronic devices, an area that has not been fully exhausted.

References

1. Singh, P. B. R. & Singh, O. *Global Trends of Fossil Fuel Reserves and Climate Change in the 21st Century*. (2012). doi:10.13140/2.1.1079.8084
2. Houghton, J. *Global Warming: The Complete Briefing*. (Cambridge University Press, 2015).
3. the-Paris-Agreement @ Unfccc.Int.
4. Perez, R. & Perez, M. A Fundamental Look At Supply Side Energy Reserves For The Planet. *Int. Energy Agency SHC Program. Sol. Updat.* **62,** 4–6 (2015).
5. Haegel, N. M. *et al.* Terawatt-scale photovoltaics: Trajectories and challenges. *Science (80-.).* **356,** 141 LP-143 (2017).
6. www.fondriest.com.
7. NREL in Best Research Cell Efficiencies. Available at: https://www.nrel.gov/.
8. Saga, T. Advances in crystalline silicon solar cell technology for industrial mass production. *Npg Asia Mater.* **2,** 96 (2010).
9. O'Regan, B. & Grätzel, M. A low-cost, high-efficiency solar cell based on dye-sensitized colloidal TiO_2 films. *Nature* **353,** 737 (1991).
10. Bach, U. *et al.* Solid-state dye-sensitized mesoporous TiO_2 solar cells with high photon-to-electron conversion efficiencies. *Nature* **395,** 583 (1998).
11. Kojima, A., Teshima, K., Shirai, Y. & Miyasaka, T. Organometal halide perovskites as visible-light sensitizers for photovoltaic cells. *J. Am. Chem. Soc.* **131,** 6050–6051 (2009).
12. Cherepy, N. J., Smestad, G. P., Grätzel, M. & Zhang, J. Z. Ultrafast Electron Injection: Implications for a Photoelectrochemical Cell Utilizing an Anthocyanin Dye-Sensitized TiO_2 Nanocrystalline Electrode. *J. Phys. Chem. B* **101,** 9342–9351 (1997).
13. F Watson, D. & J Meyer, G. Electron injection at dye-sensitized semiconductor

electrodes. *Annual review of physical chemistry* **56,** (2005).

14. Bisquert, J. & Zaban, A. The trap-limited diffusivity of electrons in nanoporous semiconductor networks permeated with a conductive phase. *Appl. Phys. A* **77,** 507–514 (2003).

15. Hagfeldt, A. & Graetzel, M. Light-Induced Redox Reactions in Nanocrystalline Systems. *Chem. Rev.* **95,** 49–68 (1995).

16. Marcus, R. A. On the Theory of Oxidation-Reduction Reactions Involving Electron Transfer. I. *J. Chem. Phys.* **24,** 966–978 (1956).

17. Nissfolk, J., Fredin, K., Hagfeldt, A. & Boschloo, G. Recombination and Transport Processes in Dye-Sensitized Solar Cells Investigated under Working Conditions. *J. Phys. Chem. B* **110,** 17715–17718 (2006).

18. Kakiage, K. *et al.* Highly-efficient dye-sensitized solar cells with collaborative sensitization by silyl-anchor and carboxy-anchor dyes. *Chem. Commun.* **51,** 15894–15897 (2015).

19. Cao, Y., Liu, Y., Zakeeruddin, S. M., Hagfeldt, A. & Grätzel, M. Direct Contact of Selective Charge Extraction Layers Enables High-Efficiency Molecular Photovoltaics. *Joule* **2,** 1108–1117 (2018).

20. Listorti, A., O'Regan, B. & Durrant, J. R. Electron Transfer Dynamics in Dye-Sensitized Solar Cells. *Chem. Mater.* **23,** 3381–3399 (2011).

21. Aghazada, S. & Nazeeruddin, M. Ruthenium Complexes as Sensitizers in Dye-Sensitized Solar Cells. *Inorganics* **6,** 52 (2018).

22. Higashino, T. & Imahori, H. Porphyrins as excellent dyes for dye-sensitized solar cells: recent developments and insights. *Dalt. Trans.* **44,** 448–463 (2015).

23. Ragoussi, M.-E., Ince, M. & Torres, T. Recent Advances in Phthalocyanine-Based Sensitizers for Dye-Sensitized Solar Cells. *European J. Org. Chem.* **2013,** 6475–6489 (2013).

24. Qin, C., Wong, W.-Y. & Han, L. Squaraine Dyes for Dye-Sensitized Solar Cells: Recent Advances and Future Challenges. *Chem. – An Asian J.* **8,** 1706–1719 (2013).

25. Lee, C.-P. *et al.* Recent progress in organic sensitizers for dye-sensitized solar cells. *RSC Adv.* **5,** 23810–23825 (2015).

26. Nguyen, W. H. *et al.* Molecular Engineering of Organic Dyes for Improved Recombination Lifetime in Solid-State Dye-Sensitized Solar Cells. *Chem. Mater.* **25,** 1519–1525 (2013).

27. Kroeze, J. E. *et al.* Alkyl Chain Barriers for Kinetic Optimization in Dye-Sensitized Solar Cells. *J. Am. Chem. Soc.* **128,** 16376–16383 (2006).

28. Yao, Z. *et al.* Donor/Acceptor Indenoperylene Dye for Highly Efficient Organic Dye-Sensitized Solar Cells. *J. Am. Chem. Soc.* **137,** 3799–3802 (2015).

29. Pagliaro, M., Palmisano, G., Ciriminna, R. & Loddo, V. Nanochemistry aspects of titania in dye-sensitized solar cells. *Energy Environ. Sci.* **2,** 838–844 (2009).

30. Chen, D. *et al.* Synthesis of Monodisperse Mesoporous Titania Beads with Controllable Diameter, High Surface Areas, and Variable Pore Diameters (14–23 nm). *J. Am. Chem. Soc.* **132,** 4438–4444 (2010).

31. Chen, X. & Mao, S. S. Titanium Dioxide Nanomaterials: Synthesis, Properties, Modifications, and Applications. *Chem. Rev.* **107,** 2891–2959 (2007).

32. Koo, H.-J. *et al.* Size-dependent scattering efficiency in dye-sensitized solar cell. *Inorganica Chim. Acta* **361,** 677–683 (2008).

33. Kang, S. H. *et al.* Influence of light scattering particles in the TiO_2 photoelectrode for solid-state dye-sensitized solar cell. *J. Photochem. Photobiol. A Chem.* **200,** 294–300 (2008).

34. Hore, S., Vetter, C., Kern, R., Smit, H. & Hinsch, A. Influence of scattering layers on efficiency of dye-sensitized solar cells. *Sol. Energy Mater. Sol. Cells* **90,** 1176–1188 (2006).

35. Cameron, P. J. & and Laurence M. Peter. Characterization of Titanium Dioxide Blocking Layers in Dye-Sensitized Nanocrystalline Solar Cells. *J. Phys. Chem. B* **107,** 14394–14400 (2003).

36. Kavan, L., O'Regan, B., Kay, A. & Grätzel, M. Preparation of TiO_2 (anatase) films on

electrodes by anodic oxidative hydrolysis of TiCl3. *J. Electroanal. Chem.* **346,** 291–307 (1993).

37. Choi, H. *et al.* The effect of TiCl4-treated TiO_2 compact layer on the performance of dye-sensitized solar cell. *Curr. Appl. Phys.* **12,** 737–741 (2012).

38. Yin, H. *et al.* Novel synthesis of phase-pure nano-particulate anatase and rutile TiO_2 using TiCl4 aqueous solutions. *J. Mater. Chem.* **12,** 378–383 (2002).

39. Marchioro, A., Dualeh, A., Punzi, A., Grätzel, M. & Moser, J.-E. Effect of Posttreatment of Titania Mesoscopic Films by TiCl4 in Solid-State Dye-Sensitized Solar Cells: A Time-Resolved Spectroscopy Study. *J. Phys. Chem. C* **116,** 26721–26727 (2012).

40. Lee, S.-W., Ahn, K.-S., Zhu, K., Neale, N. R. & Frank, A. J. Effects of TiCl4 Treatment of Nanoporous TiO_2 Films on Morphology, Light Harvesting, and Charge-Carrier Dynamics in Dye-Sensitized Solar Cells. *J. Phys. Chem. C* **116,** 21285–21290 (2012).

41. Boschloo, G. & Hagfeldt, A. Characteristics of the Iodide/Triiodide Redox Mediator in Dye-Sensitized Solar Cells. *Acc. Chem. Res.* **42,** 1819–1826 (2009).

42. Howie, W. H., Harris, J. E., Jennings, J. R. & Peter, L. M. Solid-state dye-sensitized solar cells based on spiro-MeOTAD. *Sol. Energy Mater. Sol. Cells* **91,** 424–426 (2007).

43. Krüger, J. *et al.* High efficiency solid-state photovoltaic device due to inhibition of interface charge recombination. *Appl. Phys. Lett.* **79,** 2085–2087 (2001).

44. Yin, X. *et al.* The effects of pyridine derivative additives on interface processes at nanocrystalline TiO_2 thin film in dye-sensitized solar cells. *Surf. Interface Anal.* **39,** 809–816 (2007).

45. Huang, S. Y., Schlichthörl, G., Nozik, A. J., Grätzel, M. & Frank, A. J. Charge Recombination in Dye-Sensitized Nanocrystalline TiO_2 Solar Cells. *J. Phys. Chem. B* **101,** 2576–2582 (1997).

46. Boschloo, G., Häggman, L. & Hagfeldt, A. Quantification of the Effect of 4-tert-Butylpyridine Addition to I-/I3- Redox Electrolytes in Dye-Sensitized Nanostructured TiO_2 Solar Cells. *J. Phys. Chem. B* **110,** 13144–13150 (2006).

47. Han, S. Z. and M. Y. and X. Y. and L. Effect of 4- tert -Butylpyridine on the Quasi-Fermi

Level of Dye-Sensitized TiO 2 Films. *Appl. Phys. Express* **4,** 42301 (2011).

48. Kashif, M. K. *et al.* Stable dye-sensitized solar cell electrolytes based on cobalt(ii)/(iii) complexes of a hexadentate pyridyl ligand. *Angew. Chemie - Int. Ed.* **52,** 5527–5531 (2013).

49. Daeneke, T. *et al.* High-efficiency dye-sensitized solar cells with ferrocene-based electrolytes. *Nat. Chem.* **3,** 213–217 (2011).

50. Nakade, S., Kambe, S., Kitamura, T., Wada, Y. & Yanagida, S. Effects of Lithium Ion Density on Electron Transport in Nanoporous TiO_2 Electrodes. *J. Phys. Chem. B* **105,** 9150–9152 (2001).

51. Koops, S. E., O'Regan, B. C., Barnes, P. R. F. & Durrant, J. R. Parameters Influencing the Efficiency of Electron Injection in Dye-Sensitized Solar Cells. *J. Am. Chem. Soc.* **131,** 4808–4818 (2009).

52. Jennings, J. R. & Wang, Q. Influence of Lithium Ion Concentration on Electron Injection, Transport, and Recombination in Dye-Sensitized Solar Cells. *J. Phys. Chem. C* **114,** 1715–1724 (2010).

53. Thomas, S. *et al.* A review on counter electrode materials in dye-sensitized solar cells. *J. Mater. Chem. A* **2,** 4474–4490 (2014).

54. Li, Y., Li, H., Zhong, C., Sini, G. & Brédas, J.-L. Characterization of intrinsic hole transport in single-crystal spiro-OMeTAD. *npj Flex. Electron.* **1,** 2 (2017).

55. Xu, B. *et al.* 1,1,2,2-Tetrachloroethane (TeCA) as a Solvent Additive for Organic Hole Transport Materials and Its Application in Highly Efficient Solid-State Dye-Sensitized Solar Cells. *Adv. Energy Mater.* **5,** 1402340 (2015).

56. Luo, J. *et al.* 11% efficiency solid-state dye-sensitized solar cells with copper(II/I) hole transport materials. 1–8 (2017). doi:10.1038/ncomms15390

57. Hawash, Z., Ono, L. K. & Qi, Y. Moisture and Oxygen Enhance Conductivity of LiTFSI-Doped Spiro-MeOTAD Hole Transport Layer in Perovskite Solar Cells. *Adv. Mater. Interfaces* **3,** 1600117 (2016).

58. Snaith, H. J., Zakeeruddin, S. M., Schmidt-Mende, L., Klein, C. & Grätzel, M. Ion-

Coordinating Sensitizer in Solid-State Hybrid Solar Cells. *Angew. Chemie Int. Ed.* **44,** 6413–6417 (2005).

59. John, M.-K. *et al.* The Effect of Hole Transport Material Pore Filling on Photovoltaic Performance in Solid-State Dye-Sensitized Solar Cells. *Adv. Energy Mater.* **1,** 407–414 (2011).

60. Fabregat-Santiago, F. *et al.* Electron Transport and Recombination in Solid-State Dye Solar Cell with Spiro-OMeTAD as Hole Conductor. *J. Am. Chem. Soc.* **131,** 558–562 (2009).

61. I-Kang, D. *et al.* Pore-Filling of Spiro-OMeTAD in Solid-State Dye Sensitized Solar Cells: Quantification, Mechanism, and Consequences for Device Performance. *Adv. Funct. Mater.* **19,** 2431–2436 (2009).

62. Snaith, H. J. *et al.* Charge collection and pore filling in solid-state dye-sensitized solar cells. *Nanotechnology* **19,** (2008).

63. Melas-Kyriazi, J. *et al.* The Effect of Hole Transport Material Pore Filling on Photovoltaic Performance in Solid-State Dye-Sensitized Solar Cells. *Adv. Energy Mater.* **1,** 407–414 (2011).

64. Bach, U., De Cloedt, K., Spreitzer, H. & Grätzel, M. Characterization of Hole Transport in a New Class of Spiro-Linked Oligotriphenylamine Compounds. *Adv. Mater.* **12,** 1060–1063 (2000).

65. Kojima, A., Teshima, K., Shirai, Y. & Miyasaka, T. Organometal Halide Perovskites as Visible-Light Sensitizers for Photovoltaic Cells. *J. Am. Chem. Soc.* **131,** 6050–6051 (2009).

66. Yang, W. S. *et al.* Iodide management in formamidinium-lead-halide–based perovskite layers for efficient solar cells. *Science (80-.).* **356,** 1376 LP-1379 (2017).

67. Assadi, M. K., Bakhoda, S., Saidur, R. & Hanaei, H. Recent progress in perovskite solar cells. *Renew. Sustain. Energy Rev.* **81,** 2812–2822 (2018).

68. Albero, J., Asiri, A. M. & García, H. Influence of the composition of hybrid perovskites on their performance in solar cells. *J. Mater. Chem. A* **4,** 4353–4364 (2016).

69. Slimi, B. *et al.* Perovskite FA1-xMAxPbI3 for Solar Cells: Films Formation and Properties. *Energy Procedia* **102,** 87–95 (2016).

70. Upadhyaya, A., Negi, C. M. S., Yadav, A., Gupta, S. K. & Verma, A. S. Synthesis and Characterization of Methylammonium Lead Iodide Perovskite and its Application in Planar Hetero-junction Devices. *Semicond. Sci. Technol.* **33,** (2018).

71. White, T. P., Lal, N. N. & Catchpole, K. R. Tandem Solar Cells Based on High-Efficiency c-Si Bottom Cells: Top Cell Requirements for >30% Efficiency. *IEEE J. Photovoltaics* **4,** 208–214 (2014).

72. Lee, M. M., Teuscher, J., Miyasaka, T., Murakami, T. N. & Snaith, H. J. Efficient Hybrid Solar Cells Based on Meso-Superstructured Organometal Halide Perovskites. *Science (80-.).* **338,** 643 LP-647 (2012).

73. Ball, J. M., Lee, M. M., Hey, A. & Snaith, H. J. Low-temperature processed meso-superstructured to thin-film perovskite solar cells. *Energy Environ. Sci.* **6,** 1739–1743 (2013).

74. Stranks, S. D. *et al.* Electron-Hole Diffusion Lengths Exceeding 1 Micrometer in an Organometal Trihalide Perovskite Absorber. *Science (80-.).* **342,** 341 LP-344 (2013).

75. Stranks, S. D. *et al.* Electron-Hole Diffusion Lengths Exceeding 1 Micrometer in an Organometal Trihalide Perovskite Absorber. *Science (80-.).* **342,** 341 LP-344 (2013).

76. Umari, P., Mosconi, E. & De Angelis, F. Infrared Dielectric Screening Determines the Low Exciton Binding Energy of Metal-Halide Perovskites. *J. Phys. Chem. Lett.* **9,** 620–627 (2018).

77. Yucheng, L. *et al.* Two-Inch-Sized Perovskite CH3NH3PbX3 (X = Cl, Br, I) Crystals: Growth and Characterization. *Adv. Mater.* **27,** 5176–5183 (2015).

78. Li, W. *et al.* Enhanced UV-light stability of planar heterojunction perovskite solar cells with caesium bromide interface modification. *Energy Environ. Sci.* **9,** 490–498 (2016).

79. Yi, C. *et al.* Entropic stabilization of mixed A-cation ABX3 metal halide perovskites for high performance perovskite solar cells. *Energy Environ. Sci.* **9,** 656–662 (2016).

80. Bi, D. *et al.* Efficient luminescent solar cells based on tailored mixed-cation perovskites. *Sci. Adv.* **2,** (2016).

81. Ball, J. M., Lee, M. M., Hey, A. & Snaith, H. J. Low-temperature processed meso-superstructured to thin-film perovskite solar cells. *Energy Environ. Sci.* **6,** 1739–1743 (2013).

82. Etgar, L. *et al.* Mesoscopic CH3NH3PbI3/TiO_2 Heterojunction Solar Cells. *J. Am. Chem. Soc.* **134,** 17396–17399 (2012).

83. Liu, M., Johnston, M. B. & Snaith, H. J. Efficient planar heterojunction perovskite solar cells by vapour deposition. *Nature* **501,** 395 (2013).

84. Eperon, G. E., Burlakov, V. M., Docampo, P., Goriely, A. & Snaith, H. J. Morphological control for high performance, solution-processed planar heterojunction perovskite solar cells. *Adv. Funct. Mater.* **24,** 151–157 (2014).

85. Calió, L., Kazim, S., Grätzel, M. & Ahmad, S. Hole-Transport Materials for Perovskite Solar Cells. *Angew. Chemie Int. Ed.* **55,** 14522–14545 (2016).

86. Yin, W. J., Shi, T. & Yan, Y. Unique properties of halide perovskites as possible origins of the superior solar cell performance. *Adv. Mater.* **26,** 4653–4658 (2014).

87. Ryu, S. *et al.* Voltage Output of Efficient Perovskite Solar Cells with high Open-Circuit Voltage and Fill Factor. *Energy Environ. Sci.* **7,** 2614–2618 (2014).

88. Ye, S. *et al.* CuSCN-Based Inverted Planar Perovskite Solar Cell with an Average PCE of 15.6%. *Nano Lett.* **15,** 3723–3728 (2015).

89. Gagliardi, A. & Abate, A. Mesoporous Electron-Selective Contacts Enhance the Tolerance to Interfacial Ion Accumulation in Perovskite Solar Cells. *ACS Energy Lett.* **3,** 163–169 (2018).

90. Zhu, Z. *et al.* Mesoporous SnO2 single crystals as an effective electron collector for perovskite solar cells. *Phys. Chem. Chem. Phys.* **17,** 18265–18268 (2015).

91. Dobrovolsky, A., Merdasa, A., Unger, E. L., Yartsev, A. & Scheblykin, I. G. Defect-induced local variation of crystal phase transition temperature in metal-halide perovskites. *Nat. Commun.* **8,** 34 (2017).

92. Salim, T. *et al.* Perovskite-based solar cells: impact of morphology and device architecture on device performance. *J. Mater. Chem. A* **3,** 8943–8969 (2015).

93. Ghosh, D., Ali, M. Y., Chaudhary, D. K. & Bhattacharyya, S. Dependence of halide composition on the stability of highly efficient all-inorganic cesium lead halide perovskite quantum dot solar cells. *Sol. Energy Mater. Sol. Cells* **185,** 28–35 (2018).

94. Li, Z. *et al.* Extrinsic ion migration in perovskite solar cells. *Energy Environ. Sci.* **10,** 1234–1242 (2017).

95. Chou, H.-H. *et al.* Zinc Porphyrin–Ethynylaniline Conjugates as Novel Hole-Transporting Materials for Perovskite Solar Cells with Power Conversion Efficiency of 16.6%. *ACS Energy Lett.* **1,** 956–962 (2016).

96. Yu, Q. *et al.* High-Efficiency Dye-Sensitized Solar Cells: The Influence of Lithium Ions on Exciton Dissociation, Charge Recombination, and Surface States. *ACS Nano* **4,** 6032–6038 (2010).

97. Joly, D. *et al.* A Robust Organic Dye for Dye Sensitized Solar Cells Based on Iodine/Iodide Electrolytes Combining High Efficiency and Outstanding Stability. *Sci. Rep.* **4,** 4033 (2014).

98. Nusbaumer, H., Zakeeruddin, S. M., Moser, J.-E. & Grätzel, M. An Alternative Efficient Redox Couple for the Dye-Sensitized Solar Cell System. *Chem. – A Eur. J.* **9,** 3756–3763 (2003).

99. Hagfeldt, A., Boschloo, G., Sun, L., Kloo, L. & Pettersson, H. Dye-Sensitized Solar Cells. *Chem. Rev.* **110,** 6595–6663 (2010).

100. Izatt, R. M., Pawlak, K., Bradshaw, J. S. & Bruening, R. L. Thermodynamic and kinetic data for macrocycle interactions with cations and anions. *Chem. Rev.* **91,** 1721–2085 (1991).

101. Hamann, T. W., Jensen, R. A., Martinson, A. B. F., Van Ryswyk, H. & Hupp, J. T. Advancing beyond current generation dye-sensitized solar cells. *Energy Environ. Sci.* **1,** 66–78 (2008).

102. Wang, Z.-S., Sayama, K. & Sugihara, H. Efficient Eosin Y Dye-Sensitized Solar Cell

Containing Br-/Br3- Electrolyte. *J. Phys. Chem. B* **109,** 22449–22455 (2005).

103. Duvva, N., Chilakamarthi, U. & Giribabu, L. Recent developments in tetrathiafulvalene and dithiafulvalene based metal-free organic sensitizers for dye-sensitized solar cells: a mini-review. *Sustain. Energy Fuels* **1,** 678–688 (2017).

104. Tian, H., Yu, Z., Hagfeldt, A., Kloo, L. & Sun, L. Organic Redox Couples and Organic Counter Electrode for Efficient Organic Dye-Sensitized Solar Cells. *J. Am. Chem. Soc.* **133,** 9413–9422 (2011).

105. Bai, Y. *et al.* High-efficiency organic dye-sensitized mesoscopic solar cells with a copper redox shuttle. *Chem. Commun.* **47,** 4376–4378 (2011).

106. Xu, B. *et al.* 1,1,2,2-Tetrachloroethane (TeCA) as a solvent additive for organic hole transport materials and its application in highly efficient solid-state dye-sensitized solar cells. *Adv. Energy Mater.* **5,** 1–6 (2015).

107. Lee, J. Y. *et al. Thiophene–nitroxide radical as a novel combination of sensitizer–redox mediator for dye-sensitized solar cells*. *Journal of Solid State Electrochemistry - J SOLID STATE ELECTROCHEM* **16,** (2012).

108. Wang, L., Wu, M., Gao, Y. & Ma, T. Highly catalytic counter electrodes for organic redox couple of thiolate/disulfide in dye-sensitized solar cells. *Appl. Phys. Lett.* **98,** 221102 (2011).

109. Tian, H. *et al.* A thiolate/disulfide ionic liquid electrolyte for organic dye-sensitized solar cells based on Pt-free counter electrodes. *Chem. Commun.* **47,** 10124–10126 (2011).

110. Liu, Y., Jennings, J. R., Parameswaran, M. & Wang, Q. An organic redox mediator for dye-sensitized solar cells with near unity quantum efficiency. *Energy Environ. Sci.* **4,** 564–571 (2011).

111. Cheng, M., Yang, X., Li, S., Wang, X. & Sun, L. Efficient dye-sensitized solar cells based on an iodine-free electrolyte using l-cysteine/l-cystine as a redox couple. *Energy Environ. Sci.* **5,** 6290–6293 (2012).

112. Pashaei, B., Shahroosvand, H. & Abbasi, P. Transition metal complex redox shuttles

for dye-sensitized solar cells. *RSC Adv.* **5,** 94814–94848 (2015).

113. Yella, A. *et al.* Porphyrin-Sensitized Solar Cells with Cobalt (II/III)–Based Redox Electrolyte Exceed 12 Percent Efficiency. *Science (80-.).* **334,** 629 LP-634 (2011).

114. Gao, J., Fischer, A., Svensson, P. H. & Kloo, L. Crystallography as Forensic Tool for Understanding Electrolyte Degradation in Dye–sensitized Solar Cells. *ChemistrySelect* **2,** 1675–1680 (2017).

115. Bella, F., Galliano, S., Gerbaldi, C. & Viscardi, G. Cobalt-based electrolytes for dye-sensitized solar cells: Recent advances towards stable devices. *Energies* **9,** 1–22 (2016).

116. Klahr, B. M. & Hamann, T. W. Performance Enhancement and Limitations of Cobalt Bipyridyl Redox Shuttles in Dye-Sensitized Solar Cells. *J. Phys. Chem. C* **113,** 14040–14045 (2009).

117. Mosconi, E. *et al.* Cobalt Electrolyte/Dye Interactions in Dye-Sensitized Solar Cells: A Combined Computational and Experimental Study. *J. Am. Chem. Soc.* **134,** 19438–19453 (2012).

118. Saygili, Y. *et al.* Copper Bipyridyl Redox Mediators for Dye-Sensitized Solar Cells with High Photovoltage. *J. Am. Chem. Soc.* **138,** 15087–15096 (2016).

119. Feldt, S. M. *et al.* Regeneration and recombination kinetics in cobalt polypyridine based dye-sensitized solar cells, explained using Marcus theory. *Phys. Chem. Chem. Phys.* **15,** 7087–7097 (2013).

120. Xie, Y. & Hamann, T. W. Fast low-spin cobalt complex redox shuttles for dye-sensitized solar cells. *J. Phys. Chem. Lett.* **4,** 328–332 (2013).

121. Kashif, M. K. *et al.* A new direction in dye-sensitized solar cells redox mediator development: In situ fine-tuning of the cobalt(II)/(III) redox potential through lewis base interactions. *J. Am. Chem. Soc.* **134,** 16646–16653 (2012).

122. Gregg, B. A. Interfacial processes in the dye-sensitized solar cell. *Coord. Chem. Rev.* **248,** 1215–1224 (2004).

123. Gregg, B. A., Pichot, F., Ferrere, S. & Fields, C. L. Interfacial Recombination Processes

in Dye-Sensitized Solar Cells and Methods To Passivate the Interfaces. *J. Phys. Chem. B* **105,** 1422–1429 (2001).

124. Zuo, C. & Ding, L. Solution-Processed Cu2O and CuO as Hole Transport Materials for Efficient Perovskite Solar Cells. *Small* **11,** 5528–5532 (2015).

125. Daeneke, T. *et al.* Aqueous Dye-Sensitized Solar Cell Electrolytes Based on the Ferricyanide–Ferrocyanide Redox Couple. *Adv. Mater.* **24,** 1222–1225 (2012).

126. Rorabacher, D. B. Electron Transfer by Copper Centers. *Chem. Rev.* **104,** 651–698 (2004).

127. Colombo, A. *et al.* Efficient copper mediators based on bulky asymmetric phenanthrolines for DSSCs. *ACS Appl. Mater. Interfaces* **6,** 13945–13955 (2014).

128. Hattori, S., Wada, Y., Yanagida, S. & Fukuzumi, S. Blue Copper Model Complexes with Distorted Tetragonal Geometry Acting as Effective Electron-Transfer Mediators in Dye-Sensitized Solar Cells. 9648–9654 (2005).

129. Freitag, M. *et al.* Copper phenanthroline as a fast and high-performance redox mediator for dye-sensitized solar cells. *J. Phys. Chem. C* **120,** 9595–9603 (2016).

130. Michaels, H. *et al.* Copper Complexes with Tetradentate Ligands for Enhanced Charge Transport in Dye-Sensitized Solar Cells. *Inorganics* **6,** (2018).

131. Li, M. H., Yum, J. H., Moon, S. J. & Chen, P. Inorganic p-type semiconductors: Their applications and progress in dye-sensitized solar cells and perovskite solar cells. *Energies* **9,** 1–28 (2016).

132. Perera, K. T. and G. R. R. A. K. and I. R. M. K. and K. G. U. W. and V. P. S. A solid-state photovoltaic cell sensitized with a ruthenium bipyridyl complex. *J. Phys. D. Appl. Phys.* **31,** 1492 (1998).

133. O'Regan, B., Lenzmann, F., Muis, R. & Wienke, J. A Solid-State Dye-Sensitized Solar Cell Fabricated with Pressure-Treated P25−TiO_2 and CuSCN: Analysis of Pore Filling and IV Characteristics. *Chem. Mater.* **14,** 5023–5029 (2002).

134. Tennakone, K. *et al.* Dye-sensitized solid-state photovoltaic cells: Suppression of electron-hole recombination by deposition of the dye on a thin insulating film in

contact with a semiconductor. *J. Electron. Mater.* **30,** 992–996 (2001).

135. Kumara, G. R. A., Kaneko, S., Okuya, M. & Tennakone, K. Fabrication of Dye-Sensitized Solar Cells Using Triethylamine Hydrothiocyanate as a CuI Crystal Growth Inhibitor. *Langmuir* **18,** 10493–10495 (2002).

136. Meng, Q.-B. *et al.* Fabrication of an Efficient Solid-State Dye-Sensitized Solar Cell. *Langmuir* **19,** 3572–3574 (2003).

137. Kumara, G. R. A., Konno, A., Shiratsuchi, K., Tsukahara, J. & Tennakone, K. Dye-Sensitized Solid-State Solar Cells: Use of Crystal Growth Inhibitors for Deposition of the Hole Collector. *Chem. Mater.* **14,** 954–955 (2002).

138. Sakamoto, H., Igarashi, S., Niume, K. & Nagai, M. Highly efficient all solid state dye-sensitized solar cells by the specific interaction of CuI with NCS groups. *Org. Electron.* **12,** 1247–1252 (2011).

139. SAKAMOTO, H., IGARASHI, S., NIUME, K. & NAGAI, M. All solid state dye-sensitized solar cells by the specific interaction of CuI with NCS groups for practical use. *J. Ceram. Soc. Japan* **120,** 304–306 (2012).

140. Sakamoto, H., Igarashi, S., Uchida, M., Niume, K. & Nagai, M. Highly efficient all solid state dye-sensitized solar cells by the specific interaction of CuI with NCS groups II. Enhancement of the photovoltaic characteristics. *Org. Electron.* **13,** 514–518 (2012).

141. Chung, I., Lee, B., He, J., Chang, R. P. H. & Kanatzidis, M. G. All-solid-state dye-sensitized solar cells with high efficiency. *Nature* **485,** 486 (2012).

142. Kwon, U. *et al.* Solution-Processible Crystalline NiO Nanoparticles for High-Performance Planar Perovskite Photovoltaic Cells. *Sci. Rep.* **6,** 30759 (2016).

143. Jung, M. *et al.* Thermal Stability of CuSCN Hole Conductor-Based Perovskite Solar Cells. *ChemSusChem* **9,** 2592–2596 (2016).

144. Chen, W.-Y. *et al.* Low-cost solution-processed copper iodide as an alternative to PEDOT:PSS hole transport layer for efficient and stable inverted planar heterojunction perovskite solar cells. *J. Mater. Chem. A* **3,** 19353–19359 (2015).

145. Qin, P. *et al.* Inorganic hole conductor-based lead halide perovskite solar cells with

12.4% conversion efficiency. *Nat. Commun.* **5,** 3834 (2014).

146. Hossain, M. I., Alharbi, F. H. & Tabet, N. Copper oxide as inorganic hole transport material for lead halide perovskite based solar cells. *Sol. Energy* **120,** 370–380 (2015).

147. Yang, G. *et al.* A facile molecularly engineered copper (II) phthalocyanine as hole transport material for planar perovskite solar cells with enhanced performance and stability. *Nano Energy* **31,** 322–330 (2017).

148. Qi, D. & Jiang, J. Toward Panchromatic Organic Functional Molecules: Density Functional Theory Study on the Electronic Absorption Spectra of Substituted Tetraanthracenylporphyrins. *J. Phys. Chem. A* **115,** 13811–13820 (2011).

149. Ke, W. *et al.* Efficient fully-vacuum-processed perovskite solar cells using copper phthalocyanine as hole selective layers. *J. Mater. Chem. A* **3,** 23888–23894 (2015).

150. Sfyri, G. *et al.* Soluble butyl substituted copper phthalocyanine as alternative hole-transporting material for solution processed perovskite solar cells. *Electrochim. Acta* **212,** 929–933 (2016).

151. Nouri, E. *et al.* Soluble tetratriphenylamine Zn phthalocyanine as Hole Transporting Material for Perovskite Solar Cells. *Electrochim. Acta* **222,** 875–880 (2016).

152. Wang, F. *et al.* Soluble hexamethyl-substituted subphthalocyanine as a dopant-free hole transport material for planar perovskite solar cells. *R. Soc. Open Sci.* **5,** (2018).

153. Liu, X. *et al.* Tetra-Propyl-Substituted Copper (II) Phthalocyanine as Dopant-Free Hole Transporting Material for Planar Perovskite Solar Cells. *Sol. RRL* **2,** 1800050 (2018).

154. Hua, Y., Liu, P., Li, Y., Sun, L. & Kloo, L. Composite Hole-Transport Materials Based on a Metal-Organic Copper Complex and Spiro-OMeTAD for Efficient Perovskite Solar Cells. *Sol. RRL* **1700073,** 1700073 (2018).

155. Vivo, P., Salunke, J. K. & Priimagi, A. Hole-transporting materials for printable perovskite solar cells. *Materials (Basel).* **10,** 1–45 (2017).

156. Zhang, Y. *et al.* Enhanced performance of perovskite solar cells with P3HT hole-

transporting materials via molecular p-type doping. *RSC Adv.* **6,** 108888–108895 (2016).

157. Zhang, W., Zhu, R., Li, F., Wang, Q. & Liu, B. High-Performance Solid-State Organic Dye Sensitized Solar Cells with P3HT as Hole Transporter. *J. Phys. Chem. C* **115,** 7038–7043 (2011).

158. Zhang, J. *et al.* Efficient solid-state dye sensitized solar cells: The influence of dye molecular structures for the in-situ photoelectrochemically polymerized PEDOT as hole transporting material. *Nano Energy* **19,** 455–470 (2016).

159. Sun, W. *et al.* An ammonia modified PEDOT: PSS for interfacial engineering in inverted planar perovskite solar cells. *Org. Electron.* **46,** 22–27 (2017).

160. Nei de Freitas, J., Nogueira, A. F. & De Paoli, M.-A. New insights into dye-sensitized solar cells with polymer electrolytes. *J. Mater. Chem.* **19,** 5279–5294 (2009).

161. Wang, L., Fang, S., Lin, Y., Zhou, X. & Li, M. A 7.72% efficient dye sensitized solar cell based on novel necklace-like polymer gel electrolyte containing latent chemically cross-linked gel electrolyte precursors. *Chem. Commun.* 5687–5689 (2005). doi:10.1039/B510335E

162. Chen, J.-G., Chen, C.-Y., Wu, C.-G. & Ho, K.-C. In Situ Low Temperature Polymerization of Bismaleimide for Gel-Type Electrolyte for Dye-Sensitized Solar Cells. *J. Phys. Chem. C* **114,** 13832–13837 (2010).

163. Rawolle, M. *et al.* Infiltration of Polymer Hole-Conductor into Mesoporous Titania Structures for Solid-State Dye-Sensitized Solar Cells. *ACS Appl. Mater. Interfaces* **5,** 719–729 (2013).

164. Nia, N. Y., Matteocci, F., Cina, L. & Di Carlo, A. High-Efficiency Perovskite Solar Cell Based on Poly(3-Hexylthiophene): Influence of Molecular Weight and Mesoscopic Scaffold Layer. *ChemSusChem* **10,** 3854–3860 (2017).

165. Hu, L. *et al.* Inverted Planar Perovskite Solar Cells with a High Fill Factor and Negligible Hysteresis by the Dual Effect of NaCl-Doped PEDOT:PSS. *ACS Appl. Mater. Interfaces* **9,** 43902–43909 (2017).

166. Hutchison, G. R., Ratner, M. A. & Marks, T. J. Hopping Transport in Conductive Heterocyclic Oligomers: Reorganization Energies and Substituent Effects. *J. Am. Chem. Soc.* **127,** 2339–2350 (2005).

167. Bach, U. *et al.* Charge Separation in Solid-State Dye-Sensitized Heterojunction Solar Cells. *J. Am. Chem. Soc.* **121,** 7445–7446 (1999).

168. Agarwala, P. & Kabra, D. A review on triphenylamine (TPA) based organic hole transport materials (HTMs) for dye sensitized solar cells (DSSCs) and perovskite solar cells (PSCs): Evolution and molecular engineering. *J. Mater. Chem. A* **5,** 1348–1373 (2017).

169. Hawash, Z., Ono, L. K. & Qi, Y. Recent Advances in Spiro-MeOTAD Hole Transport Material and Its Applications in Organic–Inorganic Halide Perovskite Solar Cells. *Adv. Mater. Interfaces* **5,** 1–22 (2018).

170. Burschka, J. *et al.* Tris(2-(1H-pyrazol-1-yl)pyridine)cobalt(III) as p-Type Dopant for Organic Semiconductors and Its Application in Highly Efficient Solid-State Dye-Sensitized Solar Cells. *J. Am. Chem. Soc.* **133,** 18042–18045 (2011).

171. Leijtens, T. *et al.* Hole Transport Materials with Low Glass Transition Temperatures and High Solubility for Application in Solid-State Dye-Sensitized Solar Cells. *ACS Nano* **6,** 1455–1462 (2012).

172. Yang, L. *et al.* Initial Light Soaking Treatment Enables Hole Transport Material to Outperform Spiro-OMeTAD in Solid-State Dye-Sensitized Solar Cells. *J. Am. Chem. Soc.* **135,** 7378–7385 (2013).

173. Burschka, J., Kessler, F., Nazeeruddin, M. K. & Grätzel, M. Co(III) Complexes as p-Dopants in Solid-State Dye-Sensitized Solar Cells. *Chem. Mater.* **25,** 2986–2990 (2013).

174. ONOZAWA-KOMATSUZAKI, N. *et al.* Novel Cobalt Complexes as a Dopant for Hole-transporting Material in Perovskite Solar Cells. *Electrochemistry* **85,** 226–230 (2017).

175. Chen, D.-Y. *et al.* Application of F4TCNQ doped spiro-MeOTAD in high performance solid state dye sensitized solar cells. *Phys. Chem. Chem. Phys.* **14,** 11689–11694

(2012).

176. Xu, M. *et al.* Improvement in Solid-State Dye Sensitized Solar Cells by p-Type Doping with Lewis Acid SnCl4. *J. Phys. Chem. C* **117,** 22492–22496 (2013).

177. Xu, B. *et al.* AgTFSI as p-Type Dopant for Efficient and Stable Solid-State Dye-Sensitized and Perovskite Solar Cells. *ChemSusChem* **7,** 3252–3256 (2014).

178. Juarez-Perez, E. J. *et al.* Role of the Dopants on the Morphological and Transport Properties of Spiro-MeOTAD Hole Transport Layer. *Chem. Mater.* **28,** 5702–5709 (2016).

179. Snaith, H. J. & Grätzel, M. Enhanced charge mobility in a molecular hole transporter via addition of redox inactive ionic dopant: Implication to dye-sensitized solar cells. *Appl. Phys. Lett.* **89,** 262114 (2006).

180. Bailie, C. D., Unger, E. L., Zakeeruddin, S. M., Grätzel, M. & McGehee, M. D. Melt-infiltration of spiro-OMeTAD and thermal instability of solid-state dye-sensitized solar cells. *Phys. Chem. Chem. Phys.* **16,** 4864–4870 (2014).

181. Liu, D. & Liu, Y. Recent progress of dopant-free organic hole-transporting materials in perovskite solar cells. *J. Semicond.* **38,** (2017).

182. Liu, J. *et al.* A dopant-free hole-transporting material for efficient and stable perovskite solar cells. *Energy Environ. Sci.* **7,** 2963–2967 (2014).

183. Freitag, M. *et al.* Dye-sensitized solar cells for efficient power generation under ambient lighting. *Nat. Photonics* **11,** 372–378 (2017).

184. Mathews, I., King, P. J., Stafford, F. & Frizzell, R. Performance of III–V Solar Cells as Indoor Light Energy Harvesters. *IEEE J. Photovoltaics* **6,** 230–235 (2016).

185. Yang, P. C., Chan, I. M., Lin, C. H. & Chang, Y. L. Thin film solar cells for indoor use. in *2011 37th IEEE Photovoltaic Specialists Conference* 696–698 (2011). doi:10.1109/PVSC.2011.6186049

186. Sahmer, A. Z., Mohamed, N. M. & Zaine, S. N. A. Effectiveness of dye sensitised solar cell under low light condition using wide band dye. *AIP Conf. Proc.* **1669,** 20068 (2015).

187. Marcus, R. A. Electrostatic Free Energy and Other Properties of States Having Nonequilibrium Polarization. I. *J. Chem. Phys.* **24,** 979–989 (1956).

188. Lundgren, J. R. & Stradiotto Mark. Key Concepts in Ligand Design: An Introduction. *Ligand Des. Met. Chem. React. Catal.* 1–14 (2016).

189. Yoder, J. C., Roth, J. P., Gussenhoven, E. M., Larsen, A. S. & Mayer, J. M. Electron and Hydrogen-Atom Self-Exchange Reactions of Iron and Cobalt Coordination Complexes. *J. Am. Chem. Soc.* **125,** 2629–2640 (2003).

190. Snaith, H. J. Estimating the Maximum Attainable Efficiency in Dye-Sensitized Solar Cells. *Adv. Funct. Mater.* **20,** 13–19 (2009).

191. Senevirathna, W., Daddario, C. M. & Sauv??, G. Density functional theory study predicts low reorganization energies for azadipyrromethene-based metal complexes. *J. Phys. Chem. Lett.* **5,** 935–941 (2014).

192. Kumar, C. V., Sfyri, G., Raptis, D., Stathatos, E. & Lianos, P. Perovskite solar cell with low cost Cu-phthalocyanine as hole transporting material. *RSC Adv.* **5,** 3786–3791 (2015).

193. Teak, C. K. *et al.* Molecularly Engineered Phthalocyanines as Hole-Transporting Materials in Perovskite Solar Cells Reaching Power Conversion Efficiency of 17.5%. *Adv. Energy Mater.* **7,** 1601733 (2016).

194. Wang, Y. *et al.* Tetra-alkyl-substituted copper (II) phthalocyanines as dopant-free hole-transport layers for planar perovskite solar cells with enhanced open circuit voltage and stability. *Dye. Pigment.* **139,** 619–626 (2017).

195. Hua, Y. *et al.* High conductivity Ag-based metal organic complexes as dopant-free hole-transport materials for perovskite solar cells with high fill factors. *Chem. Sci.* 2633–2638 (2016). doi:10.1039/C5SC03569D

196. Chou, H.-H. *et al.* Zinc Porphyrin–Ethynylaniline Conjugates as Novel Hole-Transporting Materials for Perovskite Solar Cells with Power Conversion Efficiency of 16.6%. *ACS Energy Lett.* **1,** 956–962 (2016).

197. Teh, C. H. *et al.* A review of organic small molecule-based hole-transporting materials

for meso-structured organic–inorganic perovskite solar cells. *J. Mater. Chem. A* **00,** 1–35 (2016).

198. Chen, C. *et al.* Cu(II) Complexes as p-Type Dopants in Efficient Perovskite Solar Cells. *ACS Energy Lett.* **2,** 497–503 (2017).

199. Gu, X. *et al.* FeCl3 as a low-cost and efficient p-type dopant of Spiro-OMeTAD for high performance perovskite solar cells. *RSC Adv.* **8,** 9409–9413 (2018).

200. Saygılı, Y. *et al. Planar Perovskite Solar Cells with High Open-Circuit Voltage Containing a Supramolecular Iron Complex as Hole Transport Material Dopant*. *ChemPhysChem* **19,** (2018).

201. Ye, J. *et al.* Bipyridine type Co-complexes as hole-transporting material dopants in perovskite solar cells. *RSC Adv.* **6,** 17354–17359 (2016).

202. Teh, C. H. *et al.* High-efficiency dye-sensitized solar cells with molecular copper phenanthroline as solid hole conductor. *Energy Environ. Sci.* **1,** 651–698 (2015).

203. Shanthi, S., Subramanian, C. & Ramasamy, P. Preparation and properties of sprayed undoped and fluorine doped tin oxide films. *Mater. Sci. Eng. B* **57,** 127–134 (1999).

204. www.dyenamo.se. Available at: https://www.dyenamo.se/.

205. Jiang, N. *et al.* High temperature stability of dye solar cells. *Sol. Energy Mater. Sol. Cells* **119,** 36–50 (2013).

206. Saygili, Y. *et al.* Copper Bipyridyl Redox Mediators for Dye-Sensitized Solar Cells with High Photovoltage. (2016). doi:10.1021/jacs.6b10721

207. Arora, N. *et al.* Intrinsic and Extrinsic Stability of Formamidinium Lead Bromide Perovskite Solar Cells Yielding High Photovoltage. *Nano Lett.* **16,** 7155–7162 (2016).

208. Karani, A. *et al.* Perovskite/Colloidal Quantum Dot Tandem Solar Cells: Theoretical Modeling and Monolithic Structure. *ACS Energy Lett.* **3,** 869–874 (2018).

209. Thomas, S. *et al.* A review on counter electrode materials in dye-sensitized solar cells. *J. Mater. Chem. A* **2,** 4474–4490 (2014).

210. Fu, D., Zhang, X. L., Barber, R. L. & Bach, U. Dye-Sensitized Back-Contact Solar Cells.

Adv. Mater. **22,** 4270–4274 (2010).

211. Ellis, H. *et al.* PEDOT counter electrodes for dye-sensitized solar cells prepared by aqueous micellar electrodeposition. *Electrochim. Acta* **107,** 45–51 (2013).

212. Papageorgiou, N. Counter-electrode function in nanocrystalline photoelectrochemical cell configurations. *Coord. Chem. Rev.* **248,** 1421–1446 (2004).

213. Sacco, A. Electrochemical impedance spectroscopy : Fundamentals and application in dye-sensitized solar cells. *Renew. Sustain. Energy Rev.* **79,** 814–829 (2017).

214. Ellis, H. *et al.* Electrochimica Acta PEDOT counter electrodes for dye-sensitized solar cells prepared by aqueous micellar electrodeposition. *Electrochim. Acta* **107,** 45–51 (2013).

215. Bisquert, J. & Fabregat-Santiago, F. *Impedance Spectroscopy: A General Introduction and Application to Dye-Sensitized Solar Cells*. *Dye-Sensitized Solar Cells* (2010).

216. Pascoe, A. R., Duffy, N. W., Scully, A. D., Huang, F. & Cheng, Y.-B. Insights into Planar CH3NH3PbI3 Perovskite Solar Cells Using Impedance Spectroscopy. *J. Phys. Chem. C* **119,** 4444–4453 (2015).

217. Kashif, M. K. *et al.* Cobalt Polypyridyl Complexes as Transparent Solution-Processable Solid-State Charge Transport Materials. 1–13

218. Weaver, M. J. & Yee, E. L. Activation Parameters for Homogeneous Outer-Sphere Electron-Transfer Reactions. Comparisons Between Self-Exchange and Cross Reactions Using Marcus' Theory. *Inorg. Chem.* **19,** 1936–1945 (1980).

219. Liu, Y. *et al.* Cobalt Redox Mediators for Ruthenium-Based Dye-Sensitized Solar Cells: A Combined Impedance Spectroscopy and Near-IR Transmittance Study. *J. Phys. Chem. C* **115,** 18847–18855 (2011).

220. Brunschwig, B. S., Creutz, C., MacArtney, D. H., Sham, T. K. & Sutin, N. The role of inner-sphere configuration changes in electron-exchange reactions of metal complexes. *Faraday Discuss. Chem. Soc.* **74,** 113–127 (1982).

221. Yum, J.-H. *et al.* A cobalt complex redox shuttle for dye-sensitized solar cells with high open-circuit potentials. *Nat. Commun.* **3,** 631 (2012).

222. Bustarret, E. *et al.* Superconductivity in doped cubic silicon. *Nature* **444,** 465 (2006).

223. Bubnova, O. *et al.* Semi-metallic polymers. *Nat. Mater.* **13,** 190 (2013).

224. Hogg, R. & Wilkins, R. G. 57. Exchange studies of certain chelate compounds of the transitional metals. Part VIII. 2,2′,2″-terpyridine complexes. *J. Chem. Soc.* 341–350 (1962). doi:10.1039/JR9620000341

225. Krivokapic, I. *et al.* Spin-crossover in cobalt(II) imine complexes. *Coord. Chem. Rev.* **251,** 364–378 (2007).

226. Kashif, M. K. *et al.* Cobalt Polypyridyl Complexes as Transparent Solution-Processable Solid-State Charge Transport Materials. *Adv. Energy Mater.* **201600874,** 1–7 (2016).

227. Tang, C. W. Two-layer organic photovoltaic cell. *Appl. Phys. Lett.* **48,** 183–185 (1986).

228. Xu, H. *et al.* Recent progress in metal–organic complexes for optoelectronic applications. *Chem. Soc. Rev.* **43,** 3259–3302 (2014).

229. Ren, X. *et al.* Organometallic Complexes as Hole-Transporting Materials in Organic Light-Emitting Diodes. *Inorg. Chem.* **43,** 1697–1707 (2004).

230. Neale, N. R., Kopidakis, N., van de Lagemaat, J., Grätzel, M. & Frank, A. J. Effect of a Coadsorbent on the Performance of Dye-Sensitized TiO_2 Solar Cells: Shielding versus Band-Edge Movement. *J. Phys. Chem. B* **109,** 23183–23189 (2005).

231. Kashif, M. K. *et al.* Polypyridyl Iron Complex as a Hole- Transporting Material for Formamidinium Lead Bromide Perovskite Solar Cells. 1855–1859 (2017). doi:10.1021/acsenergylett.7b00522

232. Saliba, M. *et al.* A molecularly engineered hole-transporting material for efficient perovskite solar cells. *Nat. Energy* **1,** 15017 (2016).

233. Abate, A. *et al.* Lithium salts as “redox active” p-type dopants for organic semiconductors and their impact in solid-state dye-sensitized solar cells. *Phys. Chem. Chem. Phys.* **15,** 2572–2579 (2013).

234. Juarez-Perez, E. J. *et al.* Role of the Dopants on the Morphological and Transport Properties of Spiro-MeOTAD Hole Transport Layer. *Chem. Mater.* **28,** 5702–5709 (2016).

235. Wang, S. *et al.* Role of 4-tert-Butylpyridine as a Hole Transport Layer Morphological Controller in Perovskite Solar Cells. *Nano Lett.* **16,** 5594–5600 (2016).

236. Cappel, U. B., Daeneke, T. & Bach, U. Oxygen-Induced Doping of Spiro-MeOTAD in Solid-State Dye-Sensitized Solar Cells and Its Impact on Device Performance. *Nano Lett.* **12,** 4925–4931 (2012).

237. Schölin, R. *et al.* Energy Level Shifts in Spiro-OMeTAD Molecular Thin Films When Adding Li-TFSI. *J. Phys. Chem. C* **116,** 26300–26305 (2012).

238. Nguyen, W. H., Bailie, C. D., Unger, E. L. & McGehee, M. D. Enhancing the Hole-Conductivity of Spiro-OMeTAD without Oxygen or Lithium Salts by Using Spiro(TFSI)2 in Perovskite and Dye-Sensitized Solar Cells. *J. Am. Chem. Soc.* **136,** 10996–11001 (2014).

239. Kazim, S. *et al.* A dopant free linear acene derivative as a hole transport material for perovskite pigmented solar cells. *Energy Environ. Sci.* **8,** 1816–1823 (2015).

240. Parthasarathy, G., Shen, C., Kahn, A. & Forrest, S. R. Lithium doping of semiconducting organic charge transport materials. *J. Appl. Phys.* **89,** 4986–4992 (2001).

241. Tro, N. J. & Neu, D. Chemistry in Focus: A Molecular View of Our World. **29,** 643 (2008).

242. Chan, M.-S. & Wahl, A. C. Rate of electron exchange between iron, ruthenium, and osmium complexes containing 1,10-phenanthroline, 2,2'-bipyridyl, or their derivatives from nuclear magnetic resonance studies. *J. Phys. Chem.* **82,** 2542–2549 (1978).

243. Lawson Daku, L. M. & Hauser, A. Ab Initio Molecular Dynamics Study of an Aqueous Solution of [Fe(bpy)3](Cl)2 in the Low-Spin and in the High-Spin States. *J. Phys. Chem. Lett.* **1,** 1830–1835 (2010).

244. Cardona, C. M., Li, W., Kaifer, A. E., Stockdale, D. & Bazan, G. C. Electrochemical Considerations for Determining Absolute Frontier Orbital Energy Levels of Conjugated Polymers for Solar Cell Applications. *Adv. Mater.* **23,** 2367–2371 (2011).

245. Dao, Q.-D., Fujii, A., Tsuji, R., Takeoka, Y. & Ozaki, M. Efficiency enhancement in

perovskite solar cell utilizing solution-processable phthalocyanine hole transport layer with thermal annealing. *Org. Electron.* **43,** 156–161 (2017).

246. Kakiage, K. *et al.* Highly-efficient dye-sensitized solar cells with collaborative sensitization by silyl-anchor and carboxy-anchor dyes. *Chem. Commun.* **51,** 15894–15897 (2015).

247. Rorabacher, D. B. & Rorabacher, D. B. Electron Transfer by Copper Centers Electron Transfer by Copper Centers. **104,** 651–698 (2004).

248. De Rienzo, F., Gabdoulline, R. R., Menziani, M. C. & Wade, R. C. Blue copper proteins: a comparative analysis of their molecular interaction properties. *Protein Sci.* **9,** 1439–1454 (2000).

249. Freitag, M. *et al.* High-efficiency dye-sensitized solar cells with molecular copper phenanthroline as solid hole conductor. *Energy Environ. Sci.* **8,** 2634–2637 (2015).

250. Zhang, W. *et al.* Comprehensive control of voltage loss enables 11.7% efficient solid-state dye-sensitized solar cells. *Energy Environ. Sci.* **11,** 1779–1787 (2018).

251. Robertazzi, A. *et al.* Copper−1,10-Phenanthroline Complexes Binding to DNA: Structural Predictions from Molecular Simulations. *J. Phys. Chem. B* **113,** 10881–10890 (2009).

252. Olsson, M. H. M. & Ryde, U. Geometry, Reduction Potential, and Reorganization Energy of the Binuclear CuA Site, Studied by Density Functional Theory. *J. Am. Chem. Soc.* **123,** 7866–7876 (2001).

253. Gennari, M., Pécaut, J., Collomb, M.-N. & Duboc, C. A copper thiolate centre for electron transfer: mononuclear vs. dinuclear complexes. *Dalt. Trans.* **41,** 3130–3133 (2012).

254. Rusanova, J. A., Kozachuk, O. V, Semenaka, V. V & Dyakonenko, V. V. Bis(2,9-dimethyl-1,10-phenanthroline)copper(I) penta-cyanido-nitro-soferrate(II). *Acta Crystallogr. Sect. E Struct. Reports Online* **69,** m684–m685 (2013).

255. Cong, J. *et al.* Bis(1,1-bis(2-pyridyl)ethane)copper(i / ii) as an efficient redox couple for liquid dye-sensitized solar cells. *J. Mater. Chem. A* **4,** 14550–14554 (2016).

256. Kavan, L. *et al.* Electrochimica Acta Electrochemical Properties of Cu (II / I) -Based Redox Mediators for Dye-Sensitized Solar Cells. **227,** 194–202 (2017).

257. Freitag, M. *et al.* Copper Phenanthroline as a Fast and High-Performance Redox Mediator for Dye-Sensitized Solar Cells. (2016). doi:10.1021/acs.jpcc.6b01658

258. Wu, J. *et al.* Counter electrodes in dye-sensitized solar cells. *Chem. Soc. Rev.* **46,** 5975–6023 (2017).

259. Garcı, R., Jiang, R. & Canto-aguilar, E. J. Improving the mass transport of copper-complex redox mediators in dye-sensitized solar cells by reducing the inter-electrode distance †. 32132–32142 (2017). doi:10.1039/C7CP06088B

260. Yella, A. *et al.* Dye-sensitized solar cells using cobalt electrolytes: the influence of porosity and pore size to achieve high-efficiency. *J. Mater. Chem. C* **5,** 2833–2843 (2017).

261. XIONG, B.-T. *et al.* Adsorption of 4-tert-Butylpyridine on TiO_2 Surface in Dye-Sensitized Solar Cells. *Chinese J. Chem.* **26,** 70–76 (2008).

262. Ferdowsi, P. *et al.* Alternative bases to 4-tert-butylpyridine for dye-sensitized solar cells employing copper redox mediator. *Electrochim. Acta* **265,** 194–201 (2018).

263. Dürr, M., Yasuda, A. & Nelles, G. On the origin of increased open circuit voltage of dye-sensitized solar cells using 4-tert-butyl pyridine as additive to the electrolyte. *Appl. Phys. Lett.* **89,** 61110 (2006).

264. Ondersma, J. W. & Hamann, T. W. Recombination and redox couples in dye-sensitized solar cells. *Coord. Chem. Rev.* **257,** 1533–1543 (2013).

265. Stergiopoulos, T., Rozi, E., Karagianni, C.-S. & Falaras, P. Influence of electrolyte co-additives on the performance of dye-sensitized solar cells. *Nanoscale Res. Lett.* **6,** 307 (2011).

266. Coronado, E., Galán-Mascarós, J. R., Gómez-García, C. J. & Laukhin, V. Coexistence of ferromagnetism and metallic conductivity in a molecule-based layered compound. *Nature* **408,** 447 (2000).